

M.Sc. Thesis - R. Wu; McMaster University – Mechanical Engineering

**ANISOTROPIC WETTING SURFACES MACHINED BY
DIAMOND TOOL WITH TIPS MICROSTRUCTURED BY
FOCUSED ION BEAM**

M.Sc. Thesis - R. Wu; McMaster University – Mechanical Engineering

**ANISOTROPIC WETTING SURFACES MACHINED BY
DIAMOND TOOL WITH TIPS MICROSTRUCTURED BY
FOCUSED ION BEAM**

By RONG WU

B.Eng. (Harbin Institute of Technology, Harbin, P.R. China)

A Thesis Submitted to the School of Graduate Studies in Partial Fulfilment of the
Requirements for the Degree Master of Applied Science

McMaster University © Copyright by Rong Wu, August 2019

McMaster University MASTER OF APPLIED SCIENCE (2019)

Hamilton, Ontario, Canada Mechanical Engineering

TITLE: ANISOTROPIC WETTING SURFACES MACHINED
BY DIAMOND TOOL WITH TIPS
MICROSTRUCTURED BY FOCUSED ION BEAM

AUTHOR: RONG WU, B.Eng.

Supervisor Dr. P. R. Selvaganapathy
Dr. Mohammed Tauhiduzzaman

NUMBER OF PAGES xx, 135

ABSTRACT

In recent years, there has been an increasing interest in the study of hydrophobic surfaces. Hydrophobic surfaces have been used in multiple applications in microfluidic devices due to their properties of self-cleaning, and also in deicing products. Conventionally, hydrophobic surfaces were created by laser cutting, self-assembly and other chemical processing methods. However, in most of these methods, hydrophobicity of the surface cannot be maintained for an extended time or restricted to limited set of materials. A low-cost, high-throughput method to generate highly hydrophobic anisotropic surface has been developed in this thesis which uses Computer Numerical Control (CNC) machining employing diamond tools whose tips have been micro-structured using Focused Ion Beam (FIB) built tips. The versatility of this method has been demonstrated by machining both metal and polymeric materials. Significant anisotropic wetting has been observed on the machined surface with the anisotropic contact angle can reach up to 71.6° and highly-hydrophobic property with contact angle of 163.1° on 6061 Aluminum Alloy and 155.7° on PMMA surface.

ACKNOWLEDGEMENT

First, I am very grateful to my supervisor Professor Ponnambalam Ravi Selvaganapathy, for his trust and unconditional support during these 2 years. He inspired and encouraged me with his abundant knowledge and expertise to help me come up with research ideas. He generously spent his time to discussion and offered advices which were great helpful. His open-minded thoughts and professional guidance are important part of the main forces to help me complete the entire research project.

Second, I would like to thank Dr. Mohammed Tauhiduzzaman for supporting this research and sparing time to discuss and allow me to access the facility of National Research Council London. He truly supported me in the mechanical machining aspects of the reserch with his engineering insights. My appreciation also goes to all the committee members: Dr. Matiar Howlader, Dr. P. Ravi Selvaganapathy, Dr. Tohid Didar and Dr. Tauhiduzzaman Mohammed for spending their valuable time.

I must also acknowledge Dr. Zhilin Peng, research engineer in department of engineering physics in McMaster. He provided great helps to let me use the instrument in their facility. He trained me with patient and offered inspired ideas.

I thank my fellow labmates in Center for Advanced Micro-Electro-Fluidics laboratory: Dr. Jain Nidhi, Alireza Shahin-Shamsabadi, Devon Jones, Fathalla Mohamed, Nan Xiao, Shadi Shahriari, Sreekant Damodara, Vinay patel, Aliakbar, Mohammadhossein, Dariush, Aydin, Yujie Zhu. A very special thanks goes to Nan Xiao, who inspired me to get new ideas. They are very nice friends who supported me and gave me advices with both research and life. Their help and great sense of humour provided me many precious memories which became fortune in my life.

Last but not least, I would like to deeply thank my husband, the love of my life, Xintong Guo. His support and love are the power to drive me to go forward. His accompany made my life beautiful and memorable. My sincere appreciation also goes to my parents who encourage and support me to pursue my dream. This thesis is dedicated to my husband and my parents, for their unconditional love for me.

TABLE OF CONTENTS

ABSTRACT	iii
ACKNOWLEDGEMENT	iv
TABLE OF CONTENTS	v
LIST OF FIGURES	ix
LIST OF TABLES	xix
LIST OF ALL ABBREVIATIONS	xx
Chapter 1: Motivation and Organization	1
1.1 Motivation.....	1
1.2 Organization.....	4
1.3 Contribution	6
Chapter 2: Introduction	7
2.1Hydrophobic Surface	7
2.1.1 Fundamental theory of isotropic wetting	7

2.1.2 Contact angle measurement	15
2.2 Hydrophobic surface fabrication.....	18
2.2.1 Chemical fabrication of hydrophobic surface.....	19
2.2.2 Physical methods for fabrication of hydrophobic surface	28
2.3 Anisotropic wetting.....	40
2.4 Anisotropic wetting surface fabrication.....	42
2.4.1 Photolithography based chemical modification.....	43
2.4.2 Embossing.....	45
2.4.3 Nanoimprinting lithography.....	46
2.4.3 Surface wrinkled pattern	48
2.5 Focused Ion Beam.....	49
2.5.1 Fundamental theory of Focused Ion Beam	49
2.5.2 FIB for engraving topographical features on diamond tool.....	53
2.6 Summary	55
Chapter 3: Experimental Set-Up and Methods.....	57
3.2 SCD tool microstructuring by FIB.....	58
3.2.1 Preparation of SCD tools	60
3.2.2 Focused ion beam machining.....	61

3.3 CNC machining	66
3.4 Surface characterization	68
3.4.1 In-situ SEM analysis	69
3.4.2 Confocal microscope structure characterization	70
3.4.3 Surface roughness measurement	71
3.5 Contact angle measurement	73
Chapter 4: Results and discussion	78
4.1 FIB milling of tool tip	78
4.2 One-directional CNC machining results	86
4.3 Effect of CNC machining parameters on anisotropic wetting	97
4.3.1 Effect of different cutting depths on anisotropic wetting	98
4.3.2 Effect of different cutting speeds on anisotropic wetting	103
4.3.3 Effect of materials on the anisotropic wetting	106
4.3.3 Effect of spacing on the anisotropic wetting	108
4.4 Two-directional CNC machining results	110
4.5 Summary	115
Chapter 5: Conclusion and future work	116
5.1 Conclusion	116

5.2 Future work.....	118
5.2.1 FIB milling accuracy improvement	118
5.2.2 Hierarchical structures machining	119
5.2.3 Applications	120
Appendix A: 3D scanning images under Sensofar confocal microscope in NRC (London).....	122
Appendix B: Time-cost table of experimental process	124
LIST OF REFERENCES.....	125

LIST OF FIGURES

Figure 2. 1 Graphic vector representation of parameters in a sessile drop based on Young’s theory	8
Figure 2. 2 Four categories of wettability: (a) superhydrophilic, (b) hydrophilic, (c) hydrophobic, (d) super hydrophobic.	9
Figure 2. 3 Schematic of the Wenzel (a) and Cassie-Baxter (b) states on rough surfaces	12
Figure 2. 4 Schematic view of advancing and receding contact angles.....	13
Figure 2. 5 (a) SEM images of lotus leaf surface at various magnifications, which shows the hierarchical structure of the surface. (b) Image of a water droplet sitting on a lotus leaf[4].	15
Figure 2. 6 Same droplet stood on a superhydrophobic surface measured under different fitting principles(a) ellipse fitting; (b) circle fitting; (c) tangent searching; (d) and Laplace–Young fitting. [22]	16
Figure 2. 7 Schematic of θ_{Ad} and θ_{Re} using needle embedded sessile drop method. (a) θ_{Ad} : the maximum angle reliably when liquid added to the surface. (b) θ_{Re} : the minimum angle reliably when liquid withdrawing from surface. [24]	18

Figure 2. 8 Schematic of the CVD mechanism: (1) Vaporisation of reactants. (2) transfer to substrate. (3) loss of gaseous molecules from reaction exhaust. (4) physisorption of reactant. (5) chemisorption of atoms in ideal surface environment and form a film. [17]20

Figure 2. 9 SEM of micro structures on a superhydrophobic PTFE surface treated by PECVD [24].21

Figure 2. 10 SEM images of the surfaces of the samples from ion assisted chemical etching treatments for 1 min under two magnification (1000× and 20,000×). (a) and (b) with Cr³⁺, (c) and (d) with Cu²⁺, (e) and (f) with Ag⁺[37].....23

Figure 2. 11 Schematic view of the LBM process29

Figure 2. 12 (a) SEM image of micro-pillar arrays on stainless steel surface (b) Water drop on the laser fabricated stainless steel surface[6].....30

Figure 2. 13 SEM images of Laser beam machined surface: top images of (a) 100 μm spacing size, (c) 300 μm spacing size, (e) 500 μm spacing size and enlarged tilting image of (b) 100 μm spacing size, (d) 300 μm spacing size, (f) 500 μm spacing size [61].31

Figure 2. 14 Schematic of superhydrophilic and superhydrophobic surfaces with laser beam machining and post process[61].32

Figure 2. 15 Images of droplet contact angle: initial stages(a),(b),(c); after annealing without ethanol (d),(e),(f); and after annealing with ethanol (g),(h),(i); with 100, 300, and 500 μm spacing size respectively.33

Figure 2. 16 Images of LBM results with different spacing size (a)10 μm (b)15 μm (c)20 μm (d)25 μm (e)30 μm (f) 35 μm . SEM images of PDMS casted surface with 25 μm spacing size under (g)-(i)[63]34

Figure 2. 17 Water droplet contact angles results for different grid spacing sizes[63].35

Figure 2. 18 Performance of laser machined sapphire surface: (a) surperhydrophobicity (b) water repellence and transparency (c) self-cleaning effect [65]......36

Figure 2. 19 Schematic view of micro-mushrooms fabrication process: (a) A wire cuts channels by vertical motion into a steel block and undercuts by lateral displacement in (b). Then the sample is rotated by 90° (c) and the procedure repeated until completion (d)[67]......38

Figure 2. 20 (a) The figure of one micro-mushroom structure sample (b) the droplet states on this machined surface (c) a RL-68H oil sitting on this surface[67].39

Figure 2. 21 Picture sequences of an impacting water droplet[7].....40

Figure 2. 22 (a) Schematic representation of a droplet upon the anisotropic wetting surface.
(b) contact angle profile of θ_Y ($\theta \perp$), which is observed from Y direction. (c) contact angle profile of θ_X ($\theta \parallel$) which is observed from X direction.....42

Figure 2. 23 The dynamic wetting of surfaces with line width $5\mu\text{m}$: (a) dynamic state in orthogonal direction (b) dynamic state in parallel direction [68].....44

Figure 2. 24 Droplet state on (a) original Aluminum surface (b) aluminum surface after micro-embossing[10].....46

Figure 2. 25 SEM micrographs for different hierarchical structures: (A) $2\mu\text{m} \perp 250\text{nm}$; (B) $2\mu\text{m} \angle 250\text{nm}$; (C) $2\mu\text{m} // 250\text{nm}$; (D) $2\mu\text{m} \perp 2\mu\text{m}$; and (E) $2\mu\text{m} \angle 2\mu\text{m}$. [70]48

Figure 2. 26 Schematic diagram of various processes during ion interaction [77].....51

Figure 2. 27 Schematic column of main components[78]52

Figure 2. 28 Schematic of two beam positions52

Figure 2. 29 Nanoscale SCD tool fabricated by FIB machining. (a) Original SCD tool; (b) a lower magnification view of the same tool after fabrication; (c) lateral view of the

nanoscale SCD tool; (d) top view of the nanoscale SCD tool; (e) a view of the diamond tip under higher magnification [79].....	54
Figure 3. 1 Schematic of the experimental process	58
Figure 3. 2 Picture of Versa 3D FIB system [1]	59
Figure 3. 3 Design drawings and dimension unit (mm) (a) 3D design of SCD diamond tool and tool holder. (b) top view of tool and dimension of details (c) details of tool tip design from top view (d) cross-section view of tool tip (e) side view of tool and dimensions (f) details of tool tip from side view.....	63
Figure 3. 4 Schematic of position relationship during FIB milling. FIB had an 84-degree intersection angle with an SCD tool surface after tool rotating 58 degrees.	65
Figure 3. 5 Schematic of multi-step FIB milling procedures.....	66
Figure 3. 6 MICROGANTRY system and main components at National Research Council (NRC), London, ON.....	68
Figure 3. 7 SEM images of the original SCD tool (a) Top view of the rake face, (b) Perspective view after tool tilting to 58°.	70
Figure 3. 8 SENSOFAR® METROLOGY S Neox 3D Optical Profiler located at National Research Council (NRC), London, ON [4]	71

Figure 3. 9 Alicona Infinite Focus G5	73
Figure 3. 10 OCA 35 contact angle measurement instrument and its main components. .	74
Figure 3. 11 Schematic of pick-up droplet process.....	76
Figure 3. 12 Device used to measure the sliding angle.....	77
Figure 4. 1 Schematic of FIB milling process from SEM view based on Figure4.1. (a) Schematic of milling steps from SEM view. (i) is the first step (ii) is the second step (iii) is the third step. (b) Schematic of FIB milling steps from top view of the tool. Red box represents the zoomed representation of the area where the FIB milling occurs. (i) is the first step with $3\mu\text{m} \times 3\mu\text{m}$ area (ii) is the second step with $5\mu\text{m} \times 3\mu\text{m}$ area (iii) is the third step with $5\mu\text{m} \times 3\mu\text{m}$ area.(c) Dimensions of four SCD tools..	80
Figure 4. 2 (a)SEM images of diamond tool milling by FIB with multi-step (b) SEM perspective schematic view of the machined feature(c) Schematic side view of SCD tool. The microgrooves went through the whole tool tip and had an intersection angle of 6 degree.	81
Figure 4. 3 FIB images of four machined diamond tools (a) tool #1 with $1\mu\text{m} \times 1\mu\text{m}$ grooves and $30\mu\text{m}$ spacing, (b) tool #2 with $2\mu\text{m} \times 2\mu\text{m}$ grooves and $30\mu\text{m}$ spacing, (c) tool #3	

with $5\mu\text{m}\times 8\mu\text{m}$ grooves and $50\mu\text{m}$ spacing, (d) tool #4 with $5\mu\text{m}\times 5\mu\text{m}$ grooves and $20\mu\text{m}$ spacing.82

Figure 4. 4 Result of single step machining by FIB84

Figure 4. 5 FIB milling defects with ripples and round corners.85

Figure 4. 6 SEM images of Aluminum machined by tool #2 at 300 mm/min cutting speed.
(a) $200\times$ magnification of Aluminum sample (b) $500\times$ magnification of Aluminum sample.....88

Figure 4. 7 PMMA samples machined by tool #4 at 1000 mm/min cutting speed. (a) $600\times$ magnification (b) $2000\times$ magnification (c) $4000\times$ magnification88

Figure 4. 8 The partial height scanning results under confocal microscope of PMMA sample cut by tool #2 at 300 mm/min89

Figure 4. 9 Dimensional variation between cross-section area of micro-ridges on PMMA samples and micro-grooves on tooltips, including the actual size of tool #2 to #4 in x-axis.....90

Figure 4. 10 Sessile droplets on PMMA sample and 6061 Al sample. (a) PMMA surface parallel contact angle of 108.9° in along-feature direction (b) PMMA surface vertical contact angle of 155.7° from across-feature direction (c) 6061 Al sample parallel

contact angle of 108.1° from along-feature direction. (d) 6061 Al sample vertical contact angle of 163.1° from across-feature direction.....92

Figure 4. 11 Printed text observed through PMMA surface after CNC machining by tool#2 as an illustration of its transparency and clarity. The surface was machined with tool#2 which had 2µm×2µm structures with three different cutting speeds: 300mm/min, 1000mm/min and 2000mm/min.93

Figure 4. 12 Droplet distortion with 6 cm diameter based on hexagonal array[88]97

Figure 4. 13 Height of the micro-ridges obtained with tool #3 machining with various depth of cut and at at speed of 300mm/min on PMMA workpiece (n=3).....98

Figure 4. 14 Contact angle results with different three cutting depth: 2 µm, 4 µm, 8 µm on PMMA samples. Along label indicates the contact angle along the ridges while across label represents direction perpendicular to the ridges. Five measurements were taken of each sample in each direction. 100

Figure 4. 15 Anisotropic contact angle ($\Delta\theta$) results of samples based on three cutting depth:2 µm, 4 µm, 8 µm. 100

Figure 4. 16 Contact angle versus spacing [89] 102

Figure 4. 17 Contact angle with three different cutting speeds on PMMA samples. Along label represents the contact angle in direction along the ridges and across represents the contact angles in the direction perpendicular to the ridges.104

Figure 4. 18 Contact angle with different cutting depth on Aluminum samples. Along angles are the contact angle in along features direction and across contact angles are in across features direction.105

Figure 4. 19 Anisotropic contact angle ($\Delta\theta$) results of samples with different cutting speeds. (a) $\Delta\theta$ of PMMA samples with three different cutting speeds: 300mm/min, 1000mm/min, 2000mm/min (b) $\Delta\theta$ of 6061 Aluminum samples with two cutting speeds: 300mm/min, 2000mm/min.106

Figure 4. 20 Contact angle measurement results of 6061 Aluminum alloy and PMMA sample at same machining parameters at 300mm/min cutting speed with 8 μ m cutting depth. Along angles are the contact angle in along features direction and across contact angles are in across features direction.107

Figure 4. 21 Contact angle with different spacing between ridges built on the surface which is 50 μ m and 20 μ m of microstructure spacing of SCD cutting tool on Aluminum samples. Along angles are the contact angle in along features direction and across contact angles are in across features direction.109

Figure 4. 22 Schematic of two-step directional machining process 111

Figure 4. 23 SEM images of micro-pillar structures with different rotation angles. (a) 90° rotation angle under 300× magnification (b) 90° rotation angle under 2000× magnification (c) 45° rotation angle under 300× magnification (d) 45° rotation angle under 3000× magnification (e) 60° rotation angle under 800× magnification (f) 60° rotation angle under 3000× magnification. 113

Figure 4. 24 (a) Sessile water droplet on two-directional machining surface with 45 degree intersection angle (b) Schematic of droplet stated on the two-directional machining surface with 45 degree intersection angle 114

Figure 5. 1 Schematic of three feasible milling conceptions from top view. (a) First beginning with nano-structure fabrication and then applying micro-structures on the tool. (b) First beginning with micro-structures and then nano-structures (c) Triangle design with microstructure fabrication first and nanostructure after. 120

LIST OF TABLES

Table 2. 1 Chemical fabrication of hydrophobic surface.....	25
Table 4. 1 Machining parameters details of different conditions	89
Table 4. 2 Contact angle of two-directional machined samples	113

LIST OF ALL ABBREVIATIONS

CAH	Contact angle hysteresis
CNC	Computer numerical control
CVD	Chemical vapor deposition
DI water	Deionized water
EDM	Electrical discharge machining
FIB	Focused ion beam
LBM	Laser beam machining
PMMA	Poly (methyl methacrylate)
SAM	Self-assembled monolayers
SCD	Single crystal diamond
SEM	Scanning electron microscope
TEM	Transmission electron microscopy

Chapter 1: Motivation and Organization

1.1 Motivation

Ever since the observation of the lotus effect where the water droplet slides off the lotus leaf, there has been significant interest in fabrication of superhydrophobic surfaces and to understand the phenomenon underlying that effect. Superhydrophobic surfaces have a wide variety of applications such as water-resistant spray, deicing surface on solar panels, defogging surface, self-cleaning surface in satellite dishes etc., many methods have been developed to fabricate superhydrophobic surfaces. The methods used to create superhydrophobic surfaces can be mainly classified into two approaches, namely: chemical and physical modification of surfaces. The chemical method aims to fabricate superhydrophobic surface by depositing small chemical molecules on the surface to change its surface energy lower to prevent wetting. These methods include techniques such as chemical vapor deposition (CVD) [1], chemical (stearic acid) spray coating on aluminum [2] and so on. However, most of chemical modifications can be removed or damaged due

to mechanical abrasion in the environment and can degrade quickly. Moreover, they are in many instances toxic to human health, degrade the environment and also involve time-consuming processes for deposition. Therefore, chemical fabrication methods may not be appropriate for outdoor operations, such as roofs, walls, and cars [3]. Physical methods modify the topography of the surface in order to directly change the contact area between liquid and solid surface, which lead to increase of contact angle. A classic example is the lotus leaf [4] where hierarchical structures at micro and nanoscale contribute to the formation of superhydrophobic surface properties and their stability [5]. Micro and nanoscale surface texturing have been introduced by soft lithography [4], laser beam machining (LBM) [6], electrical discharge machining (EDM) [7] and other methods. Soft lithography is a rapid way to replicate micro or nanostructures on to silicone surfaces, but it requires a mold that has been fabricated using other approaches such as photolithography which is expensive. In LBM, a laser is used to ablate material from both metallic and non-metallic materials to form periodic or aperiodic topographical features in the micro and the nanoscale. However, LBM has prolonged processing time especially for large scale area, and a post treatment like low temperature annealing always needed to convert the machined surface to hydrophobic or super hydrophobic surface. Recently, EDM has been used to machine conductive materials and generate microstructures to change the wettability of surface over a wide area to overcome some of the limitations of the LBM method [7].

Although promising, this method is restricted to conductive substrates and produces isotropic wetting properties.

In some applications, anisotropy in wetting characteristics is desired. For instance, in fabrication of surfaces for extraction of water from the atmospheric humidity in the form of dew, anisotropy in wetting could be used to direct the flow of the collected droplets in a certain direction towards the collection container. Other applications from microfluidic channels to biomedical devices can also benefit from the ability to create anisotropic wetting characteristics on surfaces where the contact angle and the wetting properties are directionally dependent. However, creating such anisotropic properties requires high degree of control over the physical structures that are formed on the substrates to cause changes in wetting property. Some research has been recently directed in this area where both chemical and physical methods have been used to create anisotropic wetting. Chemical methods are used to generate the surface with chemically heterogeneous pattern. For example, self-assembled monolayers (SAM) have been used to create chemically striped patterns [8]. Similarly, selective chemical etching [9] can also be used to create patterned surfaces on certain predefined regions using masking of other regions. However, as described earlier, these chemical methods are not long-lasting and can be easily removed as they modify only an ultra-thin layer close to the surface. Furthermore, SAM are often toxic and require enclosed environment for their coating. Physical methods that introduce topographical are mainly used to modify the surface structures, such as embossing [10] and

laser beam cutting [9]. Embossing methods also needs a master mold [10] but still suit for large scale fabrication due to its low-cost.

In this thesis, a new scale-up, low-cost, repeatable and rapid method to fabricate customizable anisotropic wetting surfaces has been developed. It uses established computer numerical controlled (CNC) machining to produce micro and nanoscale physical features on substrates by structuring the diamond cutting tools using a focused ion beam (FIB). The process consists of two part: fabrication of the tool and machining of the surface. This process can be used with both metallic or non-metallic materials over large and small areas. The thesis also develops processes for structuring non-conducting diamond tools using FIB and investigates the effect of various machining process parameters on the structures produced on the substrates and the ensuing contact angles obtained.

1.2 Organization

This thesis is organized as follows:

Chapter 2 provides a background literature for this thesis including the fundamentals of focused ion beam machining, the phenomenon of wetting and its various classifications. It then discusses the various methods that have been described in the literature to create hydrophobic surfaces, discusses the working principles and classifies them into physical

and chemical methods. Finally, it describes the latest research into FIB machining of non-conductive single crystal diamond.

Chapter 3 describes the materials and the experimental set up used in this thesis for FIB machining, CNC machining, surface characterization and contact angle measurement. The designs, experimental and fabrication method of diamond tools are included in this chapter.

Chapter 4 focuses on the results obtained in the experiments where two approaches to FIB machining of the diamond tool was performed. It discusses the effect of charge accumulation and its impact on the fidelity of the features formed. Next, it describes the results obtained with the textured SCD tool was used to machine various materials including PMMA, aluminum and bronze. Finally, the effect of the surface texturing introduced by the machining on the contact angle of the machined surface is characterized and discussed.

Chapter 5 concludes the thesis with a brief discussion on the contribution made in this thesis and a summary of the main results. The advantages of surfaces machined by FIB fabricated diamond tools are highlighted. Their limitations are pointed out together with aspects to be improved and developed in the future.

1.3 Contribution

Many of the current fabrication methods to create superhydrophobic surfaces are either expensive, do not last a long time or restricted to the types of materials that it can be used on. The main contribution of this thesis is to develop a new method of using microstructured CNC machining tool tip to form anisotropic highly hydrophobic surfaces that can be applied to a wide range of materials and can be performed using existing equipment in a fast manner. The thesis also develops protocols for the microstructuring of the SCD tool which is electrically non-conductive using an ion beam milling process. The surfaces created by milling show periodic microstructures that demonstrate contact angles approaching super hydrophobicity. These methods are expected to produce more robust and easily implementable superhydrophobic surfaces for industrial applications.

Chapter 2: Introduction

2.1 Hydrophobic Surface

Hydrophobicity is the propensity of a surface to prevent wetting of its surface when it comes in contact with water. Wetting property can be understood at the molecular level as the interaction between atoms of the solid surface with the molecules and ions in the liquid. Based on this understanding, various kinds of hydrophobic surfaces have been developed using a variety of fabrication methods. These include surface that are isotropic hydrophobic properties as well as anisotropic ones. The fabrication technologies can be classified into physical and chemical ones.

2.1.1 Fundamental theory of isotropic wetting

The interactions between a liquid droplet and a solid surface, such as in wetting of a surface, is of practical significance in many industrial applications and daily life. Systematic studies on wettability can be traced back to two centuries ago by Young [11] in 1804.

2.1.1.1 Young's theory

Young recognized that the contact angle made by a sessile droplet on a solid surface is the result of a mechanical equilibrium among three interfacial surface tensions at the contact line between the three different phases (liquid, solid and air). This is referred to as the Young's theory and this angle was named as Young's angle or static contact angle (θ) as shown in Figure 2.1.

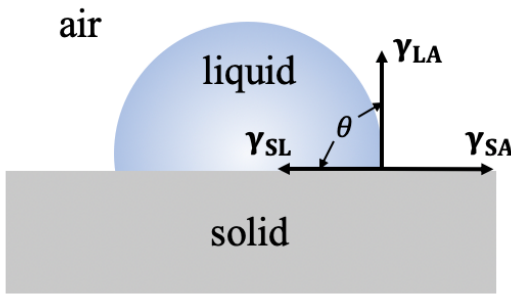


Figure 2. 1 Graphic vector representation of parameters in a sessile drop based on Young's theory

Young's angle can be calculated from three surface tensions (Eq.2.1), the solid surface tension (γ_{SA}), the liquid surface tension (γ_{LA}), the liquid-solid interfacial tension (γ_{SL}).

$$\gamma_{SA} = \gamma_{LA} \cdot \cos\theta + \gamma_{SL} \quad \text{Eq.2.1}$$

Based on the contact angle and the wetting behavior, the solid surfaces are classified into four categories which are shown in Figure 2.2: (a) superhydrophilic, if the contact angle is

less than 10° , (2) hydrophilic, if the contact angle is between 10° and 90° , (3) hydrophobic, if the contact angle is between 90° and 150° , and (4) superhydrophobic, if the contact angle is above 150° [12].

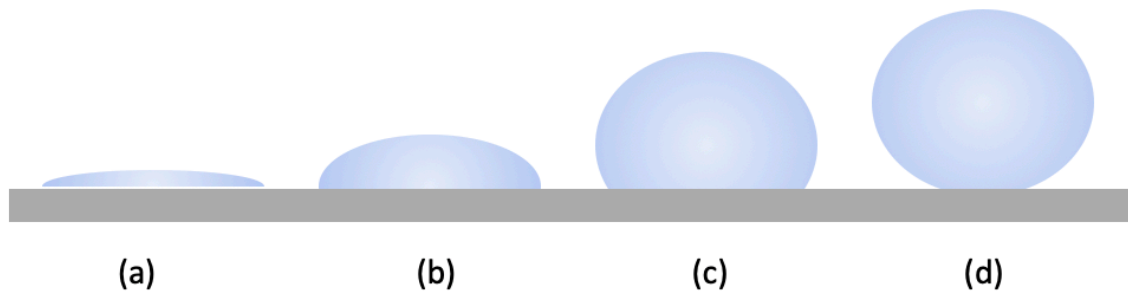


Figure 2. 2 Four categories of wettability: (a) superhydrophilic, (b) hydrophilic, (c) hydrophobic, (d) super hydrophobic.

Young 's theory is based on the assumption that the solid surface is smooth and flat. Later, this theory was modified to accommodate wetting on topographically non-flat surfaces by two other models, namely: Wenzel and Cassie-Baxter.

2.1.1.2 Wenzel and Cassie-Baxter models

The theory to describe wetting on a rough surface was first developed by Wenzel in 1936 [13]. This theory assumed that the liquid droplet fully wetted the solid rough surface which

is shown in Figure 2.3(a), and its wettability will be enhanced. The apparent contact angle on a fully wetted rough surface was then determined by the Wenzel equation Eq.2.2.

$$\cos\theta_w = r \cdot \cos\theta \quad \text{Eq.2.2}$$

where θ_w is the Wenzel contact angle, θ is the smooth surface's contact angle of the same material, and r is the roughness factor which is the ratio of real surface area to projected surface area (Eq.2.3).

$$r = \frac{\text{real surface area}}{\text{projected surface area}} = \frac{n(a_1+b_1+2h)L}{n(a_1+b_1)L} = \frac{a_1+b_1+2h}{a_1+b_1} \quad \text{Eq.2.3}$$

where, n is the number of microstructures in Figure 2.3(a), a_1 and b_1 is the widths of roughness, L is the length of roughness structures and h is the height of roughness.

Subsequently, Cassie and Baxter extended the theory [14] in 1944. They considered the case when the surface properties of the material are such that the droplet does not fully wet the entire surface of the solid. Instead wetting occurs only on the tips of the extended features of a rough surface while air bubbles are trapped in the nooks as shown in Fig 2.3(b). In this scenario, the surface energy equilibrium which is related to the contact area under the liquid droplet determines the contact angle of surfaces. In this case, the contact angle was found to be related to the area fraction of the solid in contact with the liquid as compared to that with air and is given by Cassi-Baxter equation shown in Eq.2.4 [14].

$$\cos\theta_{CB} = f_1 \cdot \cos\theta_1 + f_2 \cdot \cos\theta_2 \quad \text{Eq.2.4}$$

Where f_1 and f_2 , are the contact area fraction of the solid and air, θ_1 and θ_2 are the equilibrium contact angles, respectively.

Since the contact angle of droplet with air is 180° , and $f_1 + f_2 = 1$. The Eq.2.4 can also be written as

$$\cos\theta_{CB} = f \cdot \cos\theta + (f - 1) \quad \text{Eq.2.5}$$

$$f = \frac{\text{solid surface area}}{\text{projected surface area}} = \frac{n \cdot a_2 \cdot L}{n(a_2 + b_2)L} = \frac{a_2}{a_2 + b_2} \quad \text{Eq.2.6}$$

where θ_{CB} is the Cassie-Baxter angle, $\theta = \theta_1$ is the smooth surface's contact angle of the same material, $f = f_1$ is the solid area fraction which is the ratio of solid area to projected surface area, a_2 and b_2 are the width of solid area and air area, n is the number of solid area, L is the length of rough structures(Eq.2.6).

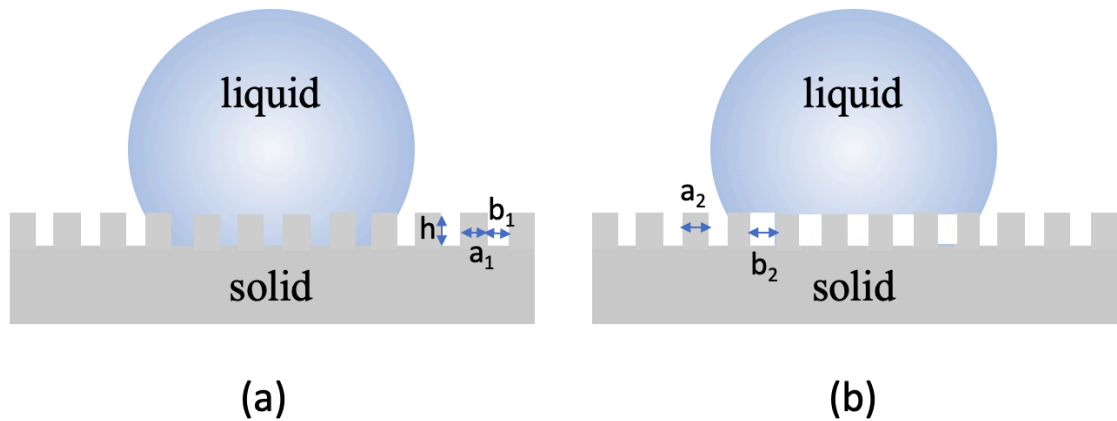


Figure 2. 3 Schematic of the Wenzel (a) and Cassie-Baxter (b) states on rough surfaces

2.1.1.3 Contact angle hysteresis

All the previous theories are based on static state of sessile droplet. However the dynamic state is also an important parameter of wettability and can be characterized by the sliding angle (α) and the phenomenon called contact angle hysteresis (CAH). These two values are used to measure stickiness of solid surface. When a solid stage is tilted at a certain speed after a sessile drop is formed on the surface, the tilt angle at which the drop will start to move is sliding angle as shown in Figure 2.4. The difference between the advancing contact angle (θ_{Ad}) and receding contact angle (θ_{Re}) is defined as CAH, which is shown in Figure 2.4. Low CAH means the water droplet has a low sliding angle and good water repellence property. The CAH of superhydrophobic surfaces with self-cleaning property should lower than 10° [4].

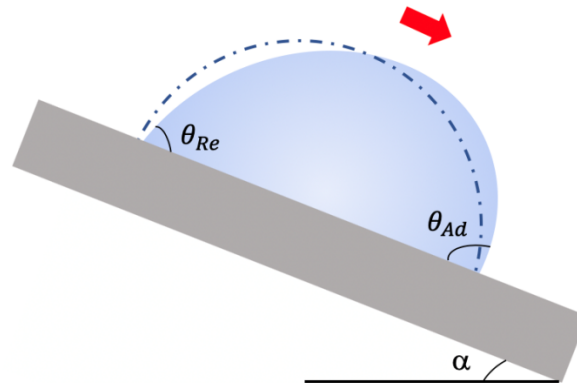


Figure 2. 4 Schematic view of advancing and receding contact angles.

2.1.1.4 Lotus effect

Lotus leaf has an interesting property that water droplets deposited on it rolls off easily. This rolling of water, takes along with it, dust and dirt that may have deposited leading to its fabled self-cleaning property. A resting water droplet on the lotus leaf is almost spherical in shape and this observation has resulted in numerous studies to explain and replicate this superhydrophobic property. Superhydrophobic phenomenon was initially studied by Dettre and Johnson in 1964 [15] with idealized heterogeneous hydrophobic surfaces. They observed that surface roughness was important to achieve high water repellence. After that, Barthlott et. al [16] in 1977 provided an explanation for the lotus effect. Two reasons were attributed for the superhydrophobicity, namely: a waxy hydrophobic material and numerous

microscopic bumps containing hierarchical structures that provide higher effective contact angle. Later, Cheng et.al found the contact angle of carnauba wax which had the same Fourier transform infrared spectroscopy signatures with lotus leaf wax was $74.0 \pm 8.5^\circ$ which makes it hydrophilic [17]. This discovery means that the hierarchical structures may have the primary role in the manifestation of superhydrophobic property of the lotus leaf. As shown in Figure 2.5, the hierarchical structures of lotus leaf were observed under SEM at three different magnifications. Numerous bumps containing hierarchical structures in the micro and the nanoscale enable the lotus leaf's surface to achieve superhydrophobic property of a contact angle greater than 150° . These structures are uneven so that air can trap into the space of bumps on the surface lead to a much greater contact angle as 160° [3].

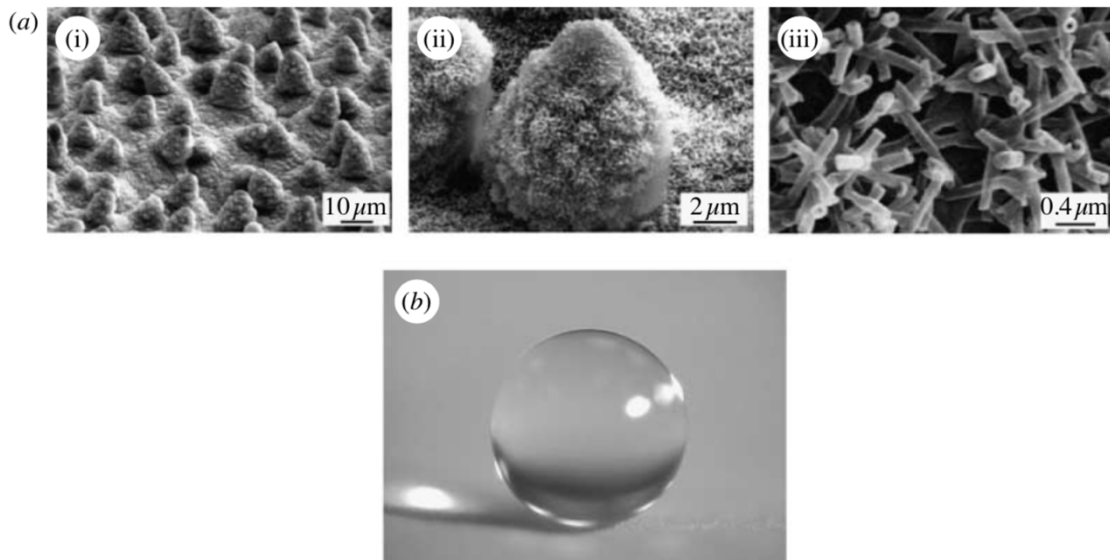


Figure 2. 5 (a) SEM images of lotus leaf surface at various magnifications, which shows the hierarchical structure of the surface. (b) Image of a water droplet sitting on a lotus leaf[4].

2.1.2 Contact angle measurement

2.1.2.1 Static sessile droplet contact angle measurement

Due to simplicity of the technique, contact angle measurement is very popular tool to characterize surface wettability. One of the most widely used technique for measuring contact angles is the optical-based sessile drop method by goniometer. A typical goniometer consists of a horizontal stage with a solid sample mount, located between a light source and a CCD camera. It comes with a motorized liquid dosing system as well, in order to dispense a certain amount of drop on the sample to form a sessile droplet. The control of parameters such as temperature, humidity, dust, in the environment is crucial to obtaining reliable measurements. A droplet volume from 1 μL to 2000 μL can be used for the measurement and there is no significant difference in the results [18]. Smaller volume of droplets is more sensitive to optical error but more suitable of super hydrophobic surfaces' measurement. Current instruments for contact angle measurement use camera and software to take the picture of droplet from the side to analyze the shape and compute contact angle. Four different mathematical methods are usually used to generate and calculate contact angle, including tangential method, circle method [19], ellipse method [20],

and Young-Laplace method [21]. The same droplet resting on a superhydrophobic surface measured using the various fitting method can produce different results as shown in Figure 2.6 [22].

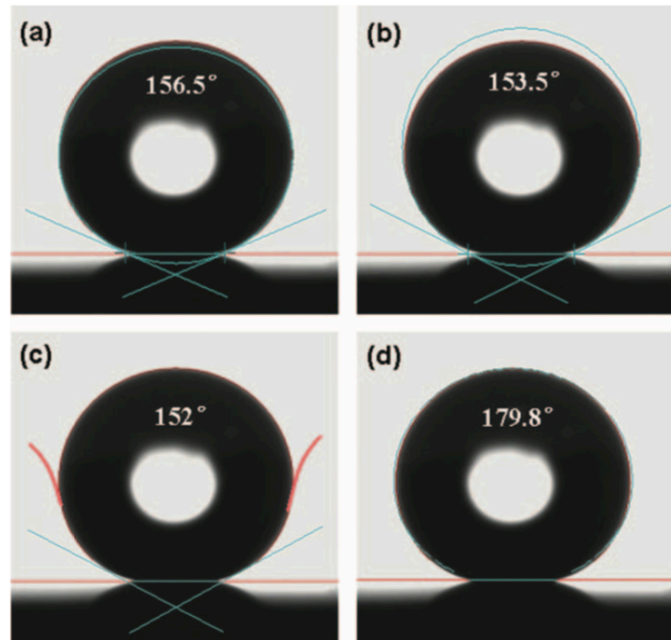


Figure 2. 6 Same droplet stood on a superhydrophobic surface measured under different fitting principles(a) ellipse fitting; (b) circle fitting; (c) tangent searching; (d) and Laplace–Young fitting. [22]

In the tangential method, the droplet outline and the baseline are captured from the image and then a tangent at the solid and liquid contact point drawn to determine the contact angle. Due to its reliance on software-based curve fitting, it may have a large error due to drop shape distortion caused by dust or surface irregularity. Circle method fits the droplet outline to a circle and assumes no distortion due to gravity. It is more suitable for small volume

droplet or super hydrophilic surface with very small contact angle. Ellipse method follows a similar approach but also accounts for the effect of gravity by fitting the droplet shape to an ellipse. This method is not suitable for extreme contact angles, such as below 30° , as the shape of the droplet deviates significantly from that of an ellipse [23]. Young-Laplace method assumes that gravity is the only external force, and the drop shape is axisymmetric under the surface tension and gravity forces. It is highly repeatable and reliable when the droplets are highly axisymmetric in their static state.

2.1.2.2 Sliding angle and CAH

CAH can be measurement by tilting plate method which is the simplest method for its measurement. By slowly tilting the surface and capturing images of the droplet as it slide, the advancing and receding contact angles can be obtained to determine the CAH. For the surface with low CAH the droplet easily rolls off the surface. There is another method to measure the CAH which called needle embedded sessile drop method shown in Figure 2.7 [24], [25] where θ_{Ad} is the maximum angle can be measured reliably when droplet is added to the surface at a very slow rate and θ_{Re} is the minimum angle of withdrawing droplet.

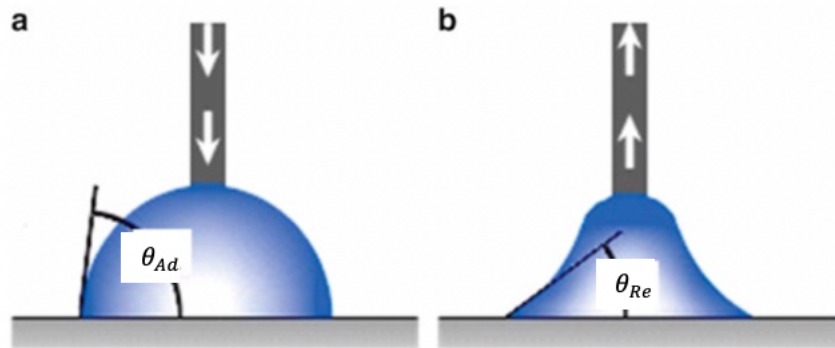


Figure 2. 7 Schematic of θ_{Ad} and θ_{Re} using needle embedded sessile drop method. (a) θ_{Ad} : the maximum angle reliably when liquid added to the surface. (b) θ_{Re} : the minimum angle reliably when liquid withdrawing from surface. [24]

Sliding angle(α) measurement reflects the propensity of the droplet to adhere to the surface which is used to understand the dynamic wetting property in this thesis. As shown in Figure 2.4, the sliding angle is the critical angle when the sessile droplet starts to slide down a surface when it is tilted at a slow speed (around 1°/second). The movement of droplet is mainly governed by a gravitational force and the friction of the surface that keeps the drop against sliding.

2.2 Hydrophobic surface fabrication

Due to the versatile use of hydrophobic surfaces in many different fields such as anti-icing surfaces, anti-fogging surfaces, there has been significant interest in the technologies to

fabricate hydrophobic surface recent years. Hydrophobic surfaces have generally been formed by either fabricating a unique surface structure or changing surface energy, to maintain a low energy of interaction with water. Two broad categories, physical and chemical methods used to form isotropic hydrophobic surfaces which have been extensively [3], [26], [27]. This section provides a short summary and fabrication methods associated with the various methods to form hydrophobic surfaces with particular emphasis on introducing anisotropic wetting properties.

2.2.1 Chemical fabrication of hydrophobic surface

Chemical fabrication of hydrophobic surface aims to influence the wettability of surface by lowering the surface energy. Low surface energy materials like fluoroalkylsilane and other fluorocarbons are widely used in chemical modification method. Several methods are reviewed in this section, more comprehensive information including material, substrate, contact angle and sliding angle of chemical fabrication methods is provided in Table 1.

2.2.1.1 Chemical vapor deposition

Chemical vapor deposition (CVD) is a method to deposit thin films and uniform layers of materials on a substrate. It is often used to modify surfaces and can be used to change its wetting properties. The general mechanism is illustrated in Figure 2.8 [1]. The reactants

are brought to the surface in the gaseous phase. The precursors are vaporized first if they are not already in the gas phase by thermal heating [28] or reduction of pressure [29]. Then, the reactants are activated to initiate chemical reaction by heating [30], or plasma activation [31] on the substrate. After physisorption followed by reaction, the products which are in the solid-state deposit on the substrate. Depending on the rate of deposition, smooth films as well as rough particles deposits can be formed [32]. Several materials have been used with the CVD method to form hydrophobic or superhydrophobic surface.

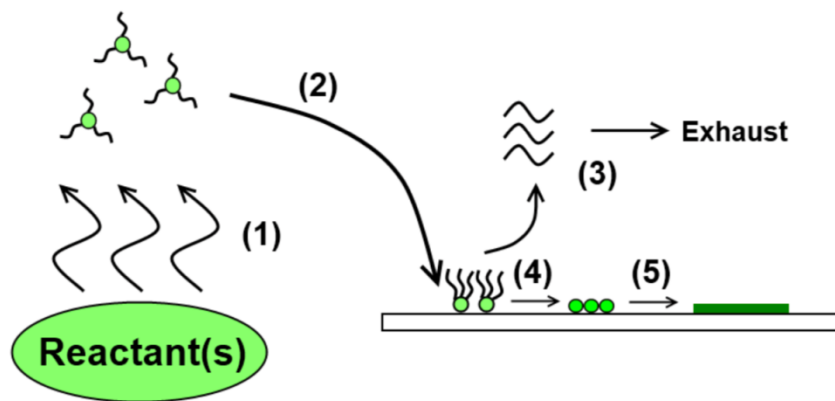


Figure 2. 8 Schematic of the CVD mechanism: (1) Vaporisation of reactants. (2) transfer to substrate. (3) loss of gaseous molecules from reaction exhaust. (4) physisorption of reactant. (5) chemisorption of atoms in ideal surface environment and form a film. [17]

Polytetrafluoroethylene (PTFE) surface coating using CVD method has been used to produce hydrophobic surfaces. PTFE is chemical inert and has low surface energy, providing a low wetting surface with contact angle of 118° . The polymer molecules do not

interact with water due to restricted access to the polarised C-F bonds [33]. PTFE is solid state at room temperature and can be deformed and reshaped easily by heating.. Pure PTFE deposit can only achieve moderate hydrophobicity, so plasma enhanced CVD (PECVD) has been used to increase the hydrophobicity to approach superhydrophobic level. The energy of plasma can activate or breakdown fluorocarbon molecules. During the PECVD process, rough particles can be generated by using the energy of plasma pulse through hexafluoroethane (C_6F_6) with H_2 feeding [34] which can further improve on hydrophobicity of surface. The SEM result of the micro-structure on the PECVD treated surface shows in Figure 2.9 and the contact angle of surfaces after treatment can reach as high as 160° [35].

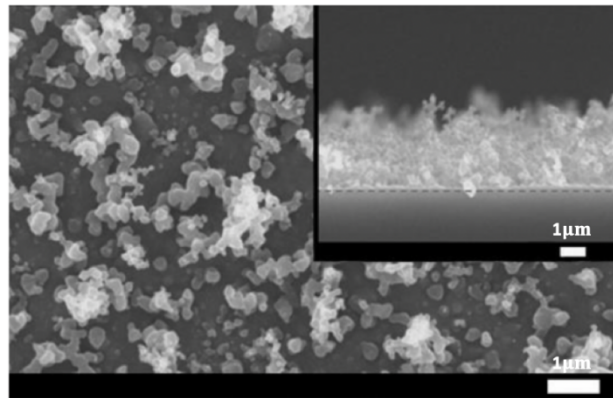


Figure 2. 9 SEM of micro structures on a superhydrophobic PTFE surface treated by PECVD [24].

The chemical treatment mentioned above can achieve superhydrophobic state rapidly and effectively. Although it provides good performance, the chemical deposited film loses its hydrophobicity over a short duration of time as chemical coatings can be removed or

damaged due to mechanical abrasion in the environment and degrade which makes it not a long-lasting method.

CVD synthesized aligned carbon nanotubes (CNTs) on Fe-N-coated Si substrates can also achieve hydrophobicity [36]. A contact angle of 146° was achieved using this approach and was subsequently increased to 159° after a thin film of ZnO deposition. Several other CVD fabricated hydrophobic surfaces are summarized in Table 2.1.

2.2.1.2 Solution based chemical treatment

Solution based chemical treatment methods are the lowest cost method to modify surfaces. For example, Qi et al. [37] developed the method called metal-assisted chemical etching to fabricate the hydrophobic surface on zinc plate. After cleaning ultrasonically, substrates were etched by a mixture of aqueous solution of HNO_3 and metal nitrate ($\text{Cu}(\text{NO}_3)_2$, AgNO_3 and $\text{Cr}(\text{NO}_3)_3$) at 30°C . After etching, samples were immersed in ethanol and fluoroalkylsilane (FAS) for surface modification. The surface etched in HNO_3 assisted by $\text{Cu}(\text{NO}_3)_2$, AgNO_3 with 1 minute etching time had contact angle $157 \pm 2^\circ$ and $162 \pm 2^\circ$, respectively. The surface of samples under SEM are shown in Figure 2.10 [37].

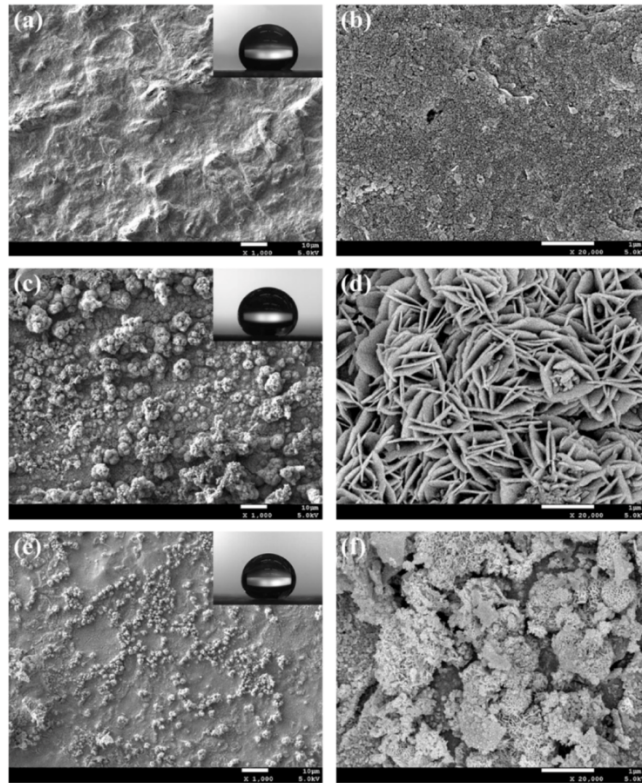


Figure 2. 10 SEM images of the surfaces of the samples from ion assisted chemical etching treatments for 1 min under two magnification (1000 \times and 20,000 \times). (a) and (b) with Cr^{3+} , (c) and (d) with Cu^{2+} , (e) and (f) with Ag^{+} [37].

Chemical etching on Cu substrate with solution of HNO_3 and AgNO_3 and then immersed in FAS (perfluorodecyltriethoxysilane) solution has been done by Chu et al.[38]. the contact angle obtained on treated copper surface was $157 \pm 1^\circ$. The solution of HCl and $\text{Cu}(\text{NO}_3)_2$ etched Al surface was tried by the same group with $164 \pm 1^\circ$ of contact angle. A

comprehensive list of materials and substrates modified by solution based chemical treatment methods are included in Table 2.1 below.

2.2.1.3 Other chemical methods

For some low surface energy materials, spin coating process can be used to deposit them and generate hydrophobic surface. Guo et al.[39] applied vinyl terminated poly(dimethylsiloxane) and perfluorononane on Aluminum sample at a speed of 3000 rpm for 30 s. The contact angle of coated surface was $168 \pm 2^\circ$.

Electrochemical method is widely used to generate rough structures and form hydrophobic surfaces. Zhang et.al [40] used electrochemical deposition of gold onto an indium tin oxide (ITO) electrode. They combined it with layer-by-layer technique to form monolayer of n-dodecanethiol as a post treatment to achieve superhydrophobicity. The treated surface could reach the contact angle as high as 156° .

Various other processing methods have also been used to attach low surface energy materials on to surfaces such as Plasma [41]⁻⁴³, solution immersion [44-46], self-assembled monolayers [45], sand-blasting and acid etching (SLA) [46], slippery liquid-infused porous surface (SLIPS) [47] and are listed in Table 1 below.

Table 2. 1 Chemical fabrication of hydrophobic surface

Method	Substrate	Material	Contact angle(°)	Sliding angle(°)
Chemical Vapor Deposition[35]	Silicon	Polytetrafluoroethylene (PTFE), Hexafluoroethane, Hydrogen, Acetone	160	/
Chemical Vapor Deposition[48]	Silicon	Aluminum etchant type D, Octadecyltrichlorosilane(OTS), Acetone, Isopropanol	155	1
Chemical Vapor Deposition[49]	Silicon	Fluoroalkyl silane ($CF_3(CF_2)_nCH_2CH_2Si(OCH_3)_3$; $n=0, 5, \text{ or } 7$), Ozone, Oxygen	112	/
Plasma-enhanced chemical vapor deposition[50]	Poly(ethylene terephthalate) (PET)	Organosilane, Fluoroalkylsilane (FAS), tetramethylsilane(TMS), $Si(CH_3)_3$	≥ 150	/
Plasma-enhanced chemical vapor deposition[51]	Copy-grade paper/handsheets	Pentafluoroethane, Argon carrier gas, PFE monomer gas, Oxygen, N_2	166.7	3.4
Chemical etching[37]	Zinc	fluoroalkylsilane (FAS), HNO_3 , Metal nitrate ($Cu(NO_3)_2$, $AgNO_3$ and $Cr(NO_3)_3$, Ethanol	$Cu(NO_3)_2$:1 57 ± 2 $AgNO_3$:162 ± 2 $Cr(NO_3)_3$:1 43 ± 2	/

Chemical etching[38]	Aluminum/Copper	Fine sand paper, Ethyl alcohol, $\text{Cu}(\text{NO}_3)_2 \cdot 3\text{H}_2\text{O}$, HCl, AgNO_3 , HNO_3 , Perfluorodecyltriethoxysilane	Al: 164 ± 1 , Copper: 157 ± 1	/
Chemical etching[52]	Aluminum foil	$\text{CuCl}_2 \cdot 2\text{H}_2\text{O}$, Emery paper no. 400, no. 600, and no. 1000, Hydrochloric acid, Hexadecyl- trimethoxysilane	161.9 ± 0.5	6.8
Chemical etching+spin coating[39]	Aluminum/Aluminum alloy 2024Al	sodium hydroxide (NaOH), perfluorononane (C_9F_{20}), poly(dimethylsiloxane) vinyl terminated (PDMSVT) containing 1 wt % 184 curing agent, dimethyl methylhydrogen siloxane, sylgard 184	Al: 168 ± 2 , 2024Al: 161 ± 2	< 5
Chemical etching[53]	Silicon	Acetone, Ethanol, Isopropanol, NaBF_4 , AgNO_3 , perfluorooctyltriethoxysilane(PFTS), Hexadecane, C_4F_8	C_4F_8 /PFTS: 160	/
Chemical etching[54]	Ti6Al4V	Fluoroalkylsilane-17 (FAS-17), Acetone, Alcohol	160	3
Chemical etching[55]	Magnesium alloy	AgNO_3 , ethanol, DTS ($\text{CH}_3(\text{CH}_2)_{11}\text{Si}(\text{OCH}_3)_3$).	138.4 ± 2	/
Chemical etching[56]	Magnesium	H_2SO_4 , H_2O_2 , stearic acid ($\text{CH}_3(\text{CH}_2)_{16}\text{COOH}$), ethanol	154	3
Spray coating[50]	Glass	Polystyrene (PS), Hydroxylterminated polystyrene (PS-OH), Toluene, Cyclohexane, Silica NPs, Flourinated silanes	170	0
Solution immersion [43]	Silicon	MeSiCl_3 toluene, ethanol	>170	0
Solution immersion[57]	Copper	Acetone, Ethanol, HCl, Nitrogen, Ethanolic stearic acid	156	4
Solution immersion [44]	Titanium	Alumina media, Isopropyl alcohol, Nitrogen, Colloidal silica, C_4F_8	152	/

Plasma[41]	Aluminum alloy	Methoxy- {3- [(2,2,3,3,4,4,5,5,6,6,7,7,8,8,8-pentadecafluorooctyl)oxy]propyl}-silane (MAF), decane, and 99.9% ethanol, C ₄ H ₄ O ₆ K ₂ ·0.5 H ₂ O, NaF SiO ₂	164.5 ± 3.3	8.2 ± 2.7
Plasma[58]	Poly(methyl methacrylate (PMMA)	iso-propyl-alcohol (IPA), O ₂ (99.95% pure), C ₄ F ₈ (99.995% pure)	152	5
Plasma CVD[42]	Silicon	Pentafluoroethane argon mixtures Fluorocarbon, Al ₂ O ₃ Fe, acetone, isopropyl, alcohol, CNT for CVD	166	<1
Self-assembled monolayers [45]	ZnO nanorod array film on cotton fabrics	zinc acetate dehydrate, sodium hydroxide, ethanol, zinc nitrate hexahydrate, hexamethylenetetra, n-Dodecyltrimethoxysilane.	161	9
Sand-blasting and acid etching (SLA)[46]	Titanium	Grits of 0.25–0.50 mm, HCl, H ₂ SO ₄ , N ₂ , NaCl	139.9	/
Electro-chemical deposition [40]	indium tin oxide (ITO)	Ethanol, n-dodecanethiol, poly(diallyldimethylammonium chloride) (PDDA), poly(4-styrene sulfonate) (PSS), H ₂ SO ₄ , KAuCl ₄	156	/
Slippery liquid-infused porous surface (SLIPS)[47]	Two porous solids: (1) arrays of nanoposts functionalized polyfluoroalkyl silane (2) random network of Teflon nanofibrous membranes	perfluorinated fluids	/	<5

2.2.2 Physical methods for fabrication of hydrophobic surface

Physical methods structure topographical features to create heterogeneous surfaces that can trap air in them and create conditions for high contact angle and possibly low wettability. The methods for fabrication of such topography are laser beam machining on metallic and non-metallic surfaces, electrical discharge machining and many others.

2.2.2.1 Laser beam machining on metallic surface

Laser beam machining (LBM) is a popular and widely used methodology to fabricate hydrophobic surfaces. It is simple, effective and flexible with high accuracy as well. This process uses thermal energy to remove material and it can be applied on both metallic and non-metallic surfaces. The laser beam generated by laser source passed through the attenuator which can control the beam power, then it goes to the expander and focus lens to obtain a finer and smaller spot size beam. A schematic view of the LBM process is shown in Figure 2.11.

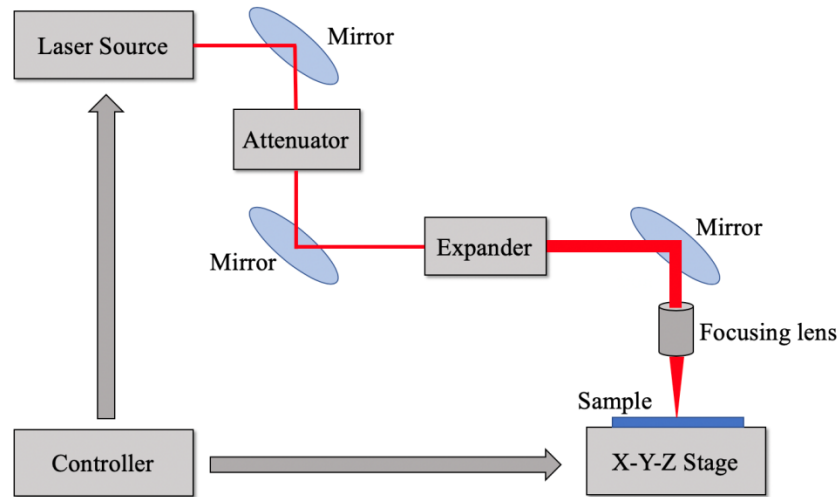


Figure 2. 11 Schematic view of the LBM process

For the metallic material machining, Tang et al. [6] used femtosecond laser beam on steel to create hydrophobic surface using the laser system with 800 nm wavelength, 100 fs pulse duration. The laser beam was focused to a small spot of a few micrometers in diameter using an objective lens and applied on the 2mm thickness steel film perpendicularly. They engraved grooves on the top surface of the steel sheet sample. The groove formed on the steel surface has a V-shape (shown in Figure 2.12 (a)) in the cross section and its dimension can be determined by a combination of the spot size, laser power and the distance from the target surface, laser focus point and the scanning speed. They applied the laser to the steel sheet forming grooves that were 20 μm apart and 4 μm in depth in two perpendicular directions that resulted in array of pillars as shown in Figure 2.11 (a). The laser beam scanned surface at 100mm/min speed by double passes of each groove. With these

structures the contact angle can be increased to 130° which is hydrophobic which is shown in Figure 2.11 (b).

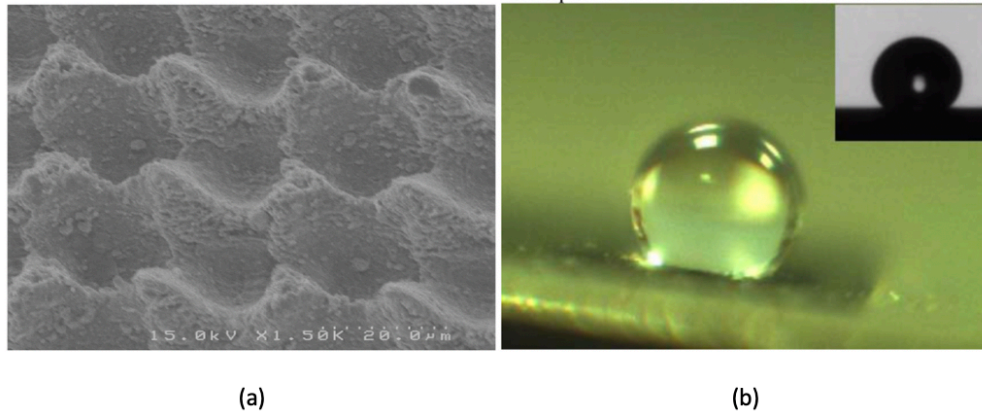


Figure 2. 12 (a) SEM image of micro-pillar arrays on stainless steel surface (b) Water drop on the laser fabricated stainless steel surface[6].

Although femtosecond laser is good for building periodic micro or nano pattern on the metallic surface, it is not suited for production due to its relatively low throughput [59], [60]. Chun et al. [61] used UV nanosecond pulsed laser which is faster to machine a pure copper plate with 2 mm thickness as a substrate. They applied laser beam to generate the grid pattern on the copper surface with burrs at the edges of the grooves formed with three different spacing between the lines: 100 μm , 300 μm , and 500 μm . The machined copper surface showed isotropic superhydrophobic properties in every direction [62][63]. The SEM images of the machined substrates with the different spacings are shown in Figure 2.13 [61].

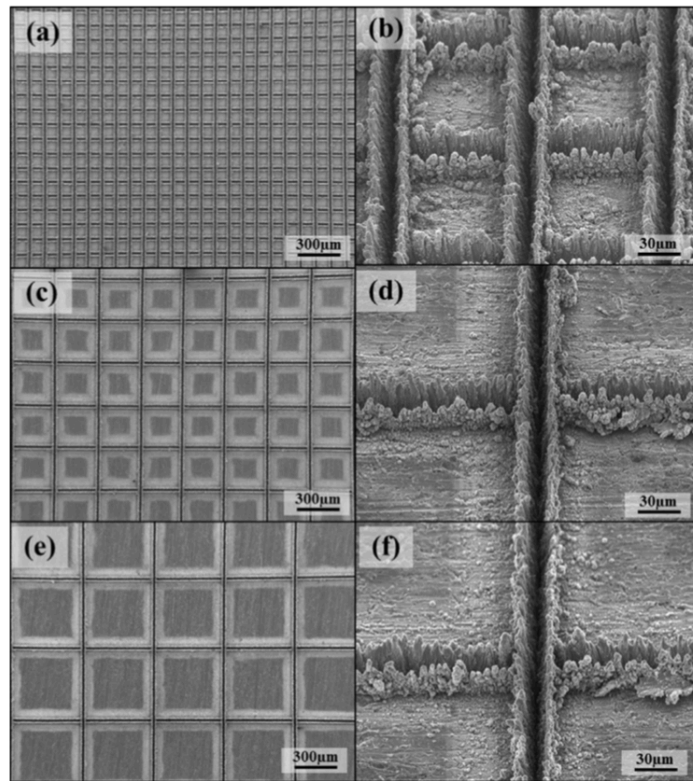


Figure 2. 13 SEM images of Laser beam machined surface: top images of (a) 100 μm spacing size, (c) 300 μm spacing size, (e) 500 μm spacing size and enlarged tilting image of (b) 100 μm spacing size, (d) 300 μm spacing size, (f) 500 μm spacing size [61].

Post processing of the laser textured surface to generate surface coatings have also been investigated. For example, ethanol has been used to accelerate the process of copper oxide formation on the surface [64]. The surface was covered with a thin layer of ethanol at 0, 0.5, 1 and 2 h post processing and then subsequently annealed at a low temperature of 100^o. CuO which is hydrophilic that was formed after laser machining was converted to Cu₂O

which is hydrophobic and this process was accelerated by ethanol. The schematic image of this process shows in Figure 2.14 [61].

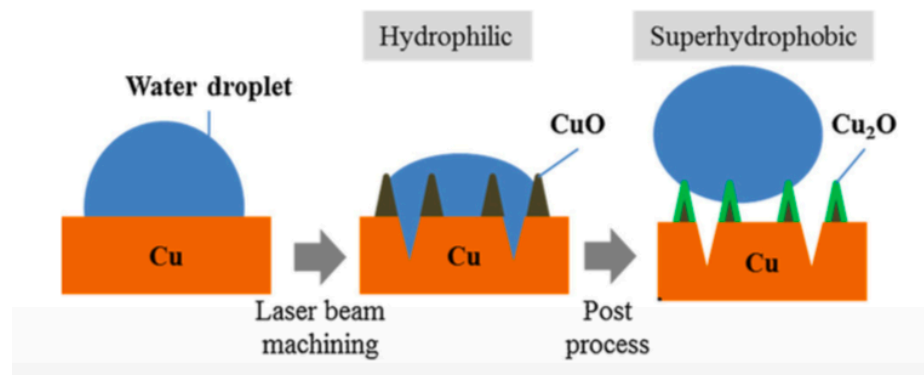


Figure 2. 14 Schematic of superhydrophilic and superhydrophobic surfaces with laser beam machining and post process[61].

The wettability measured by contact angle with 10 μ L and the results of three different spacing sizes showed in Figure 2.15. The contact angle of LBM surface with ethanol post-treatment was found to be 165°, 155°, and 157° with 100, 300, 500 μ m spacing size respectively. The sliding angle was around 9° of 300 μ m spacing size. Although the post treatment can reduce the overall surface preparation time, it still took around 5 hours to finish the whole process of LBM.

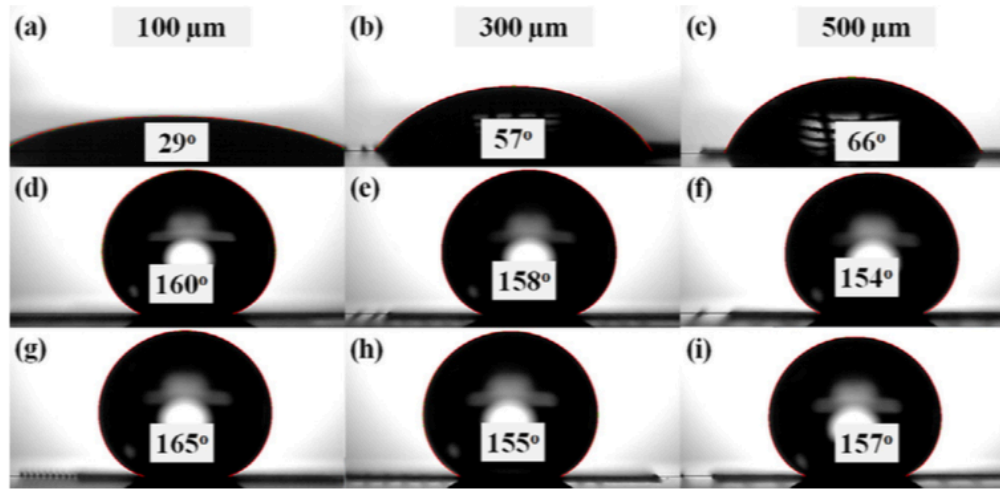


Figure 2. 15 Images of droplet contact angle: initial stages(a),(b),(c); after annealing without ethanol (d),(e),(f); and after annealing with ethanol (g),(h),(i); with 100, 300, and 500 μm spacing size respectively.

2.2.2.2 Laser beam machining on non-metallic surface

Laser micromachining has also been used to create microtextures on non-conductive materials such as sapphire to create hydrophobic surfaces. In addition, these microtextured surfaces have also been used as mold to cast elastomers such as PDMS to create inverse patterns that could also be hydrophobic. Davaasuren et al. [63] used this approach and laser machined sapphire using a nanosecond pulsed laser beam with 5 μm diameter to fabricate a textured surface with various spacings from 10 μm to 35 μm . They also used the textured surface as a mold and casted PDMS to form the inverse pattern that was hydrophobic. The

machined sapphire substrates are shown in Figure 2.16 (a)-(f) and the cast PDMS texture is shown in Figure 2.16(g)-(i) [63].

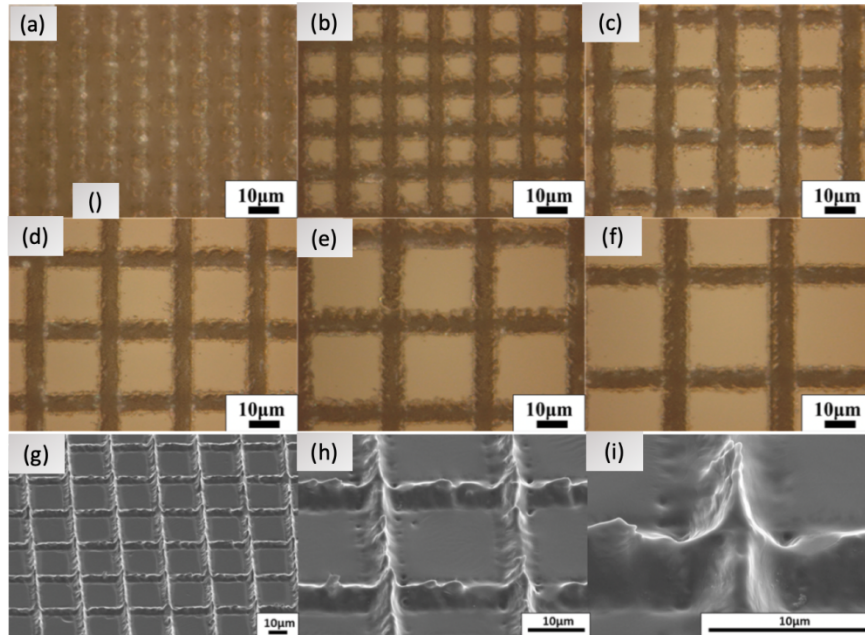


Figure 2. 16 Images of LBM results with different spacing size (a)10µm (b)15µm (c)20µm (d)25µm (e)30µm (f) 35µm. SEM images of PDMS casted surface with 25µm spacing size under (g)-(i)[63]

The contact angle of textured substrate was dependent on the spacing (Fig 2.17) between the ridges on the PDMS and was substantially different from flat PDMS (110°). The maximum contact angle obtained was 171° with 25 µm spacing. The smaller spacing produced a Cassie–Baxter state which resulted in higher contact angle. When the spacing

was 30 μm or above, the wetting state turned to Wenzel state with the liquid fully wetting substrate changing the contact angle significantly [63].

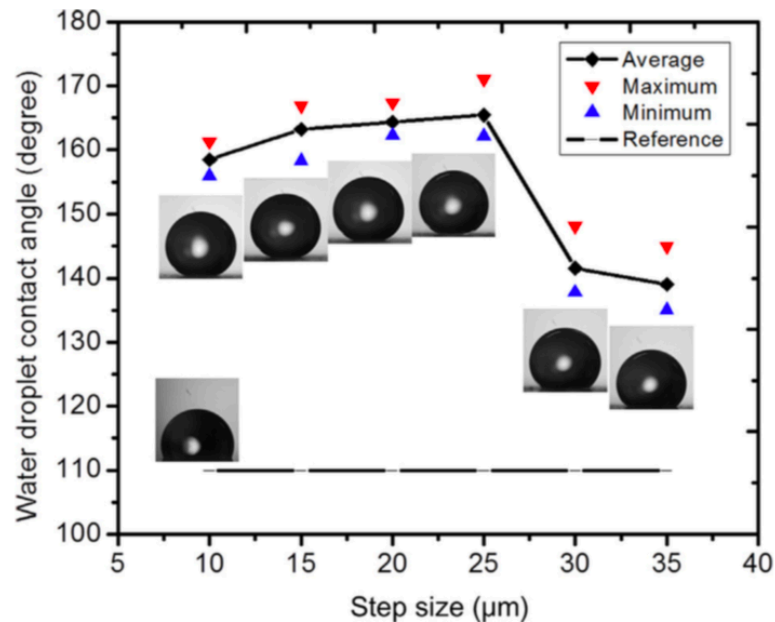


Figure 2. 17 Water droplet contact angles results for different grid spacing sizes[63].

Chun et. al. also used laser fabrication of sapphire surfaces [65] and used heat treatment as post-treatment process to generate textured hydrophobic surfaces. A UV nanosecond pulse laser was used to fabricate a 0.43 mm thick sapphire wafer which resulted in a textured but hydrophilic surface. Subsequent heat treatment at 200°C for six hours resulted in the replacement of the OH groups on the surface with methyl groups that were adsorbed from the organic matter in air to form a hydrophobic surface that has a contact angle of 176° and

a sliding angle of 4° . The surfaces thus formed demonstrated high water-repellence (Figure 2.18 (a)) was transparent (Figure 2.18 (b)) and had self-cleaning property (Figure 2.18 (c)).

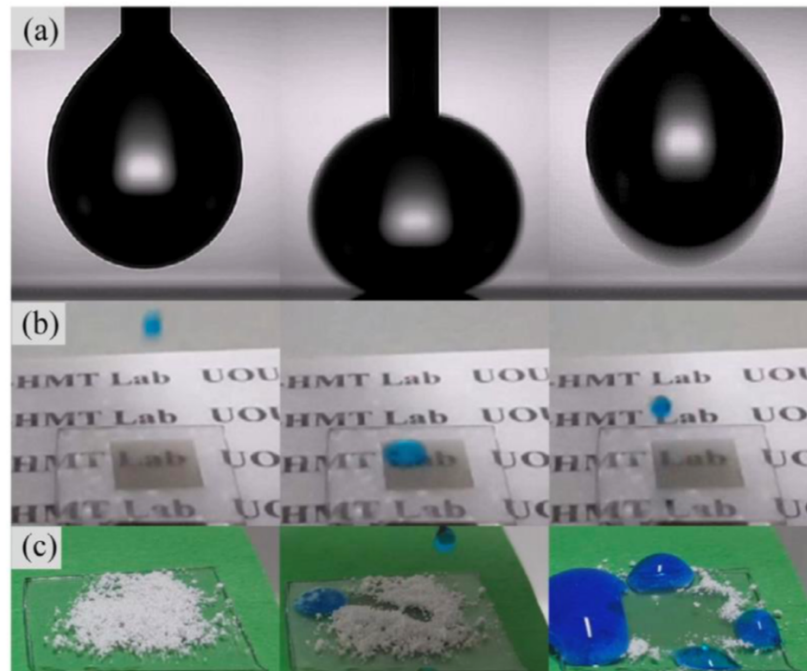


Figure 2. 18 Performance of laser machined sapphire surface: (a) surperhydrophobicity (b) water repellence and transparency (c) self-cleaning effect [65].

LBM is a fabrication method which can create micro and nanofeatures on metal as well as non-conductive materials. It has advantages like reproducibility, high precision and low contamination. However, the machining time of LBM process is relatively long. Another drawback of LBM is there must be a post treatment after laser machining to make it

hydrophobic. Exposure to air can also make it hydrophobic but the process takes a significant amount of time (11 to 12 days)[61].

2.2.2.3Electrical discharge machining

Electrical discharge machining (EDM) can also be used to texture a conductive surface. EDM uses electrical discharge between the tool and the workpiece to erode away the workpiece in selective areas. uses electricity as machining power source. There are two types of EDM, namely: sink and wire EDM. In sink EDM, a tool with the intended 3D shape is sunk into the workpiece gradually and through electrical discharges erodes away the workpiece to create an inverse feature. In wire EDM, the tool is a wire that is moved in two or three dimensions to form an outline that can carve out the intended shape from the workpiece. Various dielectric mediums such as hydrocarbon oil in sink EDM and deionized water in wire EDM are used to fill the gap between the tool and the workpiece in order to flush away the debris generated by the discharge process [66].

EDM methods have been used to texture the surface such that hydrophobicity can be achieved. For example, Weisensee et al. [67] used wire EDM to form hydrophobic and oleophobic surface on the steel substrates. They machined steel surface in two perpendicular directions to form micro-mushroom structures as shown in Figure 2.19.

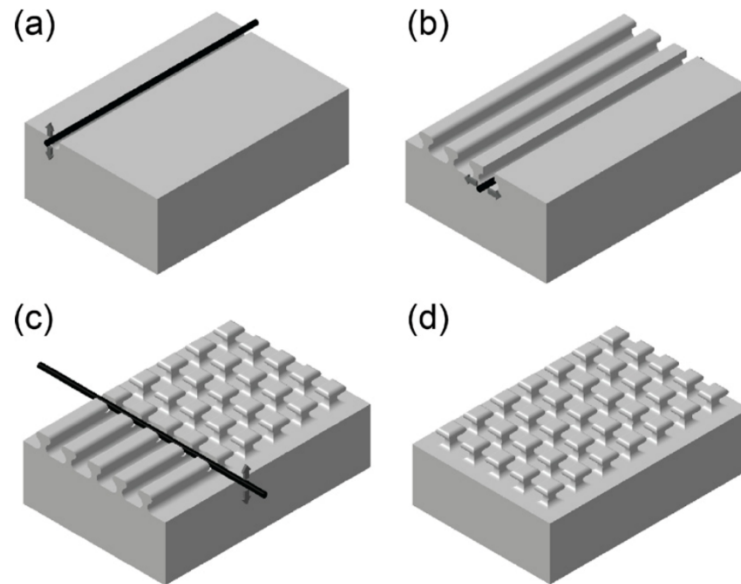


Figure 2. 19 Schematic view of micro-mushrooms fabrication process: (a) A wire cuts channels by vertical motion into a steel block and undercuts by lateral displacement in (b). Then the sample is rotated by 90° (c) and the procedure repeated until completion (d)[67].

The samples were subsequently coated in liquid Teflon to lower the surface's energy. Using deionized water and silicone oil they demonstrated hydrophobicity and olephobicity on these surfaces as shown in Figure 2.20. The highest contact angles achieved were 162° with a CAH of 19° , and 152° with a CAH of 70° for water and oil respectively.

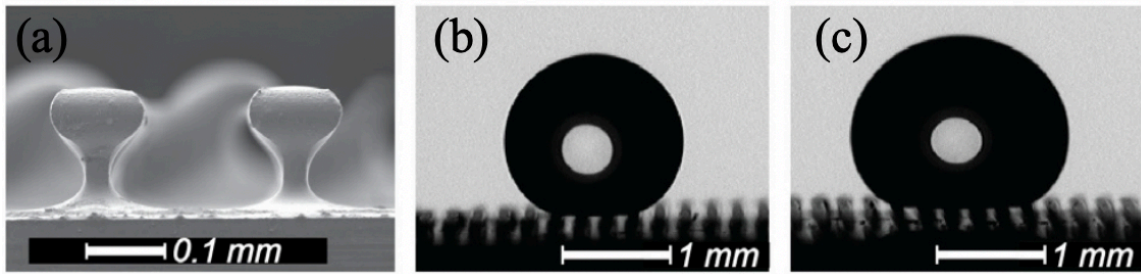


Figure 2. 20 (a) The figure of one micro-mushroom structure sample (b) the droplet states on this machined surface (c) a RL-68H oil sitting on this surface[67].

Alternatively, Guo et al.[7] also generated hydrophobic surfaces on Aluminum Alloy 7075 by sink EDM method. They used sink EDM machine and flat piece of copper as tool electrode material. After Sink EDM texturing, a contact angle $149.4^{\circ} \pm 0.77^{\circ}$ with a CAH of $15.3^{\circ} \pm 2.62^{\circ}$ was achieved. Figure 2.21 demonstrated the highly water repellency of this textured surface as compared with non-EDM textured polished surface.

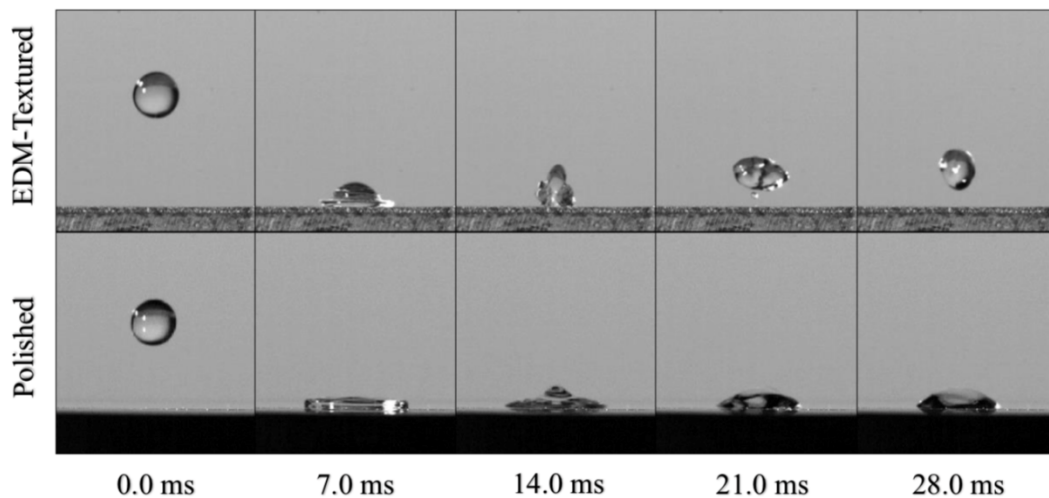


Figure 2. 21 Picture sequences of an impacting water droplet[7]

Although EDM is a low-cost and rapid method to form hydrophobic surface, it can only be applied on conductive materials limiting its application. Also, the wire EDM methods take a long time and the sink EDM methods do not demonstrate anisotropic surface textures. For non-conductive materials, it still needs other ways to change the surface properties.

2.3 Anisotropic wetting

All of the instances discussed earlier are based on isotropic wetting where the surface properties for wetting on an average are homogenous on the surface and similar in every direction. Alternatively, the properties could be changed or patterned in such a way that they are inhomogeneous or different along different directions producing a surface with anisotropic wetting characteristics. A droplet placed on such a surface will have two (or several) contact angles which are different along each of the principal directions in which the surface properties are different. The profile of the droplet from the top will be anisotropic, elongated along the direction where the contact angle is smaller (Fig 2.22). Such anisotropy of wetting properties can be attributed to physical discontinuity existing at liquid contact line or chemical heterogeneity on surfaces[9]. In addition to static conditions such as the contact angle, the dynamic properties such as CAH and sliding angle can also differ. Figure 2.6 (a) shows the schematic of anisotropic wetting as well as the contact

angle profile from Y direction (b) and X direction (c). The anisotropy in wetting can be characterized by several parameters. The distortion of droplet shape can be characterized by the width ratio ξ (Eq. 2.9) [9],

$$\xi = \frac{L_Y}{L_X} \quad \text{Eq.2.9}$$

where the L_Y is the length of the major axis of the droplet baseline (along the Y direction) and L_X is the width of the minor axis of the droplet baseline (along the X direction) (shown in Figure 2.22 a).

Another parameter of anisotropy is defined by difference between contact angles in the X and Y directions [9]:

$$\Delta\theta = \theta_Y - \theta_X \quad \text{Eq.2.10}$$

θ_X also called θ_{\parallel} is the contact angle observed by X direction, which is also described as the contact angle parallel with grooves. Accordingly, the contact angle observed along Y direction is θ_Y or θ_{\perp} , which is also described as the contact angle perpendicular with grooves.

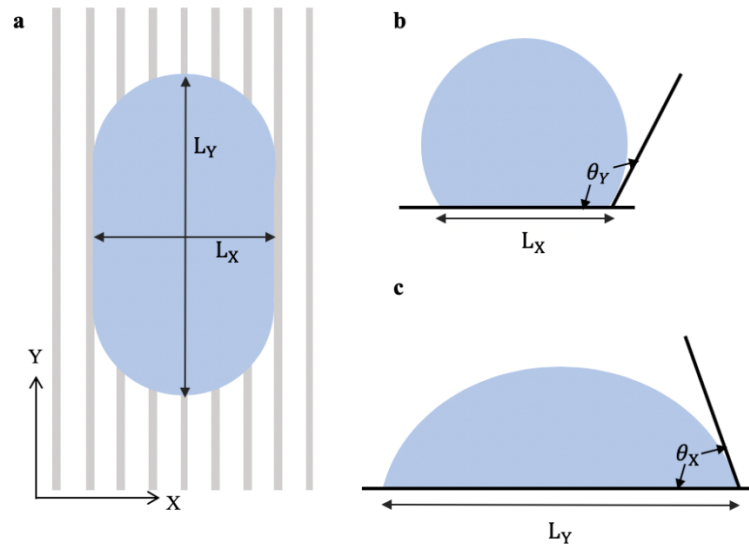


Figure 2. 22 (a) Schematic representation of a droplet upon the anisotropic wetting surface. (b) contact angle profile of θ_Y (θ_{\perp}), which is observed from Y direction. (c) contact angle profile of θ_X (θ_{\parallel}) which is observed from X direction.

2.4 Anisotropic wetting surface fabrication

The methods of anisotropic hydrophobic surface fabrication can be mainly divided by two different categories - chemically patterned surfaces and structural patterned surfaces. The chemistry of surface plays an important role to determine the anisotropic performance. The dimensions of micro- or nano-structures are critical to the structural patterned surfaces. In this section, several fabrication methods are reviewed which are more structural compared to chemical.

2.4.1 Photolithography based chemical modification

Photolithography is a widely used method of patterning in electronics and microfluidics. It has also been utilized to fabricate anisotropic wetting surfaces. Morita et al. [68] have published a report about the photolithographically patterned lines comprising alternating fluoroalkylsilane and silanol chemical groups forming anisotropic wetting surfaces. First, the entire Si substrate was coated with organosilane molecules such as n-octadecyltrimethoxysilane $[\text{CH}_3(\text{CH}_2)_{17}\text{Si}(\text{OCH}_3)_3]$, n-decyltriethoxysilane $[\text{CH}_3(\text{CH}_2)_9\text{Si}(\text{OC}_2\text{H}_5)_3]$, and perfluorohexylethyltrimethoxysilane $[\text{CF}_3(\text{CF}_2)_5\text{CH}_2\text{CH}_2\text{Si}(\text{OCH}_3)_3]$ by CVD. Next, the substrate was exposed to UV light at 172 nm through a photomask (line patterns from 1 μm -20 μm) which photo decomposed the organosilane in the exposed areas. These photopatterned substrates were found to strong anisotropic wetting property as shown in Figure 2.23. The orthogonal-direction static contact angles (78°-89°) of different line spacing (1 μm , 2 μm , 5 μm , 10 μm) were 10°-30° higher than parallel direction (60°-71°). The sliding angles of parallel direction were from 27° to 33°, while the orthogonal-direction sliding angle were all higher than 80°.

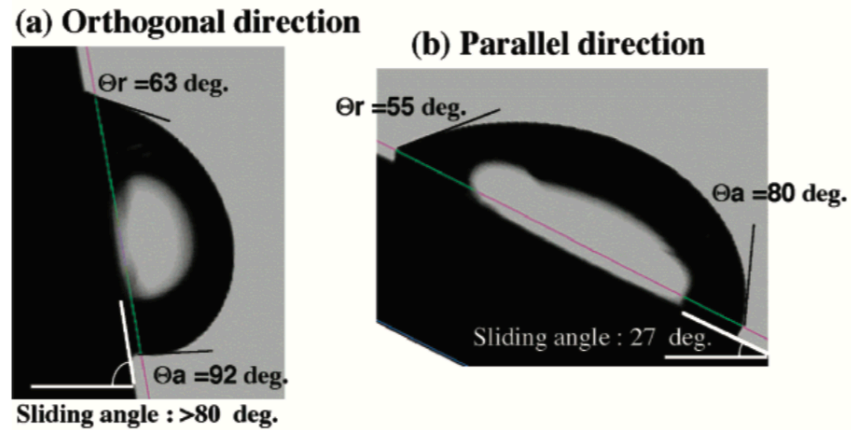


Figure 2. 23 The dynamic wetting of surfaces with line width $5\mu\text{m}$: (a) dynamic state in orthogonal direction (b) dynamic state in parallel direction [68].

Wang et al. [69] also used photolithography combined with chemical vapor deposition (CVD) to form periodic hydrophobic and hydrophilic striped structures. Oxygen plasma was used to modify the surface with $-\text{OH}$ groups. The silicon wafer was spin-coated by photoresist and patterned by photolithography with the stripe-patterned photo mask. Then trichloro- (1H,1H,2H,2H-perfluorooctyl) silane (PFS) was deposited on the wafer by CVD. Photoresist was removed with ethanol and dried with nitrogen. The contact angle of perpendicular direction was 75° and 104° in parallel direction.

Photolithography in combination with CVD is a convenient and established way to modify the surfaces heterogeneously with chemical groups. However, photolithography method needs clean room facilities which are expensive. Also, as with any chemical modification

method, the chemical modifications by itself may not be robust over long time when exposed to mechanical abrasion dust and debris contact or deposition.

2.4.2 Embossing

Embossing is an industrial process to create micro and nanoscale physical features on a wide variety of substrates. Liu et al. [10] utilized an embossing method to fabricate anisotropic wetting surfaces of aluminum foil. Embossing plates were made up of hard rubber with micrometer scale grooves with triangular or trapezoidal shapes. During the fabrication process, ambient temperature was set and the depth of grooves on the aluminum foil was controlled by embossing pressure. They found the minimum groove width was 30 μm and depth was 15 μm due to the limitation of embossing. The contact angles of orthogonal-direction were from 60.1° to 83.6° and the parallel-direction contact angle changed from 59.5° to 75.2° with different structure dimensions. The fabricated surface exhibited a small degree of wetting anisotropy which is less than 10° difference between orthogonal and parallel directions. The droplet state on unmachined and machined surface were shown in Figure 2.24. They demonstrated an inexpensively method to introduce micro-grooved topographical structures. Although it is a promising method, the hard rubber mold was originally fabricated using laser machining which is a sequential and slow process. Furthermore, this method is suitable to modify foils and thermoplastic materials but not hard and bulk metal surfaces or ceramics.

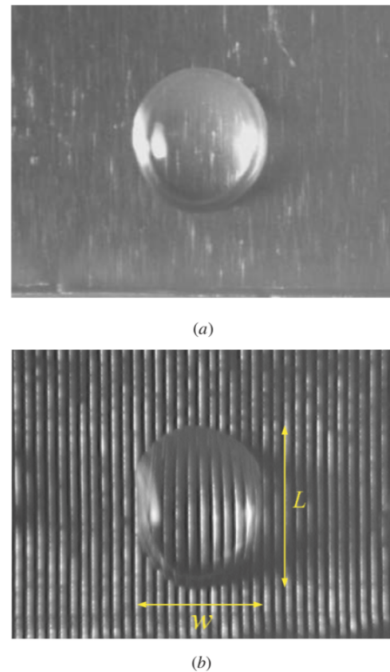


Figure 2. 24 Droplet state on (a) original Aluminum surface (b) aluminum surface after micro-embossing[10].

2.4.3 Nanoimprinting lithography

A variation of hot embossing which is the nanoimprinting lithography (NIL) can also be used to fabricate nano and sub microscale features. Zhang et al.[70] fabricated hierarchical structures on polystyrene (PS) and poly(methyl methacrylate) (PMMA) surface by NIL which showed significant anisotropic wetting. Two dimension of Silicon molds, $2\mu\text{m}$ pitch and 250nm pitch, were used to fabricate hierarchical structures. Molds were ultrasonic cleaned in isopropanol and rinsed by acetone followed by oxygen plasma treatment. After

treatment with perfluorodecyltrichlorosilane (FDTS) which can lower surface energy to help remove the mold after imprinting, the rest of the physisorbed FDTS was removed by heptane. PMMA and PS thin films were formed on Silicon wafer by spin coating and heat treatment. Then NIL was carried by the nanoimprinter under different conditions. The imprinting of the primary microstructures (line features) was performed at 130°C, 40 bar for 600s, and the imprinting of the secondary nanostructures was performed at 90 °C, 40 bar for 900s in an orthogonal directions. The imprinted features are shown in Figure 2.25[70], with various feature sizes and intersection angles between the micro and the nanofeatures on PMMA and PS substrates. The anisotropy of contact angles between the different imprint directions was 8° to 38° on PS surface, from 6° to 54°. The highest contact angle was 135° of 2 μm ⊥ 250 nm structure. The structures formed by NIL showed great anisotropic wetting property. However, the NIL usually used based on non-metallic surface and requires micro or nanostructured molds made by other direct write methods.

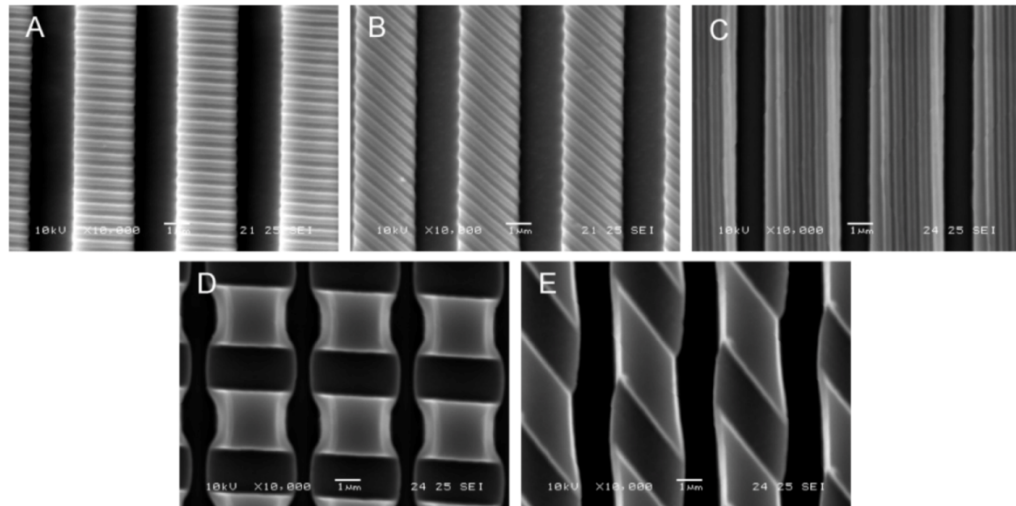


Figure 2.25 SEM micrographs for different hierarchical structures: (A) $2\ \mu\text{m} \perp 250\ \text{nm}$; (B) $2\ \mu\text{m} \angle 250\ \text{nm}$; (C) $2\ \mu\text{m} // 250\ \text{nm}$; (D) $2\ \mu\text{m} \perp 2\ \mu\text{m}$; and (E) $2\ \mu\text{m} \angle 2\ \mu\text{m}$. [70]

2.4.3 Surface wrinkled pattern

Surface wrinkled pattern which responds to mechanical stimuli are used to fabricate anisotropic wetting surfaces. Rhee et al.[71] fabricated surface with anisotropic wetting on pre-strained PDMS and silica-like (SiO_x) surface. The difference between contact angles were up to 13° . Lin et al. [72] used the sequential strain release and plasma ultraviolet ozone treatment to form hierarchical patterns on PDMS surface. Two level of wrinkles generated on the surface, first level with 700 to 1500nm wavelength and second level with 15 to $35\ \mu\text{m}$. The surfaces with wrinkled pattern had 3° to 9° of contact angle anisotropy.

2.5 Focused Ion Beam

All of the physical anisotropic patterning methods involve molds that are pattern using a direct write method. Laser micromachining is a popular direct write method to create features in the microscale. Increasingly, Focused ion beam (FIB) is a newer method that is being adapted for this purpose. FIB was originally developed as a tool to assist with the surface and material characterization in the nanoscale. But the increasing power and capability of these systems has opened the possibility of using them as a nanofabrication tool. In this section, the theory of FIB is introduced, as well as its machining performance.

2.5.1 Fundamental theory of Focused Ion Beam

Focused ion beam (FIB) was originally developed for material characterization and analysis, especially for transmission electron microscopy (TEM) sample preparation. FIB has been recently used in micro and nano structures fabrication mainly because FIB combines flexible micro- and nano- structures machining function and high-resolution imaging in one system. FIB technology is based on field- emitted ions from a liquid metal ion source, and the use of electric and magnetic fields to deflect the ion beams on to a surface to be machined. Current FIB systems are able to produce a beam with an excellent beam-positioning accuracy and stable operating condition, which enable the formation of micron-scale features with nanometer precision on almost any solid material including very hard

materials [73]. In modern FIB systems, the imaging resolution determined by the sputter-limited size which is usually about 10 nm [74]. It utilizes a beam of high energy ions to bombard substrate atoms where the collision transfers sufficient energy to the substrate atoms to overcome the surface binding energy leading to a physical sputtering effect [75]. The material of ion source determines the efficiency of sputtering process. There are a number of different types of liquid-metal ion source (LMIS). Gallium (Ga) has a significant advantage over other LMIS metals such as Bi, Sn, and Au because of its combination of low melting temperature (30 °C) and low vapor pressure. The low melting temperature makes the source easy to design and operate, and because Ga does not react with W needle (emission source) and evaporation is negligible and Ga-based LMISs are typically more stable than other LMIS metals [74]. In the system, a reservoir of Ga is positioned in contact with a sharp W needle. The Ga wets the needle and flows to the W tip. A high extraction field ($>10^8$ V/cm) is used to pull the liquid Ga into a sharp cone. Ions are emitted as a result of field ionization and post-ionization are accelerated in an electrical field of up to 30 KeV down the FIB column [76]. After ion beam strikes the specimen surface, the energetic ion transfers energy and momentum to substrate atoms. Some of the energized substrate atoms then have sufficient energy that they are ejected from the substrate and into the vacuum environment in a process called sputtering. Alternatively, some of the other incident Ga ions participate in a collision cascade that can result in the ion buried in the substrate or to emission of optical photons, X-rays and electrons as shown in Figure 2.26 [77].

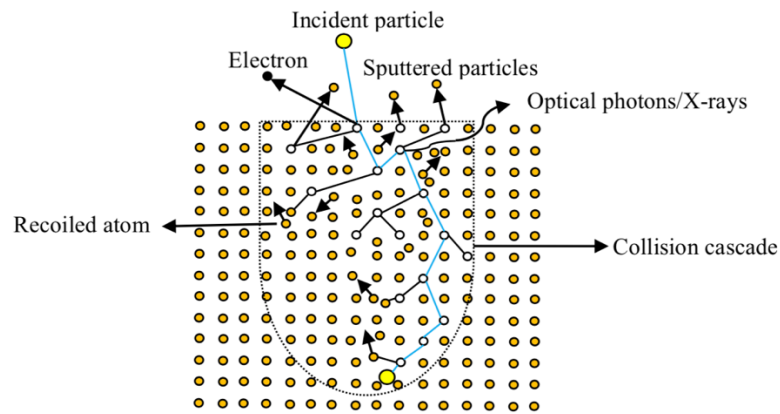


Figure 2. 26 Schematic diagram of various processes during ion interaction [77]

FIB instrument is shown in Figure 2.27 and consists of these main components: electron and ion source which emit electron or ion beam with controlled energy and small angular spread in a small spatial volume, lens system consisting of electromagnetic or electrostatic lenses, scan unit to scan signal and send back to deflection system to generate the image of sample surface, detection unit to pick up the particles generated by the reaction between beam particles and atom of specimen surface and turning to digital signal in order to display the image of sample on the control PC. SEM and FIB converge at a short working distance and a certain angle which is 52° . The schematic of two beam positions inside of the FIB machine is shown in Fig 2.28. SEM has a better resolution compared with FIB which is 1nm usually. Both SEM and FIB can be used as an observation purpose which are from two perspective, and FIB is also used to mill or remove specimen material.

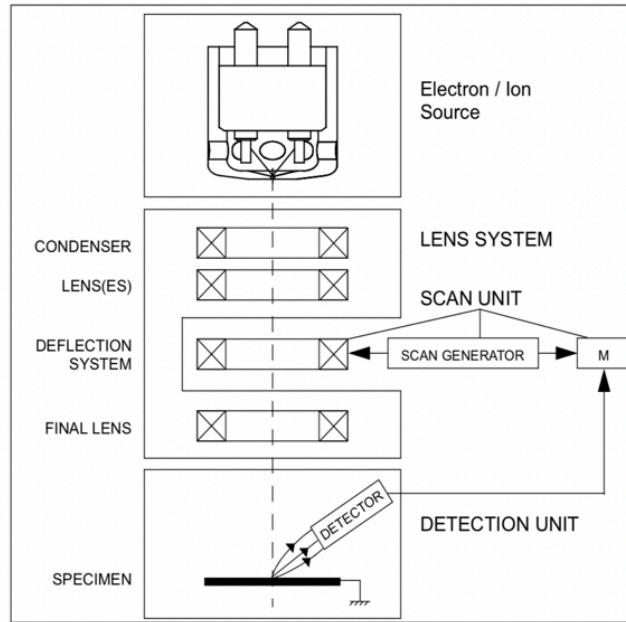


Figure 2. 27 Schematic column of main components[78]

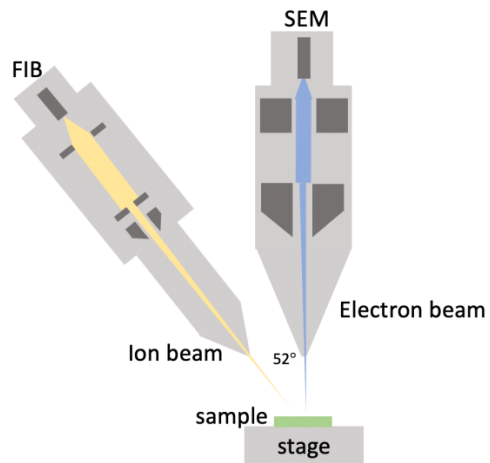


Figure 2. 28 Schematic of two beam positions

2.5.2 FIB for engraving topographical features on diamond tool

Focused ion beam has been recently used to create microfeatures on machining tools. Single crystal diamond (SCD) is a widely used material in cutting tools as it allows formation of very sharp cutting edges due to its crystalline nature. When the tools are applied on the single point diamond turning, these sharp cutting edges allow nanometer level surface finish even after a single cutting pass. The various methods available for nanofabrication such as FIB, scanning probe lithography and electron beam lithography, are all designed for fabrication on planar surfaces and have to be significant modified or adapted to be able to machine diamond tools. FIB machining is an ideal technique for obtaining structures at micro- and nano-scale, but it is limited by the low throughput [79]. Scanning probe lithography, in which a stylus is moved mechanically across a substrate surface to form a pattern, is more suitable for chemical modification of a surface rather than removal of material. It can only be used to fabricate materials which are softer than the stylus [80]. Although electron beam lithography can be used to fabricate over a large area which means it has a high throughput, it is only suitable for the fabrication of 2D structures on a planar surface. Among the methods available, FIB is more suitable method than other ways to fabricate the microstructures on diamond tools. Sun et al. [79] used FIB to fabricate diamond tools with protruding microstructures. They encountered issues such as ion beam drifting, sharp edge formation, ripples generation on the diamond surface, re-deposition

effect and beam tail effect during the diamond machining process. They fabricated protruding, triangular, periodical features that were $0.6\ \mu\text{m}$ in length and $0.15\ \mu\text{m}$ in width on the tool tip. The final fabricated structures are shown in Figure 2.29 [79].

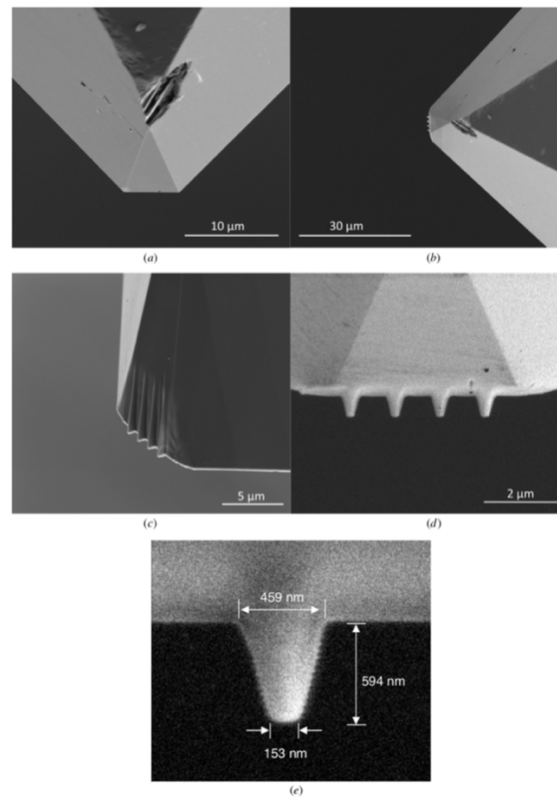


Figure 2. 29 Nanoscale SCD tool fabricated by FIB machining. (a) Original SCD tool; (b) a lower magnification view of the same tool after fabrication; (c) lateral view of the nanoscale SCD tool; (d) top view of the nanoscale SCD tool; (e) a view of the diamond tip under higher magnification [79].

This research demonstrated that FIB has ability to build micro- even nano-level structures on the SCD tool tip. However, the ability of such a tool to accurately replicate features on various materials, its form accuracy and the ability of such machined surfaces to have heterogenous functional properties and the property of surface after machining have not been characterized.

2.6 Summary

Based on the literature review above, hydrophobic surfaces of isotropic and anisotropic wetting are important in both research studies and commercial applications. Many fabrication methods have been developed to generate these kinds of surfaces. The primary methods have been to chemically modify the surface or to physically texture it. CVD deposition of hydrophobic materials such as fluorosilanes and its covalent attachment has been the primary method to form chemically modified surfaces. Photolithography has been a method that has been used extensively pattern such chemical groups on surfaces to create anisotropic wetting. However chemical modification methods suffer for long term reliability as they can be mechanically abraded easily. Alternatively, physical surface textures have been generated by primarily laser machining although EDM and other methods have also been used. These are either direct write methods and therefore slow or cannot create the anisotropic or heterogeneous properties for wetting. Therefore, a high throughput method that can be adapted to conventional machining method such as CNC

machining and can produce reliable micro and nanostructures to form anisotropic wetting surfaces is sought. Nevertheless, there is currently no method that can create.

Chapter 3: Experimental Set-Up and Methods

As described in the previous section, the FIB machined SCD tool is an excellent choice to create micro-structures on various materials that can facilitate anisotropic wetting. In comparison with other methods, the use of the micro-structured tool to CNC machine micro features onto substrates has high throughput, fast fabrication speed, and the tool can be used multiple times. In this chapter, the fabrication method of designed tool shapes is detailed. After the tool's fabrication, the tools were used to machine PMMA and 6061 Aluminum alloy by CNC machining. Different input parameters were changed during CNC machining. Surface characterization techniques, including confocal microscopy and scanning electron microscopy, that were used to characterize the samples after machining are described. Finally, contact angle of machined samples was measured and the process is described. The experimental process in this thesis is shown as a flow chart in Figure 3.1.

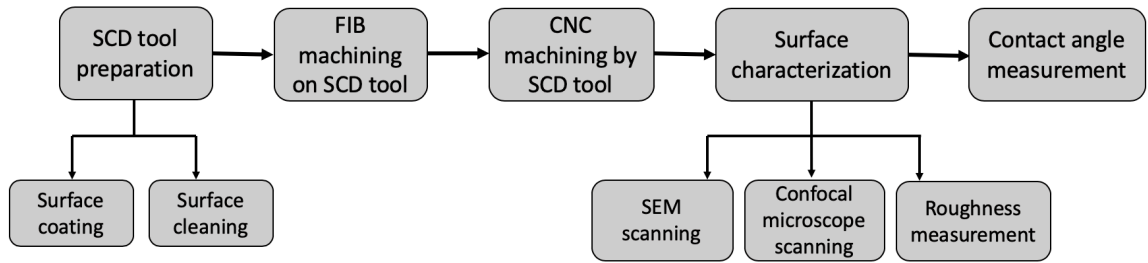


Figure 3. 1 Schematic of the experimental process

3.2 SCD tool microstructuring by FIB

The fabrication of microstructural features on the SCD tool was carried out on a dual-beam FIB system (FEI Versa 3D). The FIB system is shown in Fig 3.2.



Figure 3. 2 Picture of Versa 3D FIB system [78]

The working principle of the FIB instrument was introduced in Chapter 2. The main components of the system include two separate scan-beam generators for electron and ion beam. This kind of dual-beam system allows the milling and the observation of the process to be controlled by FIB and SEM independently. SEM and FIB converge at a short working distance and a certain angle, which is 52° . The schematic of two-beam arrangement inside of the FIB machine is shown in Fig 2.28. Two beams can activate quickly and accurately navigate between each other and milling the workpiece. The magnification of SEM is over

250,000 with high-resolution imaging which can be controlled by scan time, and the resolution of the ion beam diameter is 7nm. The gas injection system is installed in the instrument for deposition purposes. Usually, during the milling process, the SEM perspective is used to observe the specimen from the side view, and FIB can obtain the image from the top view. In this way, the condition of the sample can be monitored precisely and adequately. Optimum automation resolution and throughput are provided by this instrument to meet the requirement of micro or nanofabrication.

Before, the tool can be machined using FIB, it has to be prepared and cleaned. The following sections provide the details about these two steps.

3.2.1 Preparation of SCD tools

Preparation procedures of SCD tools are mainly based on two essential steps: surface cleaning and surface coating. The cleaning step was repeated both before surface coating and after it.

The SCD tool was cleaned thoroughly in order to remove dust, dirt and other debris as well as organic matter that may be present on its surface due to prior handling in room air. Presence of these contaminants on the surface could potentially affect the imaging and the machining of the tool tip. Isopropanol was used for washing and wiping the surface to remove large and visible debris. Then, Ultrasonic Cleaner (3 Quart GemOro Ultrasonics,

Gesswein) was used to clean the tool surface further in deionized (DI) water for 20 minutes and the tool tip was dried by compressed air.

The next step was coating the non-conductive diamond tool tip with a thin conductive metal layer in order to make the visualization through SEM better and make the machining more accurate. A thin gold layer (15 nm) was sputter-coated onto the diamond tool using a sputter coater machine (Edwards s150B) and produced a uniform film that prevented charging of the substrate when it was under an electron beam.

3.2.2 Focused ion beam machining

The SCD tool poses significant challenges during the FIB machining process due to its non-conductive nature. Although a thin layer of gold was coated on the tool's surface to improve the conductivity and prevent charge accumulation during FIB, this gold layer would be partly removed once the milling process begins, exposing the underlying non-conductive surface and subsequent charging. This is one of the significant challenges in FIB machining of non-conductive diamond tools. In this section, several machining protocols were investigated to identify the one that would mitigate this issue and provide reasonable replication of the designed features.

3.2.2.1 Dimensions of FIB machining on SCD tools

The SCD tools with flat tool edge were obtained from the K&Y diamond company. The design drawings for the as-fabricated tool are shown in Figure 3.3. In order to change the surface wetting ability, the physical method of microtexturing was used in this thesis to increase surface roughness with micro-structures. The initial design engraved onto the flat edge of the tool was a series of rectangular grooves that were equispaced. There were four SCD tools (tool#1, #2, #3 and #4) in total with different dimensions. Various dimensions of the square grooves and pitch spacing were engraved into the tools to characterize the process of transfer of patterns from the tool to the workpiece and also study the effect of those features formed on the wetting characteristics.

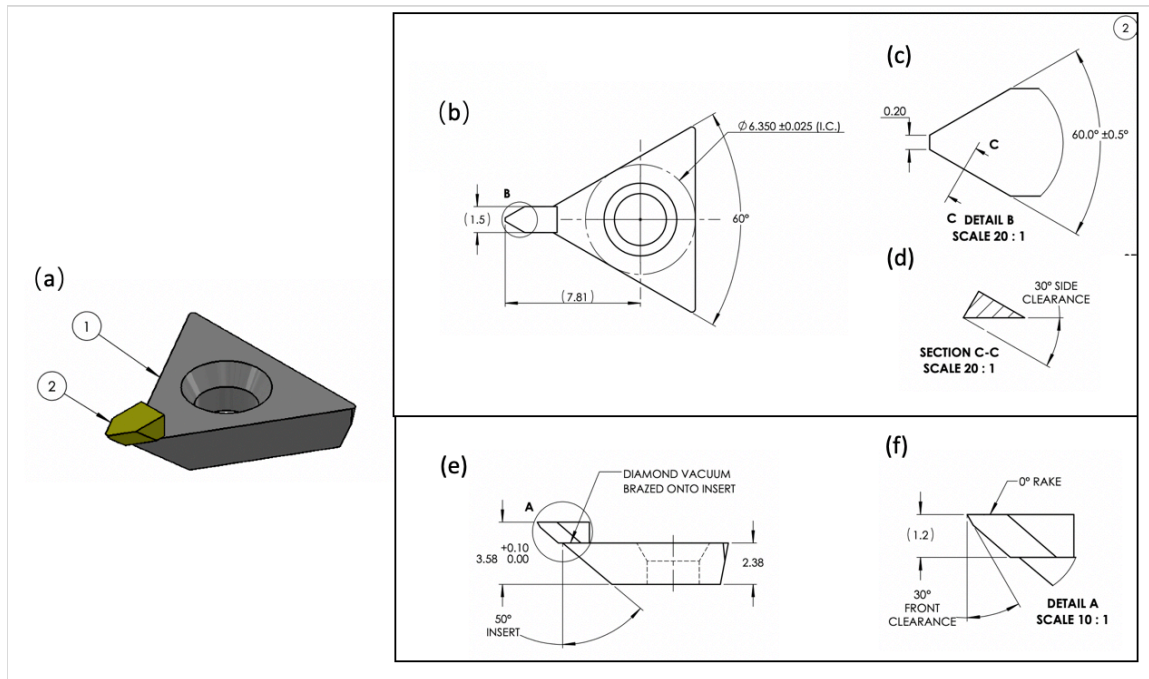


Figure 3.3 Design drawings and dimension unit (mm) (a) 3D design of SCD diamond tool and tool holder. (b) top view of tool and dimension of details (c) details of tool tip design from top view (d) cross-section view of tool tip (e) side view of tool and dimensions (f) details of tool tip from side view.

3.2.2.2 Process of FIB machining

First, the sample was loaded in the chamber of the instrument and fixed on the computer-controlled high accuracy five-axis sample stage. The stage area is 150x150 mm with 150 mm (from -75 mm to +75 mm) movement restriction in both X and Y directions and 10 mm in the Z direction and a 0.1 μm step size. The stage also has tilt limit from -10° to $+60^\circ$, is capable of being rotated by 360° rotation with 0.1° increment. Once loaded and

sealed the chamber is evacuated down to 1.96×10^{-6} Torr to create a vacuum environment during operation so that focused beams of ions and electrons could be used. The FIB machining process is initiated by tilting the tool tip sample such that the angle between the FIB beam with tooltip surface was 84° as shown in Figure 3.4. All the channels were sputtered by a beam of a fixed acceleration voltage of 30 keV incident ion in this thesis. The design for machining is loaded on and appropriate tool path is determined by the software. In the case of machining conductive materials such as Silicon, the software generated tool path was sufficient for accurate machining. For SCD tools, which were non-conductive, a multistep machining process was designed and they were performed in sequence. Unlike conventional machining where only a thin surface layer is removed or structured, here the features cut into the tool is a through cut. Therefore, these features which were in an array were cut one at a time to completion rather than in parallel using a layer by layer approach. A multi-step FIB machining process was also used to improve the ability of FIB to accurately machine non-conductive samples. The schematic of procedures is shown in Figure 3.5. The ion beam scanned the surface with a current of smallest current (0.3nA for tool #1 and #2, 1nA for tool #3 and #4.) to remove the material of the first step. The structure built in this step was much smaller than the target. The second step was aimed at broader and deeper structures with the design width (a) and smaller height (h) meeting the target design. In this step, 0.5nA and 3nA of current were used respectively. After that, 1nA and 5nA of current were used to build the final structure, which was the same with

design in table 3.1. Although the coating layer was removed at the beginning of milling, the multi-step method reduced the accumulation of incident ions and electrons and prevents the beam drifting to a great extent.

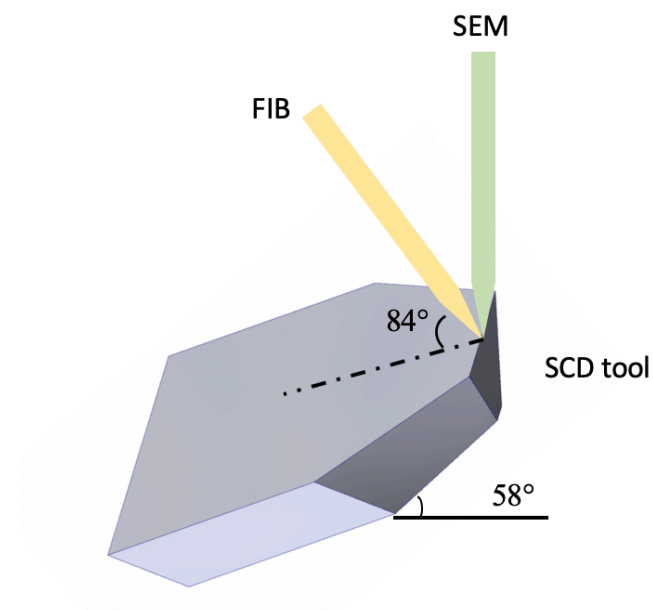


Figure 3. 4 Schematic of position relationship during FIB milling. FIB had an 84-degree intersection angle with an SCD tool surface after tool rotating 58 degrees.

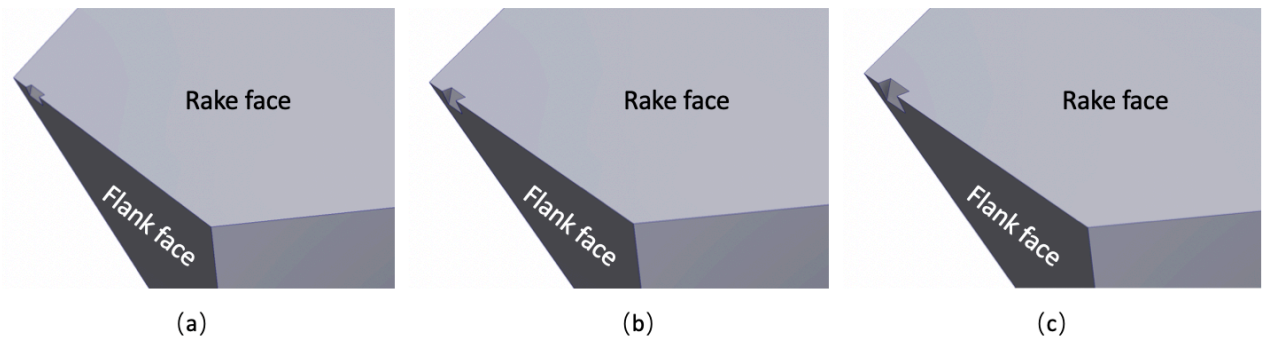


Figure 3. 5 Schematic of multi-step FIB milling procedures

3.3 CNC machining

After the texturing of the tool's tip, they were used to cut a variety of substrates using a high precision CNC machining system (MICROGANTRY nano 5X from Kugler GmbH, Salem, Germany) which is shown in Figure 3.6 located at National Research Council, London, ON. The main components of MICROGANTRY are a Renishaw touch probe, machining spindle, laser beam delivery system, a five-axis controlling sample holder (motion stage), light source, and a live camera. First, the SCD tool was fixed on the tool holder. Then the PMMA or Aluminum6061 alloy sample was immobilized by the holder on the five-axis stage. Air bearings control the five-axis motion stage with 10nm resolution for actual positioning. The five-axis includes X, Y, Z, rotation along the Z-axis (C axis) and tilt along the X-axis (A-axis). The positioning accuracy of the X and Y direction is

within ± 250 nm. The Z-direction positioning accuracy is ± 500 nm. For linear movement, the accuracy of the straightness profile is within ± 800 nm per 100 mm moving distance. After every reorientation of the sample, the touch probe was used to reestablish the references for the Z and the Y axis positions with a reference point on the tool. The accuracy of the touch probe is ± 500 nm. A separate control panel controls the motion and machining parameters, and the tool path can be provided as a G code. The code then was modified based on the machining parameters. In this step, different machining parameters were set to compare with each other, mainly based on cutting depth, cutting speed. In general, three different cutting speed was established, and three different cutting depth was set based on tool #3. The final cutting depth was achieved in increments of 2 μm steps instead of cutting the whole depth one time to avoid the damage to SCD tools.

Two directional machining was also conducted on the PMMA surface as well. This process contained two steps. Initially the PMMA sample was cut in one orientation Next, the sample was rotated by a specific angle and cut in the same area with different cutting depth as compared to the first cut.

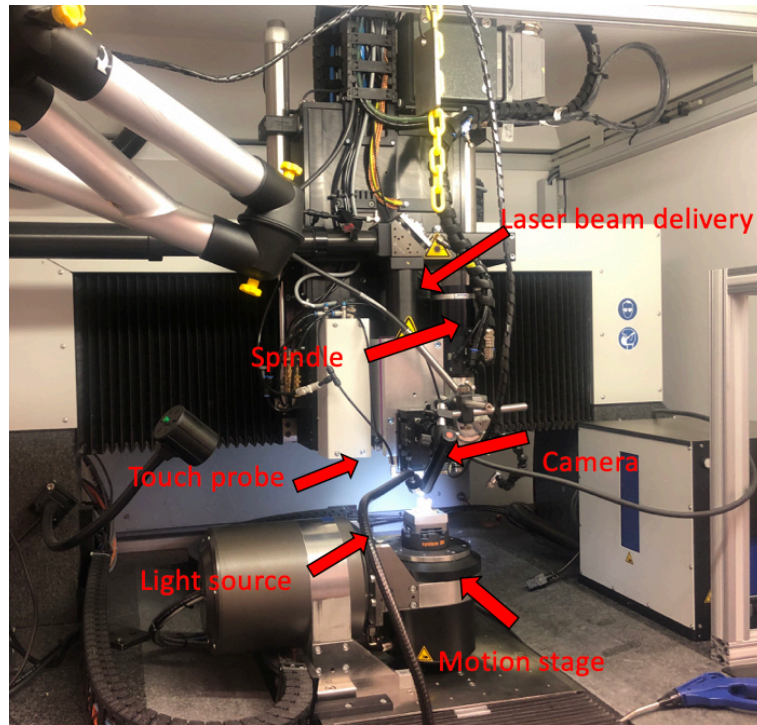


Figure 3. 6 MICROGANTRY system and main components at National Research Council (NRC), London,

ON

3.4 Surface characterization

Surface characterization is a crucial step measuring the properties of FIB built SCD tool machined surfaces. Three different methods were used to characterize the surfaces. First, in-situ real time observation of the evolving tool topography was performed using the dual-beam system in the FIB machine. After CNC machining, a confocal microscope was used

to scan and analyze surfaces. To determine the roughness of structures built on the surface, Alicona InfiniteFocus G5 conducted a roughness measurement step.

3.4.1 In-situ SEM analysis

The scanning electron microscopy system attached to FIB was used to obtain images of the structured surface before, during, and after the machining process. The in-situ observation was used to recalibrate machining and avoid accidental damages to the tool. Before machining, the original SCD tool's images taken by SEM as shown below in Figure 3.7 from two different view angles, top and perspective views to characterize the shape of the SCD tools. During the machining process, the tools were imaged in a similar manner to ensure that accurate feature representation was being produced as well as to ensure that there are no unintended damages to the tool and its tip.

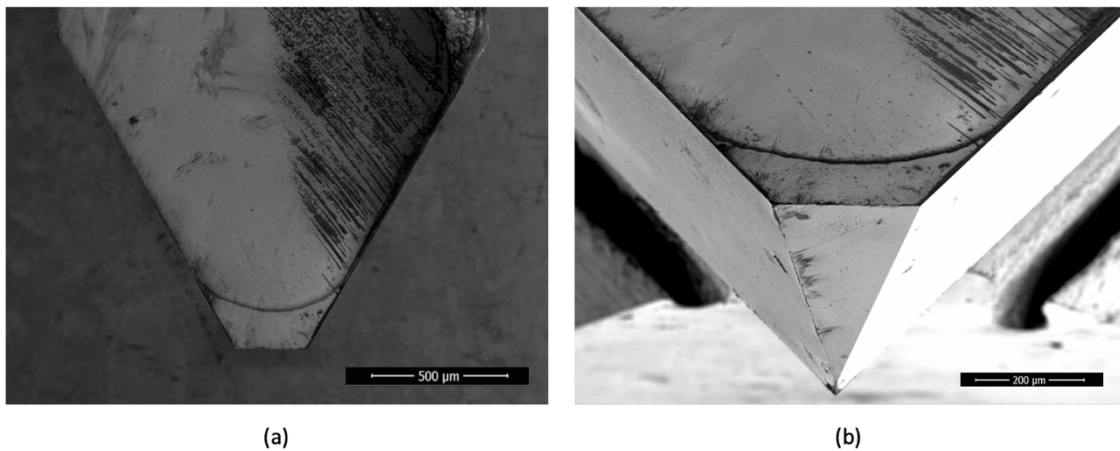


Figure 3. 7 SEM images of the original SCD tool (a) Top view of the rake face, (b) Perspective view after tool tilting to 58°.

3.4.2 Confocal microscope structure characterization

The confocal microscope was used to obtain surface texture and other surface information. In order to know the texture made by CNC machining, the machined surfaces were analyzed and scanned under SENSOFAR® METROLOGY S Neox 3D Optical Profiler located at National Research Council (NRC), London, ON which is shown in Fig 3.8. It has three different modes to measure surfaces, namely: focus variation, white light interferometry, and confocal. The confocal profiler was used in this thesis to measure micro-scale and nano-scale features. SENSOFAR® METROLOGY has Microdisplay Scan Confocal Microscope (ISO 25178-607) technology based on programmable array microscope (PAM). The electronically controlled spatial light modulator (SLM) with different light sources which can provide a set of pinholes that block out-of-focus light is installed in PAM. Ferroelectric liquid crystal on silicon installed inside provides a fast switch with no moving parts, which made the system more stable. It also provides a high resolution down to 0.01 μm . The high numerical aperture (NA) up to 0.95 and high magnification up to 150X enable it to measure up to 71° inclined smooth surfaces and 86° inclined rough surfaces. The lowest magnification is 2.5X of this microscope.



Figure 3. 8 SENSOFAR® METROLOGY S Neox 3D Optical Profiler located at National Research Council (NRC), London, ON [81]

After CNC machining, all the samples were prepared by wiping the surface with isopropanol. The scan of the sample produces a surface profile from which arithmetical average roughness (R_a) and dimensions of microstructures can be obtained. These results were tabulated for the various machining conditions and for different tool tips.

3.4.3 Surface roughness measurement

Although the surface roughness of surfaces can be obtained by the confocal microscope it does not work well on intentionally textured surfaces. In order to know the surface quality

under different CNC machining conditions and the influence of surface roughness with wetting ability, the arithmetic average roughness (R_a) of the surface was measured by Alicona Focus variation microscope in this step. Alicona Infinite Focus G5, which is shown in Figure 3.9 is a fast, accurate, non-contact optical measurement system to analyze 3D surface structures and surface roughness with very high resolution up to 10nm. The magnification range is from 2.5X to 100X. The measurement principle is based on Focus Variation. Focus Variation was developed from white light interferometers, which used the light path from the surface of a target object to a certain point to measure the distance and get the surface roughness. The modulated illumination system has a varying illumination intensity, like ring light illuminator, allows the measurement of slope angles as high as 87° . The focus variation system can capture not only the data of surface structures but also get the exact color information that will help to build the 3D model of the specimen. This technology is much more tolerant against vibrations compared with other microscopes.

After cleaning samples by isopropanol and ultrasonic cleanser, the 6061 Aluminum alloy samples after CNC machining with 15 mm x 15 mm area were put under 10X objective lens and scanned by Alicona. A 3D profile was generated after scanning, and then the surface slopes were eliminated by form removal if the signed form has been detected in the 3D model in order to determine the real roughness of the surface. After form removal, R_a was calculated based on the 3D profile built by scanning data from more than ten thousand scan points with the direction which was parallel to the surface ridges on the surface region between

each cutting pass. For each sample, the measurement of R_a repeated three times. The results of R_a were good sources to know the surface property and quality of CNC machining.

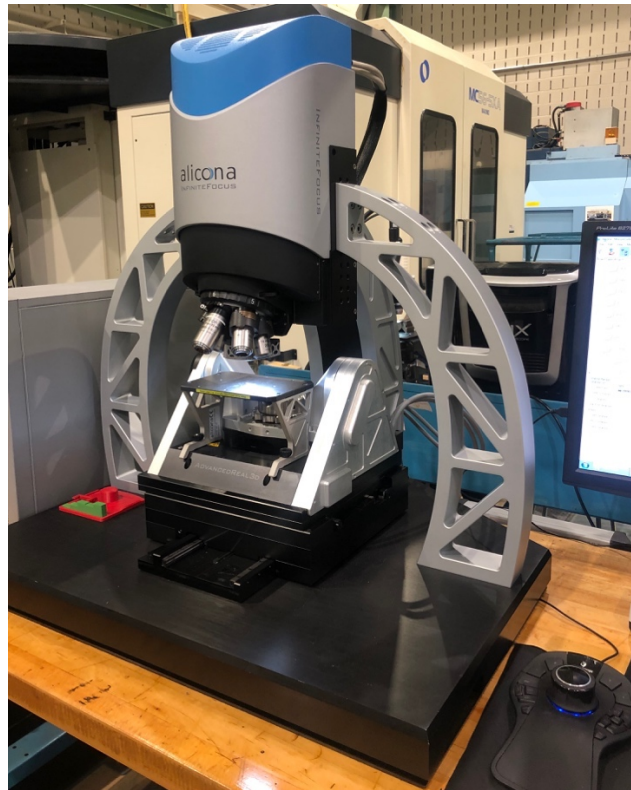


Figure 3. 9 Alicona Infinite Focus G5

3.5 Contact angle measurement

In order to know the wetting ability of all the surfaces after CNC machining, contact angle measurement is a necessary step after CNC machining. Here fully automatic video-based high-speed contact angle measurement instrument OCA35 was used to obtain the surface

contact angles. The equipment can be used to measure the contact angle on a plane or curved surface. OCA 35 can be used to measure contact angle range from 0° to 180° with $\pm 0.1^{\circ}$ precision. The instrument and its main components are shown below in Figure 3.10. The instrument comes with a USB-CCIR camera on the left side, and halogen light, electronic multiple dosing systems contain a set of needles with different diameter can be changed based on various purposes.

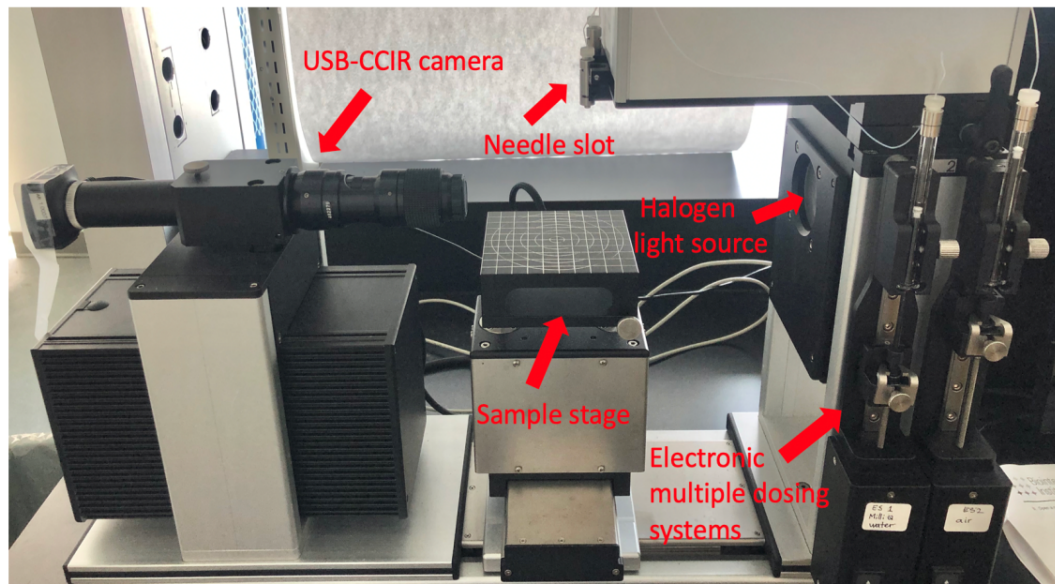


Figure 3. 10 OCA 35 contact angle measurement instrument and its main components.

Before contact angle measurement, an essential cleaning step was performed to avoid the influence of surface contaminator. The PMMA surface is cleaned by ethanol and flushed with DI water, then dried by high volume airflow blowgun. For Aluminum samples,

ultrasonic cleaning mentioned before was used for 15 minutes and dried by air blow gun as well.

For the contact angle measurement, the sessile droplet method was used in this thesis. First, the sample was placed on a 100 mmx100 mm sample stage, which can move in X-, Y-, and Z- directions with 100 mm, 100 mm, 50mm travel distance respectively with ± 0.01 mm accuracy in the sample plane direction and ± 0.005 mm perpendicular. The moving speed of the stage is from 0.13 mm/s to 3.95 mm/s controlled by an auto control panel. The stage was moved until the surface area that is to be measured displayed on the screen. A 0.5 mm diameter needle was used to dispense a 2 μ L droplet of DI water at a dosing speed of 1 μ L/s. The software-controlled dosing rate can be adjusted from 0.06 μ L to 26.4 μ L/s, and the volume range is from 50nL to 499.9 μ L. The pick-up method as shown in Figure 3.11 was used in order to dispense the droplet which was attached to the needle tip onto the substrate. SCA 20 software was used to capture the image of the droplet and calculate the contact angle fitting four different models, namely: Tangential, Young-Laplace, Circle and Ellipse. The first step was the baseline setting which can be set automatically or manually. For the Tangential and Young-Laplace method, the automatic detection baseline and outline were selected to calculate the contact angle. As for the Circle and Ellipse method, manually mode was used to get the baseline and outline. In this step, the operator chose enough points on the outline of the droplet to form an ellipse or circle shape, which could fit the shape of the droplet very well. As the last two methods were manual, they had higher variations and

errors. Each measurement was repeated 5 times, and the average value and the standard deviation were calculated.

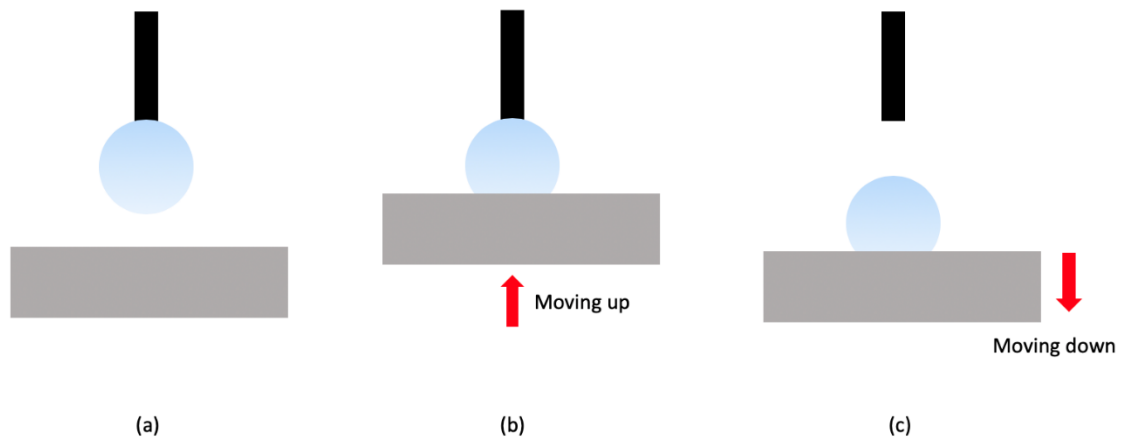


Figure 3. 11 Schematic of pick-up droplet process

The sliding angle of PMMA samples was measured based on the device shown in Figure 3.12. The sample was fixed on the slope surface by two-side tapes, and the arm was used to gradually adjust the slope angle until the droplet started rolling off. The phone camera was used to capture the images of rolling off-angle from the side view. Then, ImageJ software was used to measure the angle of the slope, which was a sliding angle of the sample. Each sample was measured from two directions three times.



Figure 3. 12 Device used to measure the sliding angle

Chapter 4: Results and discussion

In order to form periodically textured surfaces that could provide pinning locations and influence the contact angle, a single point tool could be used. Alternatively, the machining process could be parallelized if the tool were to be microstructured such that conventional machining processes can be used. This chapter presents the experimental results for the fabrication of the microstructured SCD tool tip as well as the surfaces produced when those tool tips are used to CNC machine various materials. The contact angles of the machined surfaces were also measured and the effect of various parameters in machining and its effect on the contact angle obtained discussed.

4.1 FIB milling of tool tip

In order to realize the designed micro structures on the SCD tool by FIB milling, a multi-step milling method was devised. This multistep process was specifically designed to avoid the charging of the workpiece during machining which occurs when FIB is used to machine non-conductive workpieces. The charging leads to image distortion which affects the feedback provided to the software about the machining process and also deflects the

incoming beam that can then remove material elsewhere further distorting the microstructures that are machined. The multistep process overcomes this issue by breaking up the final design of the microstructure into smaller ones that could be machined at higher current densities, sequentially. The initial design tested was a groove that had a dimension of $5\mu\text{m} \times 5\mu\text{m}$ on the rake face of the tool. Since the flank face is at an angle to the rake face and the groove was machined with the ion beam perpendicular to the rake face, it will produce a tapered groove with the cross-sectional dimension of the groove reducing along its axis into the face of the tool. This feature produces the clearance needed to allow a clear path for the material that is not machined to remain on the workpiece creating the intended feature. The schematic of multi-step machining of a single groove pattern is shown in Figure 4.1a as a perspective view and the top view of the rake face (Fig 4.1b). A three-step process was used to fabricate a $5\mu\text{m} \times 5\mu\text{m}$ groove on the rake face. The current in three different steps were 1nA, 3nA and 5nA. The dimension of first step feature was $3\mu\text{m} \times 3\mu\text{m}$ and was machined using a beam current of 1nA resulting in a milling time of 4 minutes (shown as a yellow outline in Fig 4.1b). The ion beam was scanned in the box area of designed structures in the serpentine pattern. Then, a 3nA beam current was used to machine the second step feature with dimensions of $5\mu\text{m} \times 3\mu\text{m}$ structure in 4 minutes (shown as a blue outline in Fig 4.1b). After that, a $5\mu\text{m} \times 3\mu\text{m}$ groove on SCD tool tip was milled under 5nA current for 2 minutes (shown as a green outline in Fig 4.1b). Multiple grooves that were equispaced, as shown in the schematic in Fig 4.1c, were machined

using this procedure. Four different diamond tools were microstructured by FIB with various sized of the microfeatures whose dimensions are shown in Figure 4.1c. The SEM image of one of the microgrooves that were machined is shown in Figure 4.2a. This feature had a dimension of $5\mu\text{m}\times 5\mu\text{m}$ on the rake face of the tool. The dimension of machined structure was found to be $5.4\mu\text{m}\times 5.8\mu\text{m}$ on the rake face. The variation in dimension compared with design was 16% in this case. The top view of the rake face of all machined tool tips are shown in Figure 4.3.

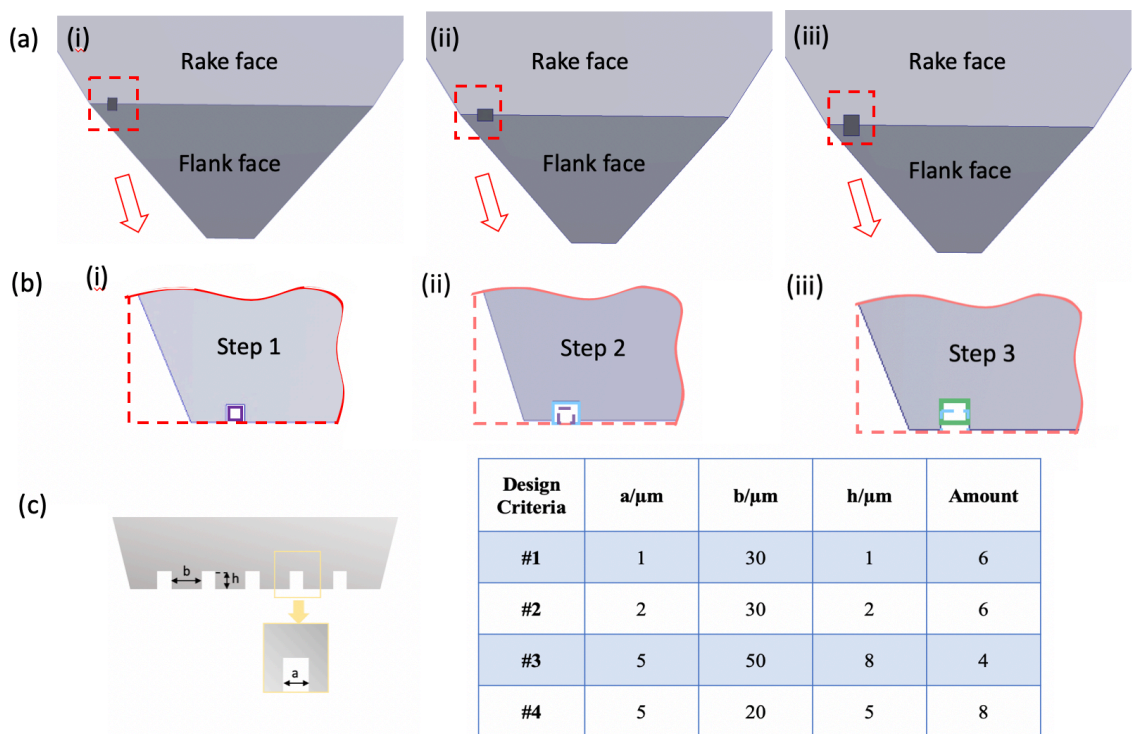


Figure 4. 1 Schematic of FIB milling process from SEM view based on Figure 4.1. (a) Schematic of milling steps from SEM view. (i) is the first step (ii) is the second step (iii) is the third step. (b) Schematic of FIB

milling steps from top view of the tool. Red box represents the zoomed representation of the area where the FIB milling occurs. (i) is the first step with $3\mu\text{m} \times 3\mu\text{m}$ area (ii) is the second step with $5\mu\text{m} \times 3\mu\text{m}$ area (iii) is the third step with $5\mu\text{m} \times 3\mu\text{m}$ area. (c) Dimensions of four SCD tools

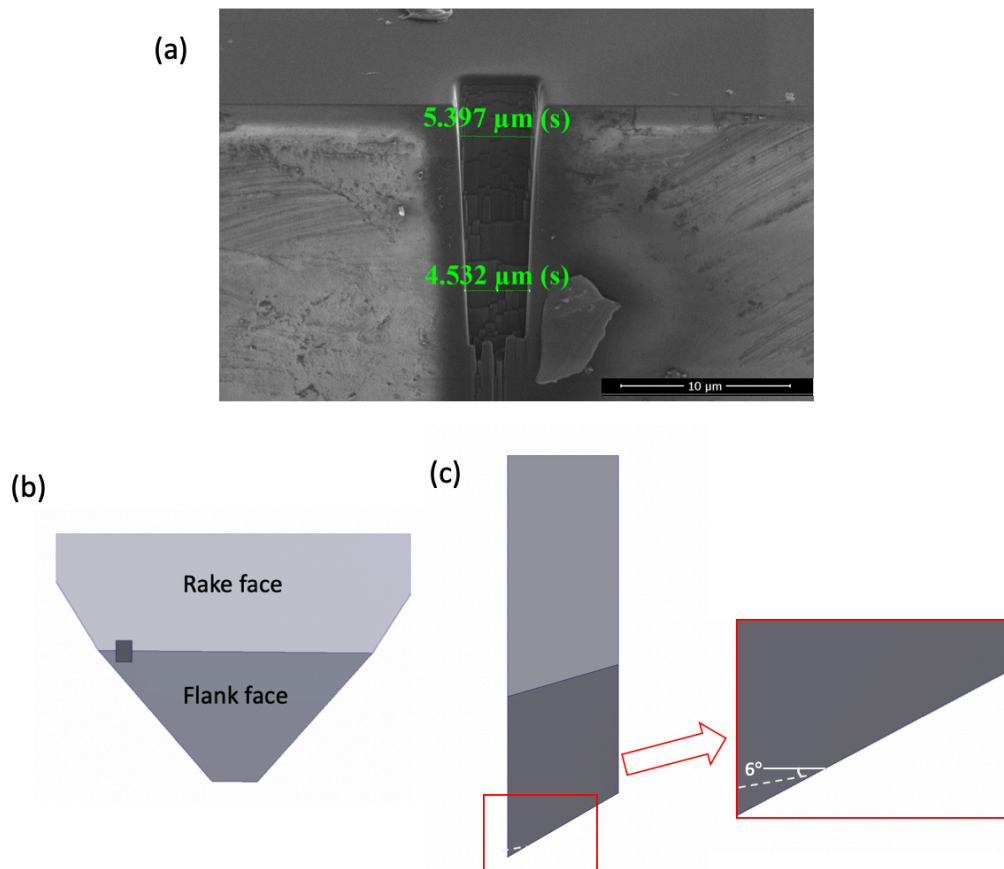


Figure 4. 2 (a)SEM images of diamond tool milling by FIB with multi-step (b) SEM perspective schematic view of the machined feature(c) Schematic side view of SCD tool. The microgrooves went through the whole tool tip and had an intersection angle of 6 degree.

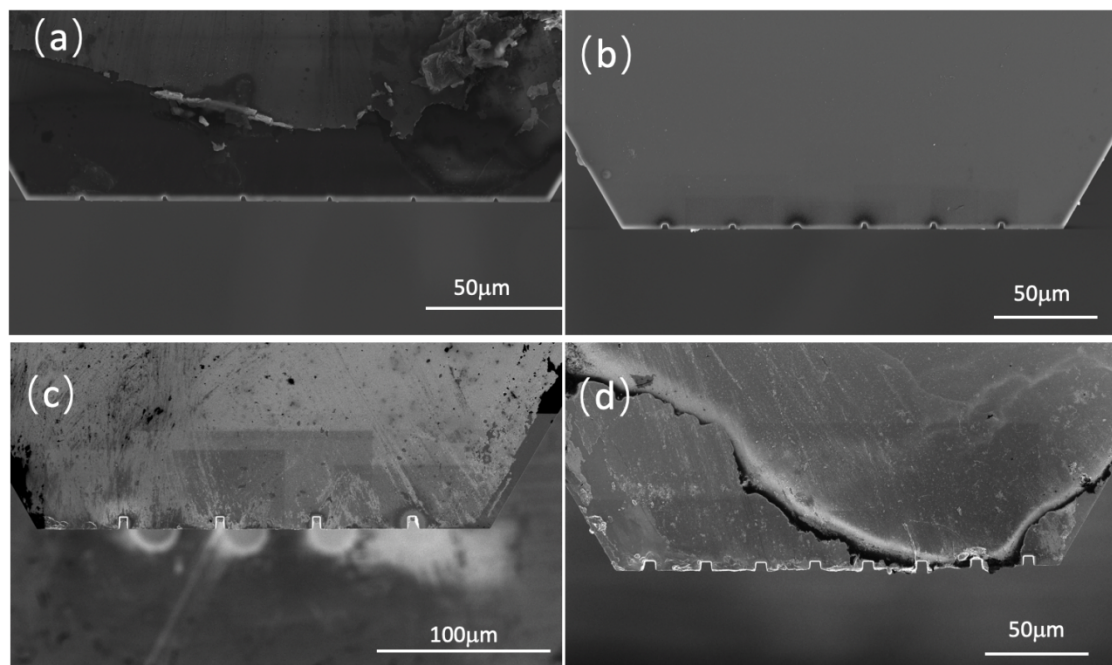


Figure 4.3 FIB images of four machined diamond tools (a) tool #1 with $1\mu\text{m}\times 1\mu\text{m}$ grooves and $30\mu\text{m}$ spacing, (b) tool #2 with $2\mu\text{m}\times 2\mu\text{m}$ grooves and $30\mu\text{m}$ spacing, (c) tool #3 with $5\mu\text{m}\times 8\mu\text{m}$ grooves and $50\mu\text{m}$ spacing, (d) tool #4 with $5\mu\text{m}\times 5\mu\text{m}$ grooves and $20\mu\text{m}$ spacing.

Diamond is non-conductive material which lead to accumulation of charges as the ion beam is directed at it. A portion of the ion beam causes sputtering of the workpiece material and is involved in material removal. Another significant amount gets embedded in the workpiece and produces the charging effect. This charging lead to the beam divergence and drift that can result in loss of resolution of the pattern created as well as drift in the path of the beam over the intended surface. In conventional FIB milling, which is mainly used on conductive workpieces or for machining very short depths, the intended shape is machined

top down. The raster scan of the ion beam goes over the entire feature to be machined and removes material layer by layer. When the conventional single step FIB machining is used on a non-conductive workpiece, the tool goes over the entire pattern to remove the first layer of material. This process removes the conductive coating and therefore any subsequent machining will produce charged surface. While in the multistep pattern milling process, when the ion beam goes deep in a localized region, the surrounding conducting surface can still prevent charging there and subsequent beam drift. Compared with the one-step milling, which is mainly used in FIB milling, there is less charge accumulation in each step and between each step. Milling deeper in one location while still maintaining the conductive surface in the surrounding location prevents beam deflection due to charging. In single step machining, the machining time was 20 min using 1nA. The machining time decreased in total by using different currents compared with single step machining leads to a more efficient removal.

Although multi-step FIB milling increased the accuracy and decreased beam divergence effect, the beam drifting was not completely eliminated, and several challenges were encountered in the machining of SCD tools. As can be seen in the SEM image (Figure 4.2a), the structure formed is wide at the top and narrow at the bottom instead of a uniform width of groove. The variation in the machined feature from the designed pattern was 9.4% in multi-step FIB milling in this case. This kind of a tunneling effect is typical in FIB milling over a considerable depth due to redeposition effect of the sputtered material. Using multi-

step milling method however provided a much cleaner side wall and smooth edges as compared with single step machining shown in Figure 4.4 which was important to cutting performance during subsequent CNC machining using these tools. Therefore, this method was adopted for all the machining of tool tips performed in this thesis.

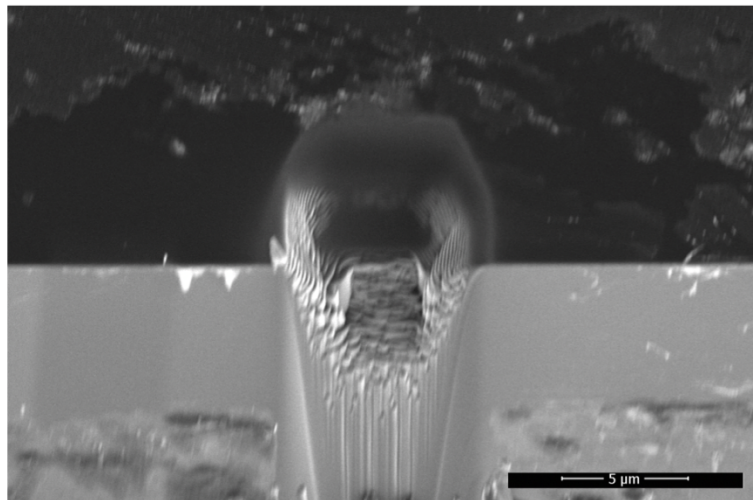


Figure 4. 4 Result of single step machining by FIB

Even with the improvement several small defects were noticed in the multistep FIB milled tools. For example, although the intended pattern to be machined had a sharp corner, the corners of the final machined feature turned out to be rounded as shown in Figure 4.5. This is due to the beam size as well as the gaussian distribution of intensity within the beam that was used in milling. During the scanning process, the beam followed the pattern to build designed structures, however the gaussian distribution in intensity led to partial removal in some regions beyond the machining boundary[82].

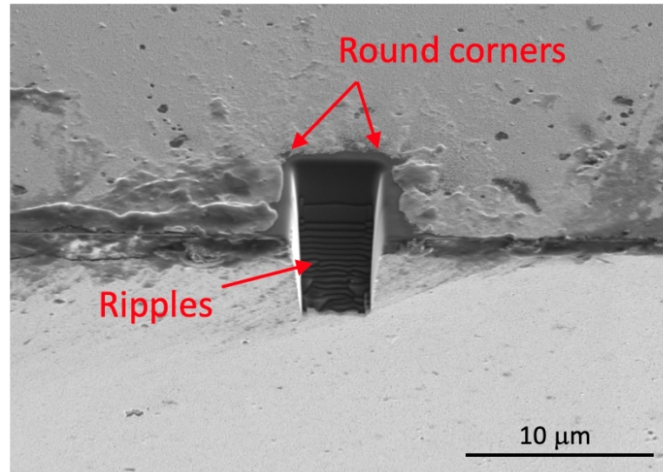


Figure 4. 5 FIB milling detects with ripples and round corners.

Another issue was the formation of ripples on the side walls of the machined surface as can be seen in Figure 4.5. Off-normal ion beam bombardment has been shown to form periodic height modulated structures like ripples [83]. The origin of ripple formation is due to the surface instability caused by the competition between curvature dependent sputtering and surface diffusion process. Bradley and Harper[83] demonstrated that an ideal ripple free surface can be obtained when the incidence angle of the beam to the workpiece was 90° . However, at other incident angles a collapsed edge at the end of structure, which is the cutting edge of SCD tool, can be formed. Ding et al.[73] found the relationship of ion beam incidence angle and surface roughness. It can be found that the roughness was low at small incidence angle until 30° . In this thesis, the incidence angle was set to 6° to the normal of the rake face, which was in the range of small roughness. They also found the rate of ripple

growth was faster and the ripples were more significant when ion currents were high (7nA and 20nA) as compared with smaller current (2.2nA) at the same incidence angle. In order to keep the high throughput of FIB milling and machining efficiency, mid-level of current (from 0.3nA to 5nA) was used to fabricate the structures. Although the ripples still formed on the further FIB milling surface, a relative fine and smooth cutting edge was achieved which was most important regarding to the use application of these SCD tools. During CNC machining, a small angle between the machined surface and the clearance surface helps the removal of cutting chips. So 6° incident angle was chosen instead of 0° .

Redeposition of the sputtered material is a common phenomenon with FIB machining of SCD tools especially with the micro-groove structure[73][79]. There was not much of redeposition here because the low aspect ratio and open-edge structures that were machined which allowed easier evacuation of the sputtered materials away from the tool tip. The third step of the multi-step milling method was used as a polishing process which also greatly helped to eliminate the redeposition layer.

4.2 One-directional CNC machining results

These microstructured SCD tools were used to CNC machine various materials to demonstrate that the topographical features on the tool can be replicated on the machined surface. Various cutting depth, cutting speed and cutting orientation were used to machine

two different materials, PMMA and Aluminum alloy 6061. Experiments were also conducted with three different cutting speed (300 mm/min, 1000 mm/min, 2000 mm/min) and three different cutting depth (2 μm , 4 μm , 8 μm) using tool #3 to machine PMMA in order to identify the effect of these parameters on the features produced.

The CNC machining using tool #1 which has microgrooves with dimensions of $1\mu\text{m}\times 1\mu\text{m}$ was found to not reliably replicate the tool microstructure on the workpiece. This was because the features were within the alignment accuracy of the machine. If the tool were not perfectly flat against the workpiece and the workpiece was not perfectly smooth, these features will not be reproduced in all the regions of the workpiece. Therefore, all the results thereafter were based on CNC machined samples by tool #2 with $2\mu\text{m}\times 2\mu\text{m}$ grooves and $30\mu\text{m}$ spacing between grooves, tool #3 with $5\mu\text{m}\times 8\mu\text{m}$ grooves and $50\mu\text{m}$ spacing, and tool #4 with $5\mu\text{m}\times 5\mu\text{m}$ grooves and $20\mu\text{m}$ spacing. The Fig 4.6 shows an example of machined Aluminum surface observed under SEM while Figure 4.7 shows the images of the PMMA machined surface that was used to measure the dimension of structures. All the CNC machining parameters have been used has been shown below in Table 4.1 where orientation machining will be discussed in next section.

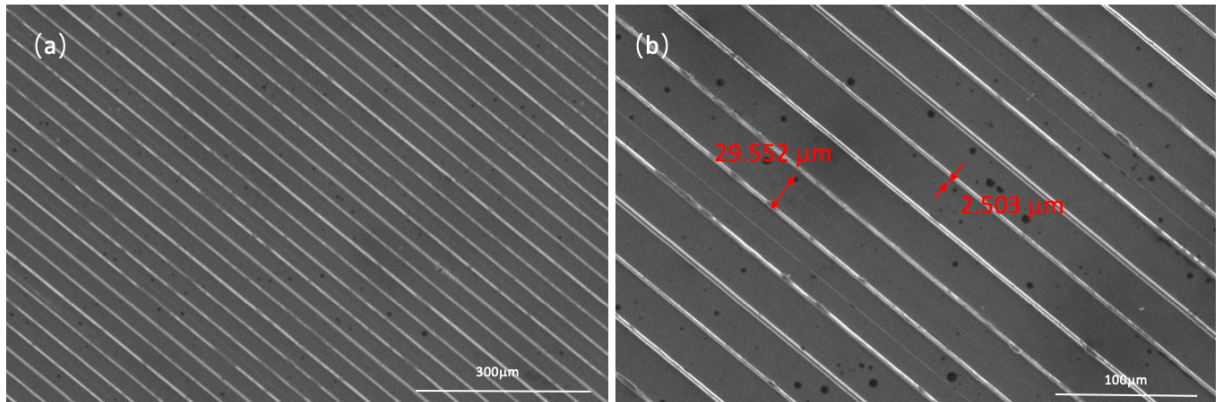


Figure 4. 6 SEM images of Aluminum machined by tool #2 at 300 mm/min cutting speed. (a) 200×magnification of Aluminum sample (b) 500× magnification of Aluminum sample

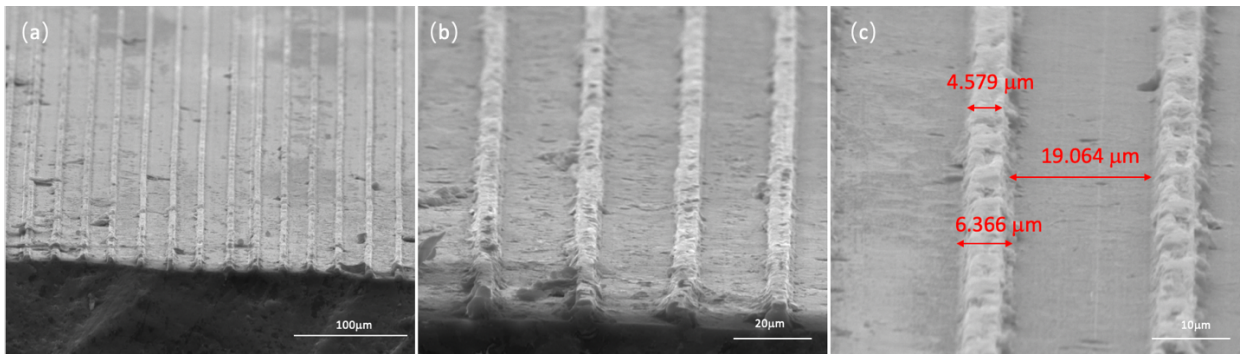


Figure 4. 7 PMMA samples machined by tool #4 at 1000 mm/min cutting speed. (a) 600× magnification (b) 2000× magnification (c) 4000× magnification

Table 4. 1 Machining parameters details of different conditions

Material	Speed(mm/min)	Depth(μm)	Orientation ($^{\circ}$)
PMMA	300	2	90
	1000	4	60
	2000	8	45
Aluminum	300	2	/
	1000	4	/
	2000	8	/

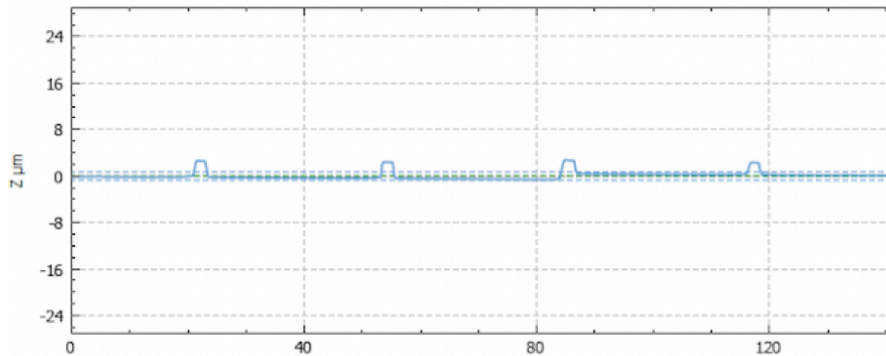


Figure 4. 8 The partial height scanning results under confocal microscope of PMMA sample cut by tool #2 at 300 mm/min

Confocal microscope was used to observe the uniformity and continuity of microfeatures formed after CNC machining as shown in Figure 4.8. The size of micro-ridges formed by CNC machining were $2.7\mu\text{m} \times 3.0\mu\text{m}$ after. The difference between the size of micro-ridges and size of micro-groove on the tooltip of this PMMA sample was 24.1% where the

dimension of tool was $3.2\mu\text{m} \times 3.0\mu\text{m}$. Similar measurements were performed for all of the microfeatures formed by CNC machining and the results are presented in Figure 4.9. They show that the smallest features have the greatest difference and it reduces with large feature sizes.

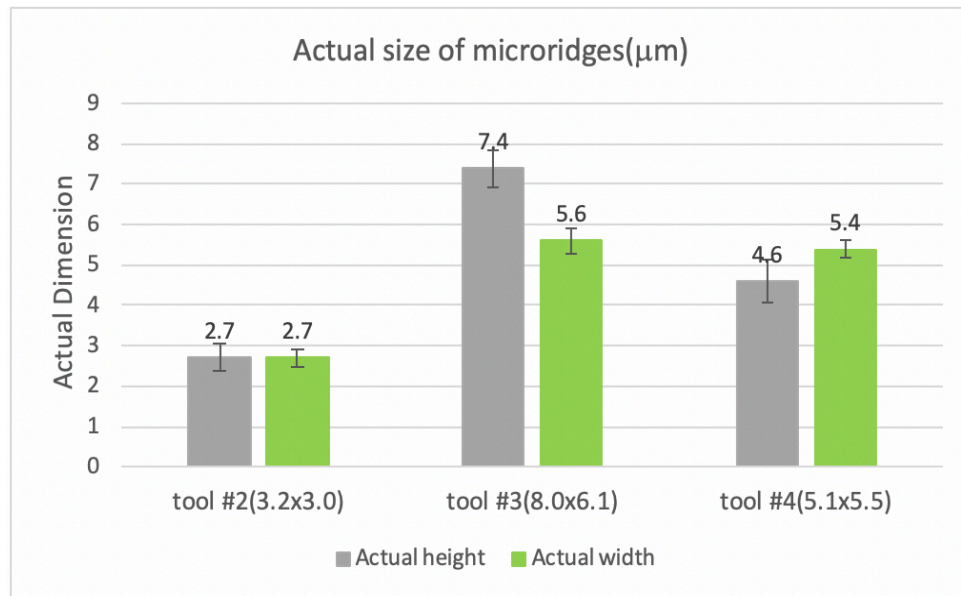


Figure 4. 9 Dimensional variation between cross-section area of micro-ridges on PMMA samples and micro-grooves on tooltips, including the actual size of tool #2 to #4 in x-axis.

The surface roughness (R_a) was analyzed by Alicona microscope with $10\times$ magnification scanned to quantify the surface quality after CNC machining. R_a was measured at the region between ridges in order to neglect the influence of micro-structure's size on its measurement. The 6061 Aluminum surface machined by tool #2 at 300 mm/min has the R_a

of $0.337\mu\text{m} \pm 0.016\mu\text{m}$. In comparison the roughness of 6061 Aluminum surfaces machined by tool #3 at 300 mm/min and 2000mm/min was found to be $0.457\mu\text{m} \pm 0.043\mu\text{m}$, $0.271\mu\text{m} \pm 0.011\mu\text{m}$ respectively. Similarly, R_a of PMMA machined samples was found to be 0.439 ± 0.135 at 300mm/min, 0.298 ± 0.065 at 1000mm/min.

Contact angle measurement shows the change of wetting ability of surfaces after CNC machining with micro-structures which is ultimate goal for the microtexturing of the surface. A $2\mu\text{L}$ water droplet was deposited on the surface and the contact angle from various directions measured. The images were analyzed and fitted using the Young-Laplace method. The contact angle of original PMMA and 6061 Al alloy surfaces before machining was found to be $84.5^\circ \pm 2.6^\circ$ and $89.3^\circ \pm 1.4^\circ$ respectively. The top view of a droplet deposited on the PMMA surface can be seen in figure 4.9 which showed an elongated shape aligned to the micro-ridges that were machined. The droplet had different contact angles in different directions on its surface. The contact angles were found to be 108.9° (Figure 4.10a) along the ridges (parallel angle) and 155.7° (Figure 4.10b) across the ridges (vertical angle). In the case of 6061 Al sample, the contact angle was 108.1° (Figure 4.10c) along the ridges and 163.1° (Figure 4.10d) across it. The difference between two directions ($\Delta\theta$) which is defined as anisotropic contact angle was as high as 71.6° . The sliding angles were also found to be different in the two directions which was $43.6^\circ \pm 0.9^\circ$ and more than 90° (the

droplet did not slide due to pinning) respectively. The PMMA surface after CNC machining had very good transparency which can be seen in Figure 4.11.

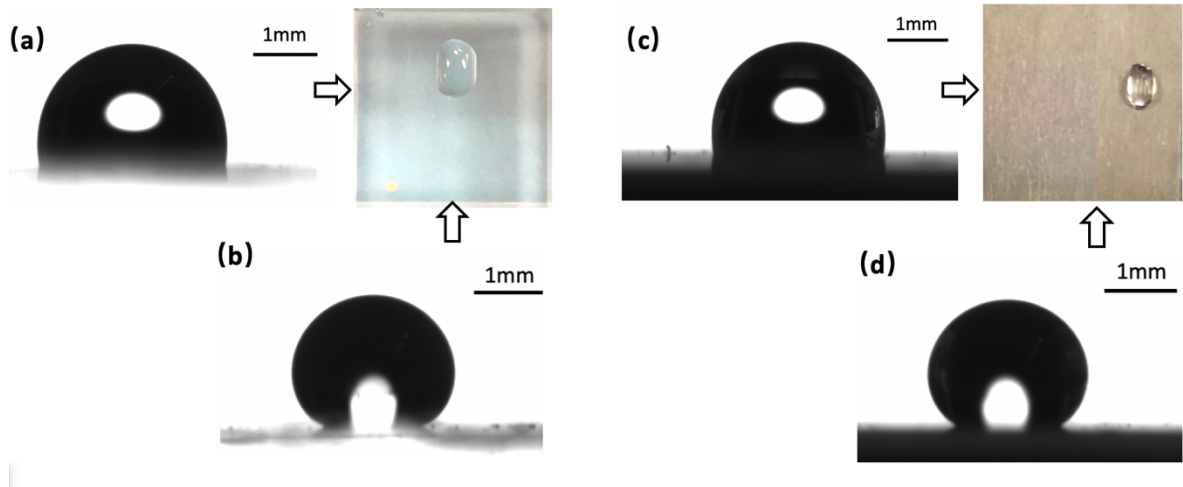


Figure 4. 10 Sessile droplets on PMMA sample and 6061 Al sample. (a) PMMA surface parallel contact angle of 108.9° in along-feature direction(b) PMMA surface vertical contact angle of 155.7° from across-feature direction(c) 6061 Al sample parallel contact angle of 108.1° from along-feature direction. (d) 6061 Al sample vertical contact angle of 163.1° from across-feature direction.

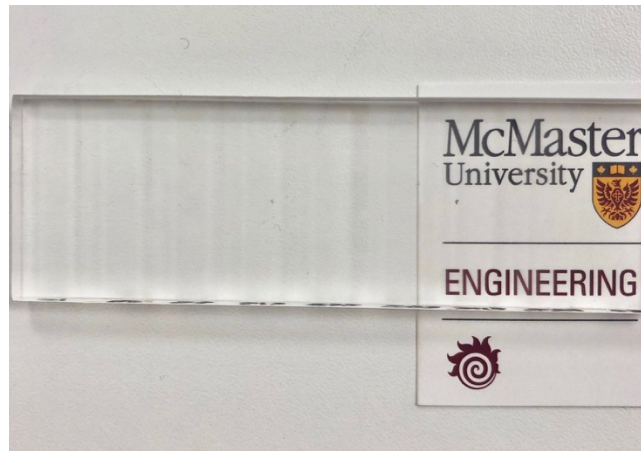


Figure 4. 11 Printed text observed through PMMA surface after CNC machining by tool#2 as an illustration of its transparency and clarity. The surface was machined with tool#2 which had $2\mu\text{m}\times 2\mu\text{m}$ structures with three different cutting speeds: 300mm/min, 1000mm/min and 2000mm/min.

The results presented so far demonstrate that microfeatures can be successfully transferred from the machine tool onto the workpiece in both metallic and polymeric materials (Fig 4.6, 4.7). The sizes of the features replicated depends on the minimum feature size of the grooves formed on the machine tool as the tool cuts through the workpiece. Since the FIB machined groove was tapered the narrower opening at its bottom determined the features produced.

There was significant surface roughness on the features machined into the workpiece as can be seen in Fig 4.7. This could be a result of ripples that were present on the side walls of the microfeatures that were machined into the tool tip. Similar to Tong et al.[84], small burrs or structural damage on micro-structures were observed which were much larger than

those from photolithography or other such processes. However, these irregularities were much smaller than laser machining processes. Furthermore, the alignment accuracy of the both of the tool to the workpiece was important in reproducing all the features on the tool accurately on the workpiece.

The material removal rate (MRR) can be used to compare the throughput of this process with the conventional FIB machining of the entire workpiece in a direct write fashion. The MRR for CNC machining is

$$\text{MRR} = S_{sc} v_c \quad \text{Eq.4.1}$$

Where S_{sc} is the cross-section of removed area during CNC machining and v_c is the cutting speed. The MRR of tool #3 at 1000 mm/min cutting speed with 8 μm cutting depth is $9.2 \times 10^7 \mu\text{m}^3/\text{s}$ which is 1.5×10^8 times faster than conventional FIB milling with ion current of 1 nA [79]. Compared with laser cutting a high repetition rate of 200 kHz fs laser system with 10 μJ pulse energy, the MRR is 11 times faster than optimized laser cutting [85]. The CNC machining method shortened the entire process by increasing the machining throughput and eliminating the need for post-treatment time unlike laser machining (LBM). The throughput is significantly improved by CNC machining as the FIB milled SCD tool creates the microridges in parallel and the speed of the machining process is similar to conventional CNC machining. LBM methods are direct write with a single laser beam and the pulse width combined with the scanner speed does not ensure enough flux to ablate the

material when the speed is too high. Therefore, they take significantly more time. An important limitation of the LBM process is the redeposition and formation of burrs on the sides of the machined feature. These are significant when continuous wave lasers or even nanosecond pulse laser are used. They can be avoided using femtosecond lasers albeit at the loss of throughput and material removal rate. The form accuracy obtained with CNC method is shown in Figure 4.9. Significant variations between the features machined and the corresponding features on the tool were observed when tools with small grooves (tool #2 with $2\mu\text{m}\times 2\mu\text{m}$ features) were used. However, the form accuracy improved with larger features and tool #3 has the smallest variation. Based on these results, the width of $5\mu\text{m}$ which is the widest dimension is the best feature used to machine micro-structures in this case. From the roughness results, higher cutting speed was found to reduce the surface roughness as expected.

The shape of the droplet resting on a textured surface can be significantly influenced by the pinning locations on the surface. Huh et al. [86] examined droplet shapes with surface with sharp ridge type protrusions and found the shape on the surface induced pronounced droplet distortion. With closely micro-ridges, the boundary of droplet was pinned by the adjacent structures which prevented the spreading out of the deposited droplet and confined it to a particular shape defined by the ridges. Gibbs has previously demonstrated that liquid confinement and contact line pinning can be realized by sharp edges and height steps [87]. Cubaud et al. [88] demonstrated deformation of droplet when deposited on hexagonal array

of ridges on a hydrophobic surface as shown in Figure 4.12. Droplet deformation along the ridges on the surface is significant and surface showed strong anisotropic wetting with a high anisotropic contact angle ($\Delta\theta$). The microridges that were created on PMMA and aluminum in this thesis also demonstrated contact line pinning in a manner similar to the previous works. The ridges can be considered as the physical barrier to the contact line movement during the wetting process. The droplet contact line becomes trapped when the barrier was high and was pinned by these periodical micro-ridge structures lead to anisotropic wetting. The contact angle results demonstrated the surface was hydrophobic from all directions and highly hydrophobic from across-feature direction. The sliding angles difference between different directions was $>41.4^\circ$ which was significant. It showed that the microstructures have anisotropic property in both static and dynamic wetting. Although the contact angle of across-feature direction was close to superhydrophobicity, the slide angle achieved was much larger as compared to what is required for a superhydrophobic surface (ideally lower than 10°).

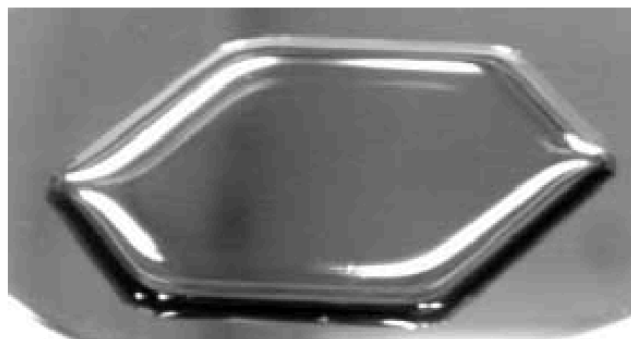


Figure 4. 12 Droplet distortion with 6 cm diameter based on hexagonal array[88]

Based on the CNC machining results, the microstructures can be successfully fabricated on the PMMA and 6061 Aluminum Alloy surface using FIB-milling SCD tools by CNC machining. The microstructures showed relatively good uniformity and continuity. The throughput of creating micro-level features is much higher than direct FIB milling. Meanwhile, the wetting property of machined surface was changed which turned to a significant anisotropic wetting surface in both static and dynamic wettability. A new method to create anisotropic wetting surface was developed which generate microstructures on both metal and non-metallic materials fabricated with CNC machining by FIB-built SCD tool with multi-tool tips.

4.3 Effect of CNC machining parameters on anisotropic wetting

The influence of CNC machining parameters on the microstructures produced on the work piece and consequently surface wetting properties was also studied. In these experiments, Tool #3 was used to perform the CNC machining on PMMA workpiece while tool #3 and #4 were used on 6061 Al. The results were summarized and discussed in this section.

4.3.1 Effect of different cutting depths on anisotropic wetting

The effect of varying the cutting depth on the height of the ridges produced and consequently on the wetting characteristics was tested using tool #3 on PMMA at 300 mm/min with 2 μm , 4 μm , 8 μm cutting depth. Machining time was 16 minutes, 40 minutes and 80 minutes respectively. Three different workpieces were machined using these conditions at the various cutting depth studied. The machined workpiece surfaces were measured using the confocal microscope and multiple points of measurements were taken for each of the sample. They are aggregated across all the three workpieces and reported in Figure 4.13.

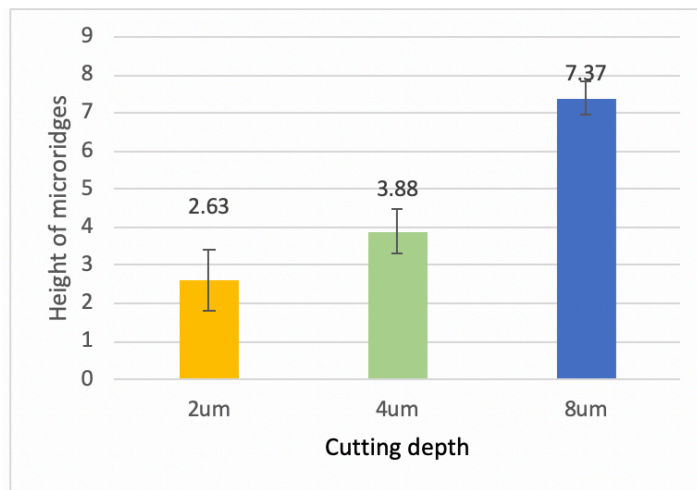


Figure 4. 13 Height of the micro-ridges obtained with tool #3 machining with various depth of cut and at speed of 300mm/min on PMMA workpiece (n=3).

The standard deviation of cutting depth of 4 μm was 0.57 μm and 8 μm was 0.44 μm which is more precise compared with 2 μm cutting depth with 0.80 μm standard deviation. This difference can be mainly attributed to the alignment accuracy of the machine and the tool alignment with the workpiece. Control of these parameters was more difficult when a smaller cutting depth was used with the microfeatures on the tool having a height of 8 μm .

After CNC machining, contact angle was measured using a 2 μL water droplet deposited on this surface at room temperature. The contact angles measurement results of 2 μm , 4 μm , 8 μm cutting depth on PMMA surface are shown in Figure 4.14. Five measurements of each sample were taken in each direction. The anisotropic contact angle ($\Delta\theta$) was shown in Figure 4.15 calculated based on contact angle measurement results.

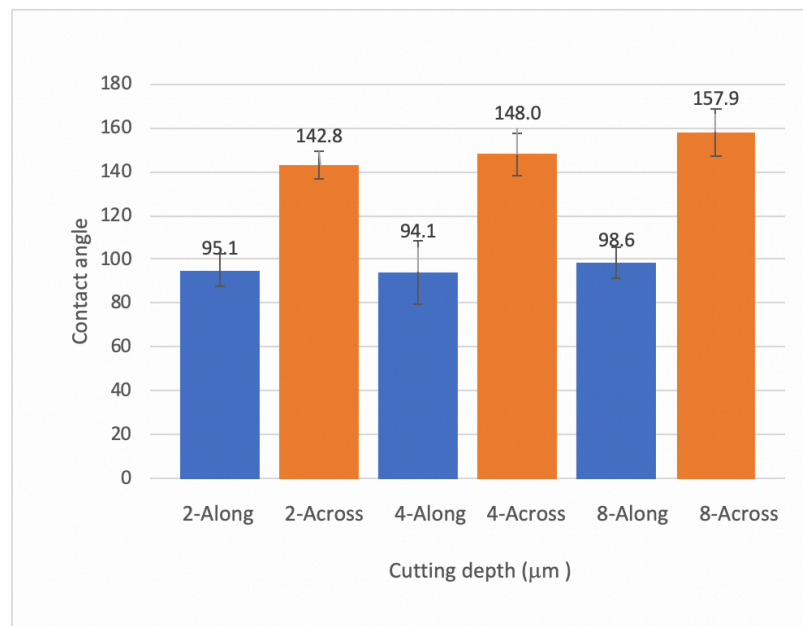


Figure 4. 14 Contact angle results with different three cutting depth: 2 μm , 4 μm , 8 μm on PMMA samples.

Along label indicates the contact angle along the ridges while across label represents direction perpendicular to the ridges. Five measurements were taken of each sample in each direction.

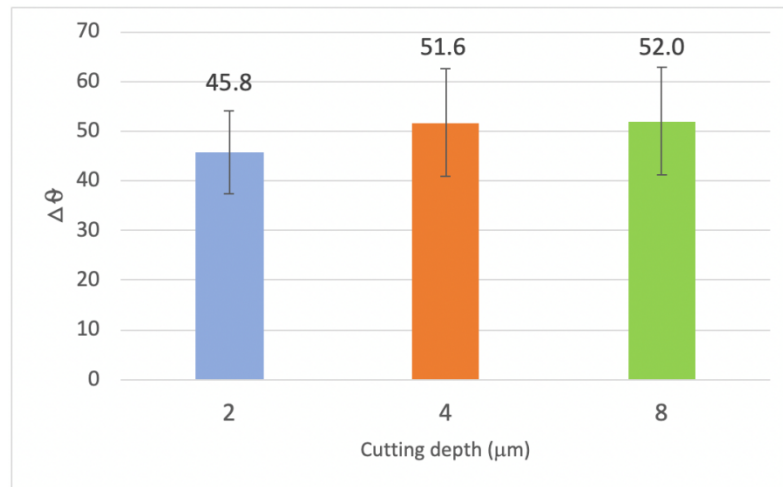


Figure 4. 15 Anisotropic contact angle ($\Delta\theta$) results of samples based on three cutting depth: 2 μm , 4 μm , 8 μm .

It can be seen that the contact angles and the anisotropy ($\Delta\theta$) was not changed significantly with different cutting depth. This result is similar to previous observations made by Bliznyuk et al. [89] who conducted an experimental study of the relationship between the ratio of groove height and spacing and its effect on the contact angle. They found that (Figure 4.16) as the ratio of height to spacing decreased the droplet transition from a Cassie state to a Wenzel state. They also identify a critical contact angle based on the height to

spacing ratio which determines which state the droplet will prefer. The critical contact angle was calculated to be[89]

$$\cos\theta_{CR} = \frac{-1}{1 + \frac{2h}{b}} \quad \text{Eq.4.2}$$

Where $\cos\theta_{CR}$ is the critical angle which is used to estimate the droplet state, h is the height of microstructures and b is the spacing.

When the critical angle is larger than the contact angle of the workpiece material which is PMMA or Aluminum 6061 in this thesis, Wenzel state is more favorable. The critical angles based on 2 μ m, 4 μ m and 8 μ m height and 30 μ m spacing are 151°, 142° and 130° that are much larger than the contact angle of original material surface. Therefore, the Wenzel state fits the model in all these different depths.

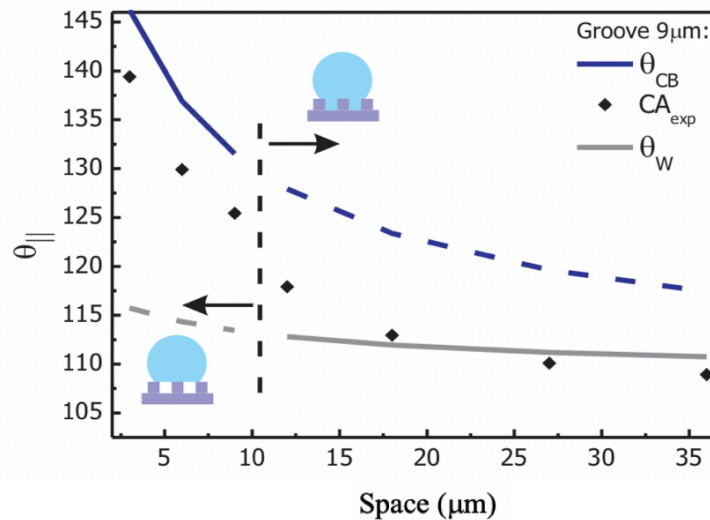


Figure 4. 16 Contact angle versus spacing [89]

It can be seen from Fig 4.16 that the contact angles don't change much in the Wenzel state. In Wenzel state, the droplet wets fully on the solid surface, although the structure changed there was no air trapped between liquid and solid to influence the behavior of droplet which lead to a larger contact angle. The contact angle is mainly depended on the pinning position of anisotropic wetting which is related to the spacing of microstructures. The ratios of the height to spacing obtained on both PMMA and Aluminum produce a critical contact angle larger than 130° which are above the contact angle of the native material and therefore place them in the Wenzel state. Therefore, the aspect ratio of the structures is not expected to have much of an impact on the contact angle.

4.3.2 Effect of different cutting speeds on anisotropic wetting

In order to investigate whether the cutting speed will have an effect on the microridges produced and on the contact angles obtained, experiments with three different cutting speeds (300mm/min, 1000mm/min, 2000mm/min) were conducted. Tool #3 was used to machine PMMA workpieces at all the three speeds with a cutting depth of 8 μ m while two different cutting speeds (300mm/min, 2000mm/min) were used on 6061 Aluminum. Contact angles obtained from the microstructured workpiece for the various cutting speed samples are plotted in Figure 4.17 for PMMA and Figure 4.18 for 6061 Aluminum samples. Anisotropic contact angles ($\Delta\theta$) of PMMA and 6061 Aluminum samples are shown in Figure 4.19.

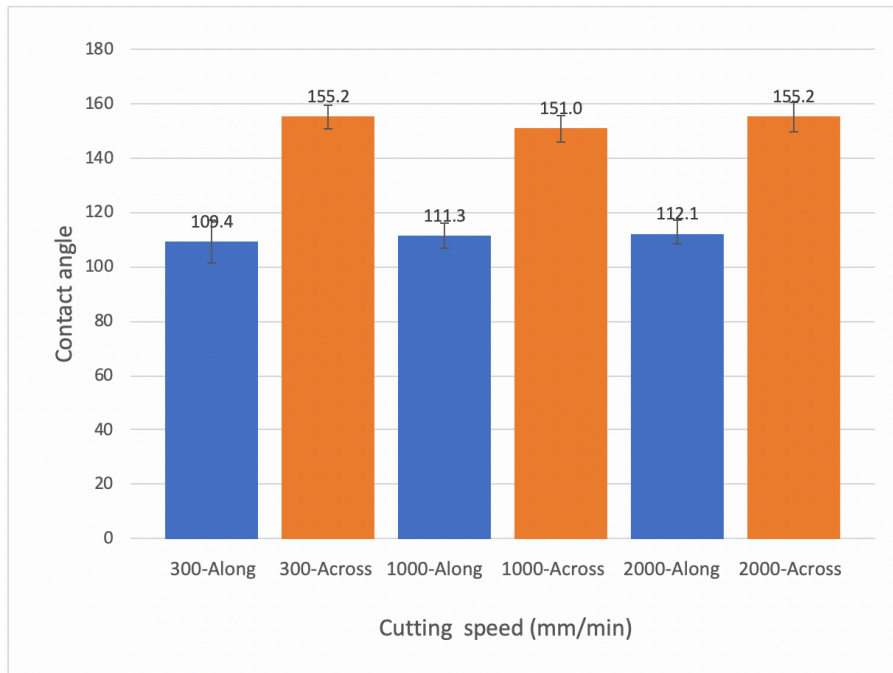


Figure 4. 17 Contact angle with three different cutting speeds on PMMA samples. Along label represents the contact angle in direction along the ridges and across represents the contact angles in the direction perpendicular to the ridges.

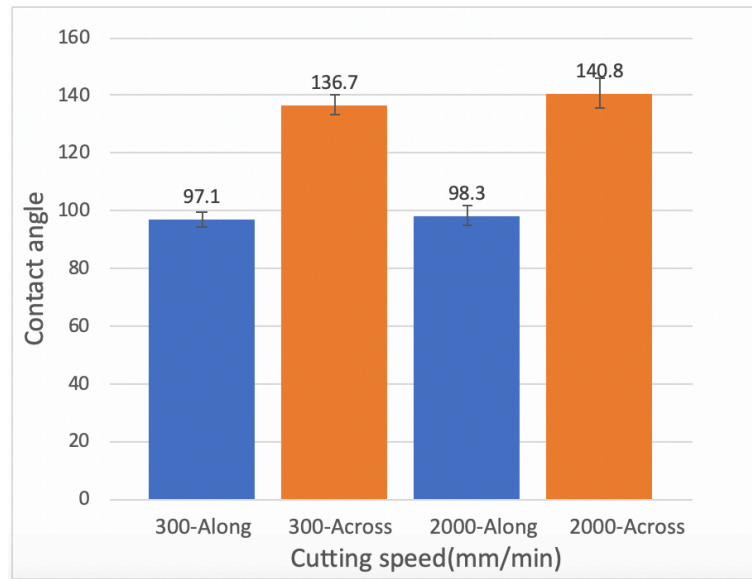


Figure 4. 18 Contact angle with different cutting depth on Aluminum samples. Along angles are the contact angle in along features direction and across contact angles are in across features direction.

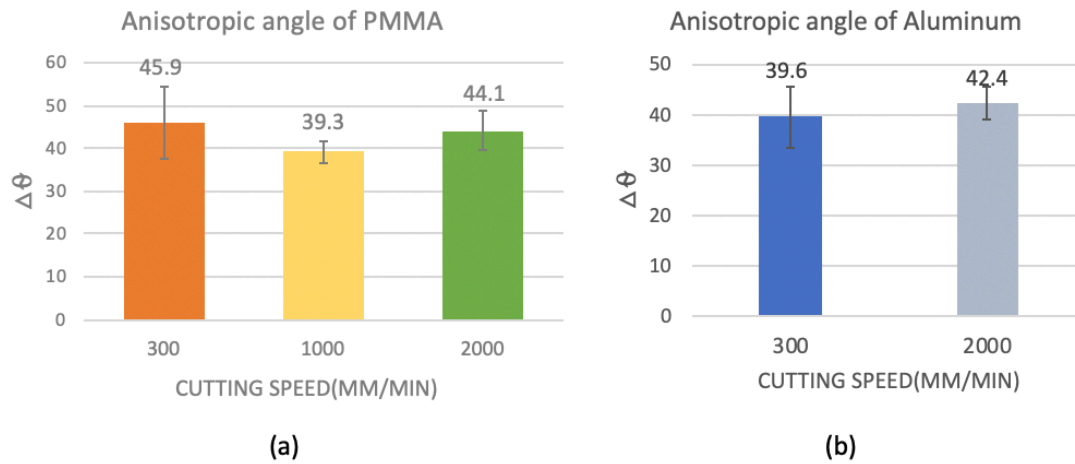


Figure 4. 19 Anisotropic contact angle ($\Delta\theta$) results of samples with different cutting speeds. (a) $\Delta\theta$ of PMMA samples with three different cutting speeds: 300mm/min, 1000mm/min, 2000mm/min (b) $\Delta\theta$ of 6061 Aluminum samples with two cutting speeds: 300mm/min, 2000mm/min.

The results of contact angles stay stable even when the cutting speed was changed from 300mm/min to 2000mm/min on both the PMMA and aluminum samples which indicates that the wetting property of samples is not changed by cutting speed. Although the roughness of surface between the ridges changes due to the changing of cutting speed, these are not consequential as pinning of the droplet is the main mechanism for determination of the contact angle. From the perspective of anisotropic wetting, the pinning position of different cutting depths were same with each other because the same dimension of micro-ridges was built on the samples. With same pinning effect, degree of droplet deformation was not changed which related to similar contact angle results. The micro-structures built on the surface have suitable wetting property for different machine speed conditions which is good for scale-up machining with large area with higher cutting speed to improve the efficiency and throughput.

4.3.3 Effect of materials on the anisotropic wetting

The effect of the workpiece material itself and its inherent contact angle on the anisotropic wetting can be determined by comparing the data from previous experiments which were obtained under the same experimental conditions. The contact angles obtained using tool

#3 at 300mm/min cutting speed with $8\mu\text{m}$ cutting depth for Aluminum and PMMA were compared and plotted in Figure 4.20. Anisotropic contact angles ($\Delta\theta$) of PMMA was $45.9^\circ \pm 8.5^\circ$ and that of 6061 Aluminum samples was $39.6^\circ \pm 6.0^\circ$.

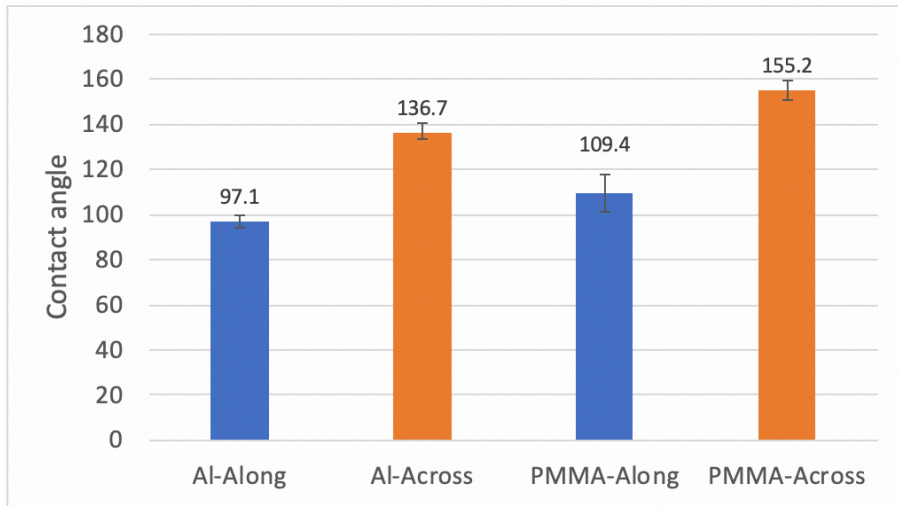


Figure 4. 20 Contact angle measurement results of 6061 Aluminum alloy and PMMA sample at same machining parameters at 300mm/min cutting speed with $8\mu\text{m}$ cutting depth. Along angles are the contact angle in along features direction and across contact angles are in across features direction.

Both along and across contact angles of PMMA were larger than 6061 Aluminum which was expected as PMMA is inherently more hydrophobic than 6061 Aluminum. From the anisotropic wettability perspective, $\Delta\theta$ of PMMA and 6061 Aluminum do not have a significant difference between each other which indicates that the pinning ridges provide similar anisotropic properties for wetting irrespective of the material on which they are machined within the narrow range of contact angles among the materials tested. Based on

the pinning theory, surfaces with the same micro-structures has the same energy barrier and pinning position to elongate the droplet. This is the main reason that two different materials have same anisotropic wettability. Another reason is the surface wetting property before machining of PMMA and 6061 Al are similar, that contact angle of original PMMA, and 6061 Al surfaces were both hydrophilic. Therefore, with the similar material wetting property and same micro-structures, same level of anisotropic wetting is obtained from PMMA and 6061 Al samples. It is interesting that many of the machining parameters such as depth of cut, speed of machining have minimal effect on the wettability. This ensures that the wettability is solely determined by the design of the microridge features and its characteristics as opposed to machining parameters enabling high throughput machining processes to be used.

4.3.3 Effect of spacing on the anisotropic wetting

In order to understand the influence of micro-ridge spacing to the contact angle, workpieces were machined with tool #3 and #4 that had 50 μ m and 20 μ m spacing between their grooves built into tool tips with 8 μ m and 5 μ m cutting depth. Although the cutting depth was different, it is not an influencing factor on the contact angle based on the previous results of cutting depth variation. They were machined at 1000 mm/min cutting speed on 6061 Al. Contact angles obtained from 6061 Al workpieces machined with these two spacings are

shown in Figure 4.21. The Anisotropic contact angle $\Delta\theta$ was $40.4^\circ \pm 4.7^\circ$ for $50\mu\text{m}$ spacing and $71.6^\circ \pm 6.8^\circ$ for $20\mu\text{m}$ spacing.

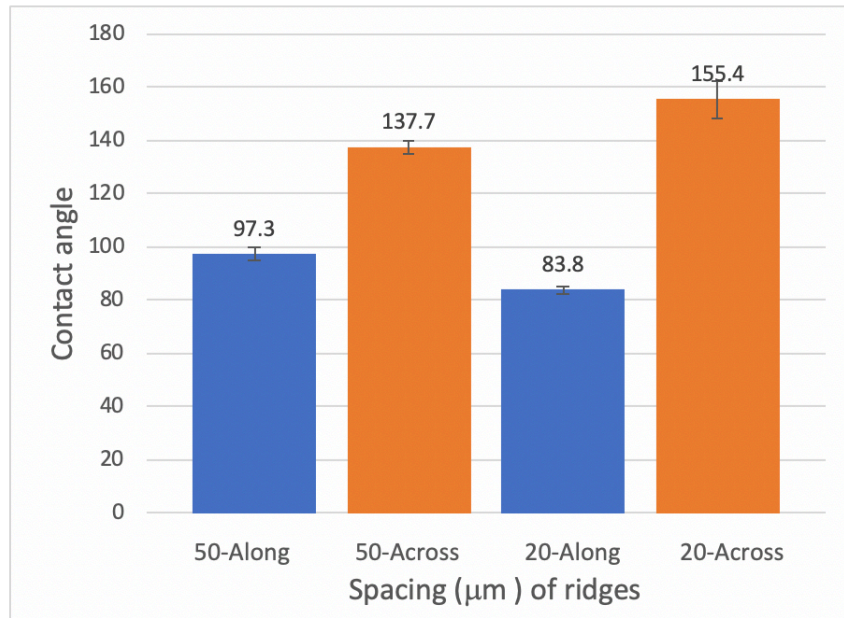


Figure 4. 21 Contact angle with different spacing between ridges built on the surface which is $50\mu\text{m}$ and $20\mu\text{m}$ of microstructure spacing of SCD cutting tool on Aluminum samples. Along angles are the contact angle in along features direction and across contact angles are in across features direction.

The contact angle difference between the directions across and along the ridges ($\Delta\theta$) is a measure of the anisotropy introduced by the structure. It can be seen that the closer spacing of ridges increases the difference in contact angles between these directions. Since the material is the same its inherent wettability should be similar. The effect of spacing has been studied before [89] and it has been shown that even in the Wenzel state the spacing

has a small effect on the contact angle obtained (Fig 4.16). The results obtained here follow a similar pattern. As the spacing becomes smaller the same volume is confined (pinned) to a smaller nominal cross-sectional area. This pinning causes an increase in the contact angle in the direction across the ridges. Also, ridges with closer spacing has many more wicking corners (where the ridges are connected to the workpiece) that water can wick more easily. Therefore, the contact angle along the ridges is lower for the spacing that is closer as compared to the one spaced apart. Both of these factors account for a larger difference in the anisotropy in contact angle seen between the two direction. In conclusion, the anisotropic property is stronger when the spacing between microstructures is smaller.

4.4 Two-directional CNC machining results

The structures that can be created on the work piece are not restricted to simple line patterns. Depending on the tool path various other features can also be created. In order to demonstrate the versatility of this method, CNC machining in two different cross cutting directions was performed on PMMA samples in order to create micropillar array structures. Multi-directional machining was conducted on PMMA surface by using the microstructured tool to first cut in one direction and then rotating the workpiece by 90°, 60° and 45° such that another cut in an intersecting direction. If the depth of cut for both the machining process were the same, then the initial ridge features are expected to be reduced

to free standing pillars. If the depth of cut is different, then ridges with periodic pillar structures can be created. In the present experiment a $6\mu\text{m}$ cutting depth was used in both directions to machine a PMMA workpiece using tool #3 at 1000 mm/min. The schematic from top view of two-step directional machining process is shown below in Figure 4.

22. After two-directional CNC machining, contact angle was measured.

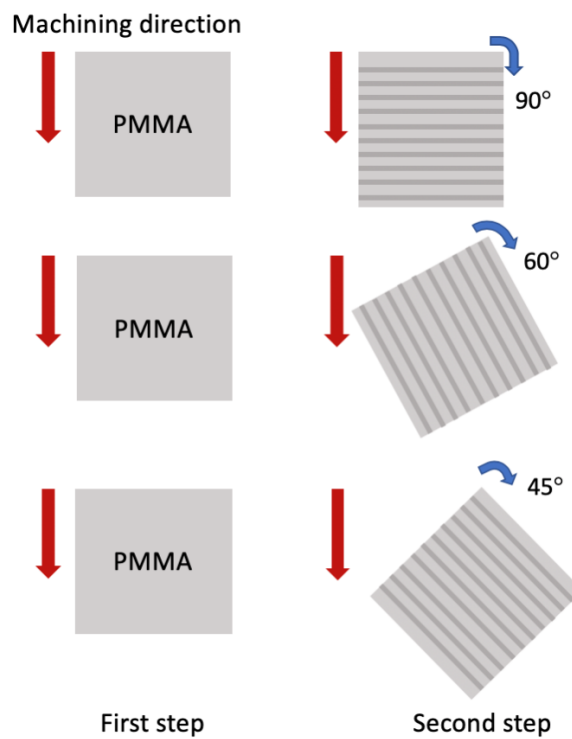


Figure 4. 22 Schematic of two-step directional machining process

SEM images in perspective view of topography of the surfaces obtained are shown in Figure 4.23. These results demonstrate that indeed micropillar patterns are produced and

the dimension of the micropillar was found to be $(4.83 \mu\text{m} \pm 1.32\mu\text{m}) \times (4.64 \mu\text{m} \pm 0.88\mu\text{m})$ which is similar to the feature size of the microgrooves in the tool. It can be seen that all of the patterns produced do include a small ridge pattern along with the micropillar pattern. This is probably due to misalignment when the sample was rotated for the second cut as any error in the z-offset can introduce a different depth of cut. Finally, the ridges and the micropillars produced were taller in one end as compared with the other end due to the tilt of the tool tip with respect to the workpiece.

Contact angle measurements were taken on these machined surfaces and the results are shown below in Table.4.2. An optical image of the top view of a droplet deposited on machined surface with 45° between two cutting directions is illustrated in Figure 4.24. It shows that the anisotropy associated with the one directional cutting is lost as expected.

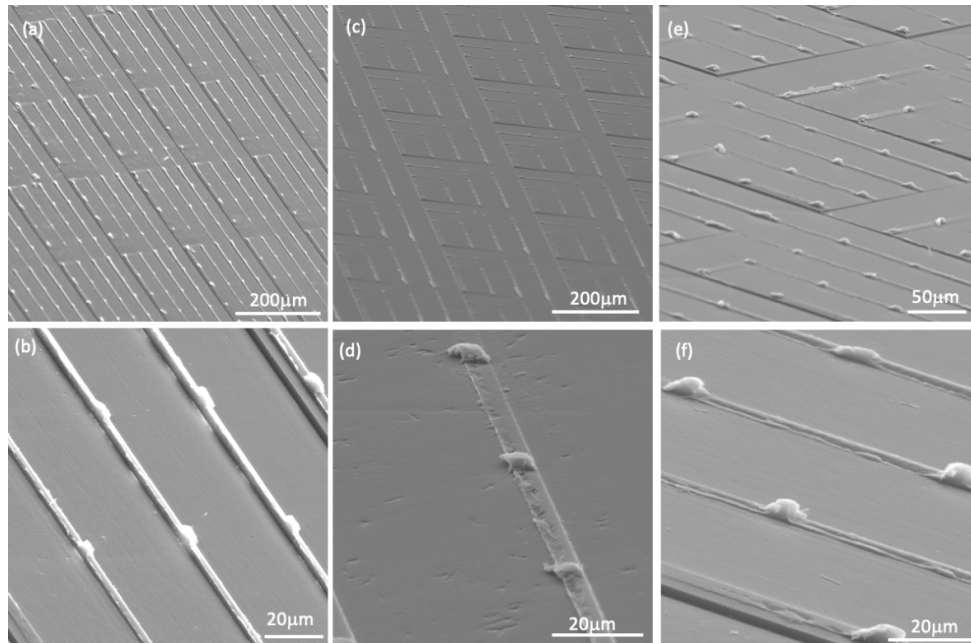


Figure 4. 23 SEM images of micro-pillar structures with different rotation angles. (a) 90° rotation angle under 300× magnification (b) 90° rotation angle under 2000× magnification (c) 45° rotation angle under 300× magnification (d) 45° rotation angle under 3000× magnification (e) 60° rotation angle under 800× magnification (f) 60° rotation angle under 3000× magnification.

Table 4. 2 Contact angle of two-directional machined samples

	Horizontal direction*	Vertical direction
90 degree	79.1° ± 4.2°	83.2° ± 3.3°
45 degree	71.2° ± 7.4°	81.2° ± 4.4°
60 degree	70.2° ± 2.2°	76.0° ± 5.0°

*Horizontal direction is the first cut direction

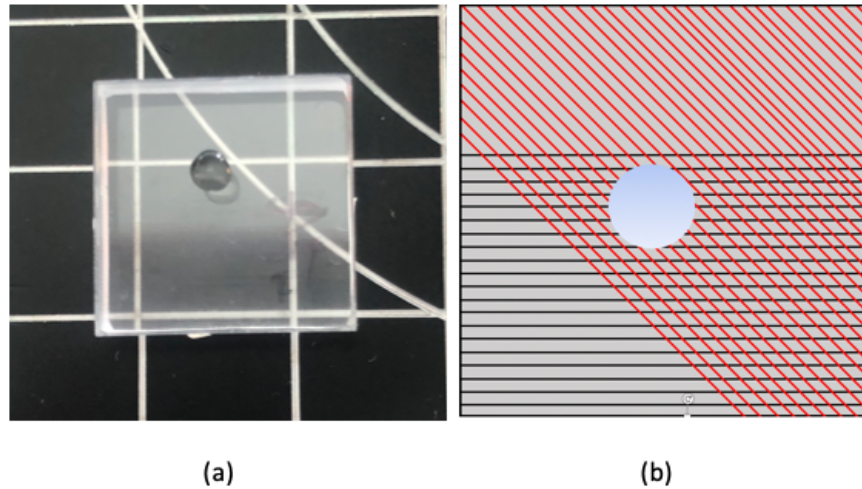


Figure 4. 24 (a) Sessile water droplet on two-directional machining surface with 45 degree intersection angle (b) Schematic of droplet stated on the two-directional machining surface with 45 degree intersection angle

Such micropillar arrays have been previously created using a single point diamond tool turning[73]. Nevertheless, the use of structured tool tip parallelizes the process and achieves a much higher throughput. Besides, the use of structured tool tip can be used to decrease the distance between the ridges quite easily as compared with other forms of CNC machining.

From the outline of droplet in Figure 4.24, one can see that even though the anisotropy in contact angle is lost, the droplet is clearly pinned at several locations and is not completely circular. This is due to the pillars forming pinning locations and holding the contact line.

Since the pillars are isotopically distributed in both the orthogonal direction, the anisotropy is lost.

4.5 Summary

In this chapter, proof of concept, effect of CNC machining parameters and materials and two-directional machining were discussed. By CNC machining, microstructures were successfully created on the PMMA and 6061 Aluminum samples with SCD tools microstructured by FIB. Compared with conventional method, machining microstructures in parallel using these structured tools improved throughput significantly. The anisotropic property of the samples with one-directional CNC machining by FIB built SCD tool is significant which is primarily dependent on the structure as compared with the cutting process parameters (cutting depth, cutting speed and material). The spacing between the ridges was the only parameter that was found to influence the wetting ability of machined surface. Anisotropy of the contact angle in different directions is increased when the spacing is reduced. Two-directional cutting with different angles were also investigated and it was found to produce relatively isotropic hydrophilic surfaces after machining. Overall, a new method that combined conventional CNC machining with emerging FIB micro-milling to create surfaces with anisotropic hydrophobic surface has been developed. By cross cutting in two directions with different intersection angles, two level of microstructures with pillar on top of the ridges were successfully created on the PMMA surface.

Chapter 5: Conclusion and future work

5.1 Conclusion

In conclusion, a new low-cost and repeatable method with high throughput to fabricate anisotropic wetting surfaces with good transparency has been presented in this thesis. All of the machined surfaces present significant anisotropy with them being hydrophobic in one direction and highly hydrophobic in the other direction. The highest contact angles obtained on these textured surfaces were 163.1° on 6061 Aluminum Alloy and 155.7° on PMMA surface. The anisotropic contact angle can reach up to 71.6° . This two-step method combined FIB machining of the tool and CNC machining using that structured tool to parallelize formation of these surface patterns and to improve the throughput significantly. Periodic microstructures including ridges and pillars were successfully fabricated by this method. It has been shown that this method can be used on both non-metallic (PMMA) and metallic surfaces (6061 Aluminum Alloy) with similar improvement of the anisotropic property.

A multistep FIB machining method was also developed to enable the accurate and reliable machining of non-conductive material such as SCD tool, in this thesis. The milling time of a microgroove was up to 10 minutes using this method which was similar to the conventional FIB machining. However, the structure built was much more accurate compared with the conventional process and avoided beam drifting and other artifacts to a great extent.

The MRR of this method is 1.5×10^8 times faster than conventional directly FIB milling on the workpiece with ion current of 1nA[79], even up to 8 times compared with single tip SCD tool and at least 11 times faster than laser cutting[85] which considered as extremely high throughput. Different CNC machining parameters including cutting speed, cutting depth and also materials have been confirmed non-related to the anisotropic wetting property of machined surface. Based on results, the anisotropic wettability is only determined by the design of microstructures and material characteristics.

Although this method overcame some of the limitations of other anisotropic wetting fabrication methods, it could still be improved further. For example, the form accuracy of FIB milling in terms of dimension, taper angle, ripple formation and sharpness of corners can be improved further. Improvement of the FIB machining will address to a great extent the form accuracy of the structures obtained on the CNC machining workpieces. In order

to obtain a more precise fabrication process, some corrections and improvement would be applied to this method which can be realized in the future.

5.2 Future work

5.2.1 FIB milling accuracy improvement

The first aspect that can be investigated is the FIB milling process. The accuracy of dimension can be improved by studying the enlarged dimension of structure compared with design. By aiming at dimension smaller than design, an actual dimension of milling structure could be obtained. In order to obtain finer edge of structures, a smaller current can be used which will lead to relative longer milling time.

The FIB milling efficiency in the process of micro-structure fabrication depends on the sputter yield. The incident angle is also related to ripple formation level. In this thesis, 6° incident angle was chosen in order to obtain the cutting through structures efficiently. So, it is critical to optimize the best angle of incident beam regarding to the sputtered yield and ripple dimension together. A suitable incident angle that can enable both less ripple formation level and high throughput of milling can be investigated in the future.

5.2.2 Hierarchical structures machining

The other aspect which can be studied is possibility of hierarchical structures machining. The microstructures have been proved can be fabricated with this method. Since the hierarchical structure showed great change of surface wettability, the machining possibility of this structure is very important. FIB can be used to milling both nano-level structure and micro-level structure on the surface. From FIB perspective, a hierarchical can be machined on the SCD tool, some feasible milling procedures from top view of tools are shown below in Figure 6.1. FIB machining of complex features such as those shown in Figure 6.1 on non conductive substrates require process development and optimization. Metal deposition between each step could be considered as a step which provides a great improvement to the milling results by avoiding beam drifting. Another challenge is to duplicate these structures to sample surface by CNC machining due to the deviation of CNC machine and tool alignment. Tool alignment deviation can be solved by changing tool holder or tool design to control it within nanometer level in order to fabrication nano-structures.

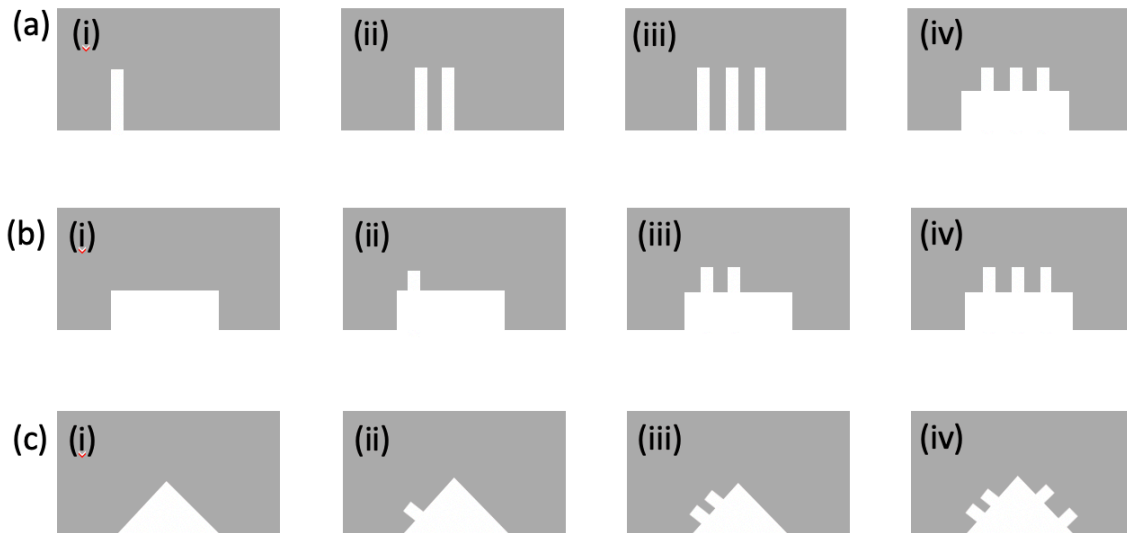


Figure 5. 1 Schematic of three feasible milling conceptions from top view. (a) First beginning with nano-structure fabrication and then applying micro-structures on the tool. (b) First beginning with micro-structures and then nano-structures (c) Triangle design with microstructure fabrication first and nanostructure after.

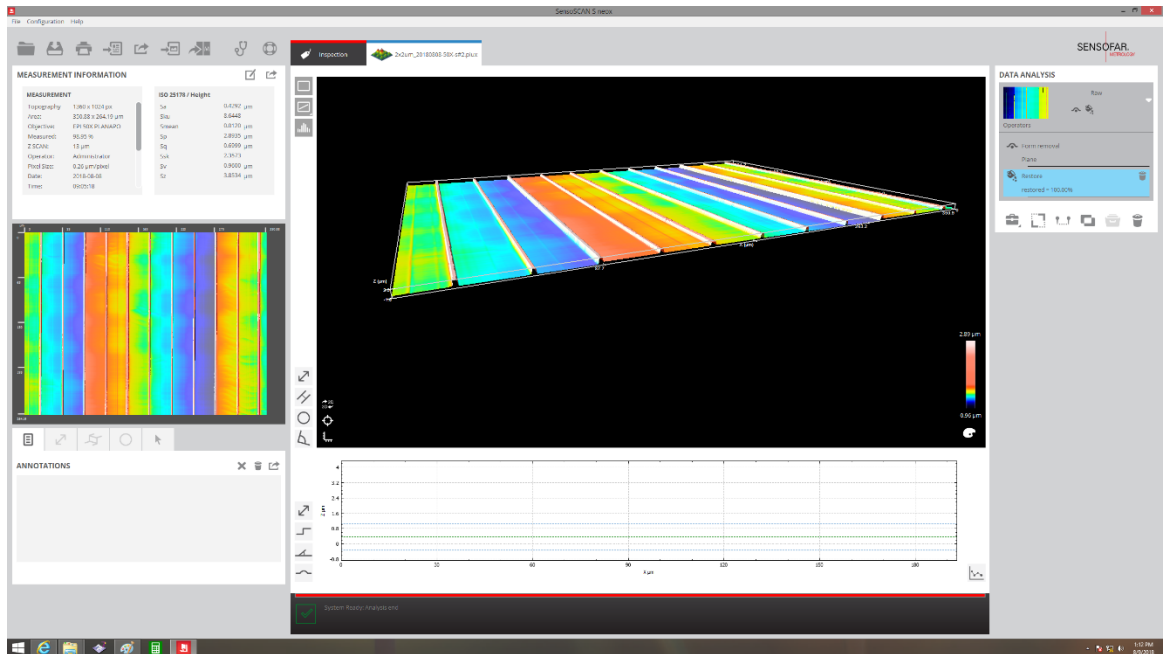
5.2.3 Applications

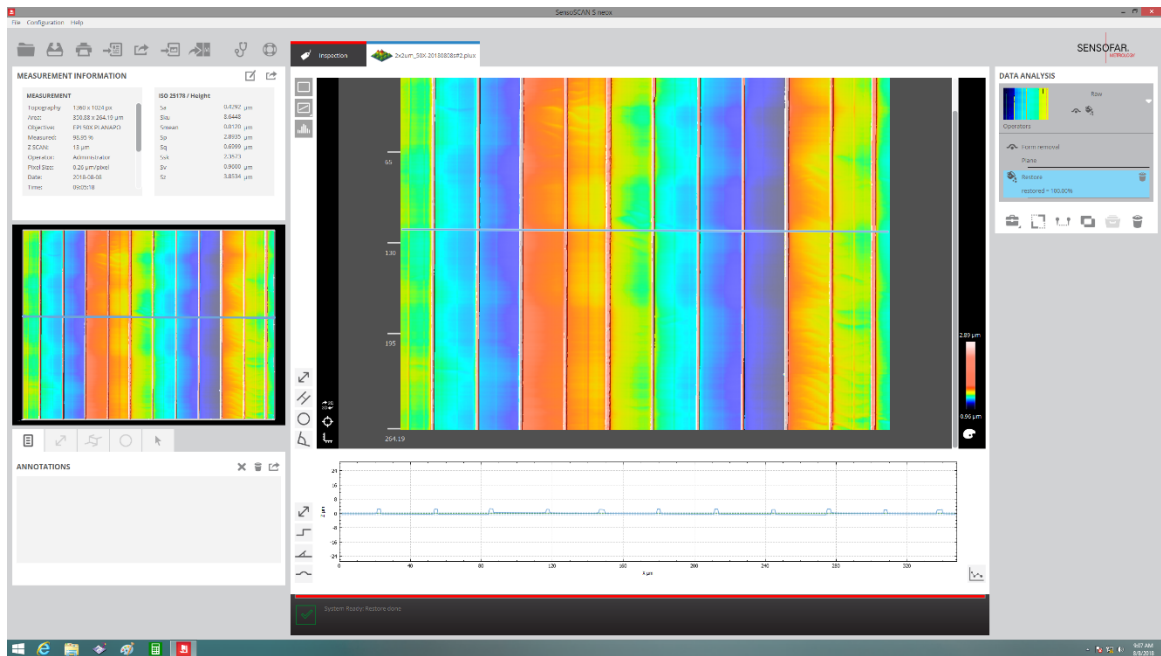
Finally, wide variety of applications can be developed for such textured surfaces and their properties studied. It is possible to fabricate a liquid path controlling surface by gradually changing spacing of microstructures or machining with different intersection angle. It will be a challenge to keep the uniformity of micro-pillars during these complex machining. By replicating machined surface with PDMS and applying into microfluidic devices, a fluid-control system can be realized which important to the microfluidic devices, as well as

biosensors and many other applications. Machined surface can also directly used in microfluidic devices, biosensors, as well as industry like airplane body surface. So different design of machining and its application is also a good aspect to be developed in the future.

In general, by overcoming existing problems in presented method, the wettability and accuracy of machined surfaces can be significantly improved. The achievement of hierarchical structures enables to fabricate an anisotropic superhydrophobic surface with a small sliding angle. By changing the pattern and machining path, a liquid-control system may be fabricated and has a big potential in many applications.

Appendix A: 3D scanning images under Sensofar confocal microscope in NRC (London)





Appendix B: Time-cost table of experimental process

Process	Time	Cost(CAD)
SCD tool	/	800
FIB milling	20-40min/each	50/hr
CNC machining	4min/(15mmx15mm area) at 1000mm/min speed	50/hr

LIST OF REFERENCES

- [1] C. R. Crick, “The chemistry and CVD of hydrophobic surfaces,” *UCL PhD Theses*, 2011.
- [2] R. Jafari and M. Farzaneh, “A Simple Method to Create Superhydrophobic Aluminium Surfaces,” *Mater. Sci. Forum*, vol. 706–709, pp. 2874–2879, 2012.
- [3] J. Jeevahan, M. Chandrasekaran, G. Britto Joseph, R. B. Durairaj, and G. Mageshwaran, “Superhydrophobic surfaces: a review on fundamentals, applications, and challenges,” *J. Coatings Technol. Res.*, vol. 15, no. 2, pp. 231–250, 2018.
- [4] B. Bhushan, Y. C. Jung, and K. Koch, “Micro-, nano- And hierarchical structures for superhydrophobicity, self-cleaning and low adhesion,” *Philos. Trans. R. Soc. A Math. Phys. Eng. Sci.*, vol. 367, no. 1894, pp. 1631–1672, 2009.
- [5] N. Michael and B. Bhushan, “Hierarchical roughness makes superhydrophobic states stable,” *Microelectron. Eng.*, vol. 84, no. 3, pp. 382–386, 2007.
- [6] M. Tang, M. H. Hong, and Y. S. Choo, “Hydrophobic surface fabrication by laser micropatterning,” *2008 IEEE Photonics Global Singapore, IPGC 2008*, pp. 1–4, 2008.
- [7] C. Guo, “Sink Electrical Discharge Machining of Superhydrophobic Surfaces Sink Electrical Discharge Machining of Superhydrophobic Surfaces By,” 2018.
- [8] O. Bliznyuk, E. Vereshchagina, E. S. Kooij, and B. Poelsema, “Scaling of anisotropic droplet shapes on chemically stripe-patterned surfaces,” *Phys. Rev. E - Stat. Nonlinear, Soft Matter Phys.*, vol. 79, no. 4, pp. 1–6, 2009.
- [9] D. Xia, L. M. Johnson, and G. P. López, “Anisotropic wetting surfaces with one-dimensional and directional structures: Fabrication approaches, wetting properties and potential applications,” *Adv. Mater.*, vol. 24, no. 10, pp. 1287–1302, 2012.
- [10] L. Liu, A. M. Jacobi, and D. Chvedov, “A surface embossing technique to create micro-grooves on an aluminum fin stock for drainage enhancement,” *J. Micromechanics Microengineering*, vol. 19, no. 3, 2009.

- [11] T. R. Society, “Thomas_Young-An_Essay_on_the_Cohesion_of_Fluids.”
- [12] K. Koch and W. Barthlott, “Superhydrophobic and superhydrophilic plant surfaces: an inspiration for biomimetic materials,” *Philos. Trans. R. Soc. A Math. Phys. Eng. Sci.*, vol. 367, no. 1893, pp. 1487–1509, Apr. 2009.
- [13] R. N. Wenzel, “Resistance of solid surfaces to wetting by water,” *Ind. Eng. Chem.*, vol. 28, no. 8, pp. 988–994, 1936.
- [14] A. B. D. Cassie and S. Baxter, “Of porous surfaces,” *Trans. Faraday Soc.*, no. 5, pp. 546–551, 1944.
- [15] R. E. Johnson and R. H. Dettre, “Contact angle hysteresis. III. Study of an idealized heterogeneous surface,” *J. Phys. Chem.*, vol. 68, no. 7, pp. 1744–1750, 1964.
- [16] W. Barthlott, “Epidermal and seed surface characters of plants: systematic applicability and some evolutionary aspects,” *Nord. J. Bot.*, vol. 1, no. 3, pp. 345–355, 1981.
- [17] Y. T. Cheng and D. E. Rodak, “Is the lotus leaf superhydrophobic?,” *Appl. Phys. Lett.*, vol. 86, no. 14, pp. 1–3, 2005.
- [18] K.-Y. Law and H. Zhao, “Drop Image Capturing and Drop Shape Analysis,” *Surface Wetting*. pp. 16-21, 2015.
- [19] G. L. Mack, “The Determination of Contact Angles from Measurements of the Dimensions of Small Bubbles and Drops. I. The Spheroidal Segment Method for Acute Angles,” *J. Phys. Chem.*, vol. 40, no. 2, pp. 159–167, 1935.
- [20] M. R. Sklodowska A, Wozniak M, “The method of contact angle measurements and estimation of work of adhesion in bioleaching of metals,” *Biol Proc*, vol. 1, no. 3, pp. 114–121, 1999.
- [21] Y. Rotenberg, L. Boruvka, and A. W. Neumann, “Determination of surface tension and contact angle from the shapes of axisymmetric fluid interfaces,” *J. Colloid Interface Sci.*, vol. 93, no. 1, pp. 169–183, 1983.
- [22] X. Zhang, F. Shi, J. Niu, Y. Jiang, and Z. Wang, “Superhydrophobic surfaces: From structural control to functional application,” *J. Mater. Chem.*, vol. 18, no. 6, pp. 621–633, 2008.

- [23] D. Instruments, “Determination of contact angles by different methods of dropshape analysis,” *Appl. note 12 DataPhysics*.
- [24] K.-Y. Law and H. Zhao, “Determination of Advancing and Receding Contact Angle,” *Surface Wetting*. pp. 25-28, 2016.
- [25] K.-Y. Law, “Definitions for Hydrophilicity, Hydrophobicity, and Superhydrophobicity: Getting the Basics Right,” *J. Phys. Chem. Lett.*, vol. 5, no. 4, pp. 686–688, 2014.
- [26] H. M. Ali, M. A. Qasim, S. Malik, and G. Murtaza, “Techniques for the Fabrication of Super-Hydrophobic Surfaces and Their Heat Transfer Applications,” in *Heat Transfer - Models, Methods and Applications*, vol. i, InTech, pp. 284-315, 2018.
- [27] B. Bhushan and Y. C. Jung, “Wetting, adhesion and friction of superhydrophobic and hydrophilic leaves and fabricated micro/nanopatterned surfaces,” *J. Phys. Condens. Matter*, vol. 20, no. 22, pp. 225010 1-24, 2008.
- [28] G. Shi, T. Franzke, W. Xia, M. D. Sanchez, and M. Muhler, “Highly dispersed MoO₃/Al₂O₃ shell-core composites synthesized by CVD of Mo(CO)₆ under atmospheric pressure,” *Chem. Vap. Depos.*, vol. 17, no. 4–6, pp. 162–169, 2011.
- [29] N. Licausi, S. Rao, and I. Bhat, “Low-pressure chemical vapor deposition of CdS and atomic layer deposition of CdTe films for HgCdTe surface passivation,” *J. Electron. Mater.*, vol. 40, no. 8, pp. 1668–1673, 2011.
- [30] S. O’Brien *et al.*, “Zinc oxide thin films: Characterization and potential applications,” *Thin Solid Films*, vol. 518, no. 16, pp. 4515–4519, 2010.
- [31] Z. Wang, M. Shoji, and H. Ogata, “Carbon nanosheets by microwave plasma enhanced chemical vapor deposition in CH₄-Ar system,” *Appl. Surf. Sci.*, vol. 257, no. 21, pp. 9082–9085, 2011.
- [32] S. Wang *et al.*, “Preparation of a durable superhydrophobic membrane by electrospinning poly (vinylidene fluoride) (PVDF) mixed with epoxy-siloxane modified SiO₂ nanoparticles: A possible route to superhydrophobic surfaces with low water sliding angle and high water contact,” *J. Colloid Interface Sci.*, vol. 359, no. 2, pp. 380–388, 2011.
- [33] S. R. Coulson, I. Woodward, J. P. S. Badyal, S. A. Brewer, and C. Willis, “Super-Repellent Composite Fluoropolymer Surfaces,” *J. Phys. Chem. B*, vol. 104, no. 37,

pp. 8836–8840, 2000.

- [34] D. J. Balazs, C. Hollenstein, and H. J. Mathieu, “Fluoropolymer coating of medical grade poly(vinyl chloride) by plasma-enhanced chemical vapor deposition techniques,” *Plasma Process. Polym.*, vol. 2, no. 2, pp. 104–111, 2005.
- [35] S. H. Yang, C. H. Liu, W. T. Hsu, and H. Chen, “Preparation of super-hydrophobic films using pulsed hexafluorobenzene plasma,” *Surf. Coatings Technol.*, vol. 203, no. 10–11, pp. 1379–1383, 2009.
- [36] L. Huang, S. P. Lau, H. Y. Yang, E. S. P. Leong, S. F. Yu, and S. Prawer, “Stable superhydrophobic surface via carbon nanotubes coated with a ZnO thin film,” *J. Phys. Chem. B*, vol. 109, no. 16, pp. 7746–7748, 2005.
- [37] Y. Qi, Z. Cui, B. Liang, R. S. Parnas, and H. Lu, “A fast method to fabricate superhydrophobic surfaces on zinc substrate with ion assisted chemical etching,” *Appl. Surf. Sci.*, vol. 305, pp. 716–724, 2014.
- [38] F. Chu and X. Wu, “Fabrication and condensation characteristics of metallic superhydrophobic surface with hierarchical micro-nano structures,” *Appl. Surf. Sci.*, vol. 371, pp. 322–328, 2016.
- [39] Z. Guo, F. Zhou, J. Hao, and W. Liu, “Stable biomimetic super-hydrophobic engineering materials,” *J. Am. Chem. Soc.*, vol. 127, no. 45, pp. 15670–15671, 2005.
- [40] X. Zhang *et al.*, “Polyelectrolyte Multilayer as Matrix for Electrochemical Deposition of Gold Clusters: Toward Super-Hydrophobic Surface,” *J. Am. Chem. Soc.*, vol. 126, no. 10, pp. 3064–3065, 2004.
- [41] S. V. Gnedenkov, S. L. Sinebryukhov, V. S. Egorin, and I. E. Vyaliy, “Wettability and electrochemical properties of the highly hydrophobic coatings on PEO-pretreated aluminum alloy,” *Surf. Coatings Technol.*, vol. 307, pp. 1241–1248, 2016.
- [42] L. Zhu, Y. Xiu, J. Xu, P. A. Tamirisa, D. W. Hess, and C. P. Wong, “Superhydrophobicity on two-tier rough surfaces fabricated by controlled growth of aligned carbon nanotube arrays coated with fluorocarbon,” *Langmuir*, vol. 21, no. 24, pp. 11208–11212, 2005.
- [43] L. Gao and T. J. McCarthy, “A perfectly hydrophobic surface ($\theta_A/\theta_R = 180^\circ/180^\circ$),” *J. Am. Chem. Soc.*, vol. 128, no. 28, pp. 9052–9053, 2006.

- [44] W. H. Huang and C. S. Lin, “Robust superhydrophobic transparent coatings fabricated by a low-temperature sol-gel process,” *Appl. Surf. Sci.*, vol. 305, pp. 702–709, 2014.
- [45] B. Xu and Z. Cai, “Fabrication of a superhydrophobic ZnO nanorod array film on cotton fabrics via a wet chemical route and hydrophobic modification,” *Appl. Surf. Sci.*, vol. 254, no. 18, pp. 5899–5904, 2008.
- [46] F. Rupp, L. Scheideier, N. Olshanska, M. De Wild, M. Wieland, and J. Geis-Gerstorfer, “Enhancing surface free energy and hydrophilicity through chemical modification of microstructured titanium implant surfaces,” *J. Biomed. Mater. Res. - Part A*, vol. 76, no. 2, pp. 323–334, 2006.
- [47] T.-S. Wong *et al.*, “Bioinspired self-repairing slippery surfaces with pressure-stable omniphobicity,” *Nature*, vol. 477, no. 7365, pp. 443–447, Sep. 2011.
- [48] G. Momen and M. Farzaneh, “A ZnO-based nanocomposite coating with ultra water repellent properties,” *Appl. Surf. Sci.*, vol. 258, no. 15, pp. 5723–5728, 2012.
- [49] A. Hozumi, K. Ushiyama, H. Sugimura, and O. Takai, “Fluoroalkylsilane Monolayers Formed by Chemical Vapor Surface Modification on Hydroxylated Oxide Surfaces,” *Langmuir*, vol. 15, no. 22, pp. 7600–7604, Oct. 1999.
- [50] K. Teshima, H. Sugimura, Y. Inoue, O. Takai, and A. Takano, “Transparent ultra water-repellent poly(ethylene terephthalate) substrates fabricated by oxygen plasma treatment and subsequent hydrophobic coating,” *Appl. Surf. Sci.*, vol. 244, no. 1–4, pp. 619–622, 2005.
- [51] B. Balu, V. Breedveld, and D. W. Hess, “Fabrication of ‘roll-off’ and ‘sticky’ superhydrophobic cellulose surfaces-via plasma processing,” *Langmuir*, vol. 24, no. 9, pp. 4785–4790, 2008.
- [52] C. Chen *et al.*, “A green one-step fabrication of superhydrophobic metallic surfaces of aluminum and zinc,” *J. Alloys Compd.*, vol. 711, pp. 506–513, 2017.
- [53] S. D. Bhagat and M. C. Gupta, “Superhydrophobic microtextured polycarbonate surfaces,” *Surf. Coatings Technol.*, vol. 270, pp. 117–122, 2015.
- [54] L. Feng, M. Yang, X. Shi, Y. Liu, Y. Wang, and X. Qiang, “Copper-based superhydrophobic materials with long-term durability, stability, regenerability, and self-cleaning property,” *Colloids Surfaces A Physicochem. Eng. Asp.*, vol. 508, pp.

39–47, 2016.

- [55] Y. Liu, X. Yin, J. Zhang, Y. Wang, Z. Han, and L. Ren, “Biomimetic hydrophobic surface fabricated by chemical etching method from hierarchically structured magnesium alloy substrate,” *Appl. Surf. Sci.*, vol. 280, pp. 845–849, 2013.
- [56] Y. Wang, W. Wang, L. Zhong, J. Wang, Q. Jiang, and X. Guo, “Super-hydrophobic surface on pure magnesium substrate by wet chemical method,” *Appl. Surf. Sci.*, vol. 256, no. 12, pp. 3837–3840, 2010.
- [57] B. Yin *et al.*, “Novel strategy in increasing stability and corrosion resistance for super-hydrophobic coating on aluminum alloy surfaces,” *Appl. Surf. Sci.*, vol. 258, no. 1, pp. 580–585, 2011.
- [58] K. Tsougeni, N. Vourdas, A. Tserepi, E. Gogolides, and C. Cardinaud, “Mechanisms of oxygen plasma nanotexturing of organic polymer surfaces: From stable super hydrophilic to super hydrophobic surfaces,” *Langmuir*, vol. 25, no. 19, pp. 11748–11759, 2009.
- [59] G. R. B. E. Römer, A. J. Huis in’t Veld, J. Meijer, and M. N. W. Groenendijk, “On the formation of laser induced self-organizing nanostructures,” *CIRP Ann. - Manuf. Technol.*, vol. 58, no. 1, pp. 201–204, 2009.
- [60] J. Noh, J. H. Lee, S. Na, H. Lim, and D. H. Jung, “Fabrication of hierarchically micro-and nano-structured mold surfaces using laser ablation for mass production of superhydrophobic surfaces,” *Jpn. J. Appl. Phys.*, vol. 49, no. 10, pp. 1065021–1065026, 2010.
- [61] D. M. Chun, C. V. Ngo, and K. M. Lee, “Fast fabrication of superhydrophobic metallic surface using nanosecond laser texturing and low-temperature annealing,” *CIRP Ann. - Manuf. Technol.*, vol. 65, no. 1, pp. 519–522, 2016.
- [62] D. M. Chun, G. Davaasuren, C. V. Ngo, C. S. Kim, G. Y. Lee, and S. H. Ahn, “Fabrication of transparent superhydrophobic surface on thermoplastic polymer using laser beam machining and compression molding for mass production,” *CIRP Ann. - Manuf. Technol.*, vol. 63, no. 1, pp. 525–528, 2014.
- [63] G. Davaasuren, C. V. Ngo, H. S. Oh, and D. M. Chun, “Geometric study of transparent superhydrophobic surfaces of molded and grid patterned polydimethylsiloxane (PDMS),” *Appl. Surf. Sci.*, vol. 314, pp. 530–536, 2014.

- [64] J. Long, M. Zhong, H. Zhang, and P. Fan, “Superhydrophilicity to superhydrophobicity transition of picosecond laser microstructured aluminum in ambient air,” *J. Colloid Interface Sci.*, vol. 441, pp. 1–9, 2015.
- [65] C. V. Ngo and D. M. Chun, “Fabrication of un-coated transparent superhydrophobic sapphire surface using laser surface ablation and heat treatment,” *CIRP Ann.*, vol. 67, no. 1, pp. 571–574, 2018.
- [66] R. Shanmuga Prakash, M. Sivakumar, M. Jeevaraja, and G. Saravanan, “Review on wire electrical discharge machining of die and tool grade steels,” *Int. J. Appl. Eng. Res.*, vol. 10, no. 85, pp. 521–527, 2015.
- [67] P. B. Weisensee, E. J. Torrealba, M. Raleigh, A. M. Jacobi, and W. P. King, “Hydrophobic and oleophobic re-entrant steel microstructures fabricated using micro electrical discharge machining,” *J. Micromechanics Microengineering*, vol. 24, no. 9, pp. 960-1317, 2014.
- [68] M. Morita, T. Koga, H. Otsuka, and A. Takahara, “Macroscopic-wetting anisotropy on the line-patterned surface of fluoroalkylsilane monolayers,” *Langmuir*, vol. 21, no. 3, pp. 911–918, 2005.
- [69] S. Wang *et al.*, “Controlling Flow Behavior of Water in Microfluidics with a Chemically Patterned Anisotropic Wetting Surface,” *Langmuir*, vol. 31, no. 13, pp. 4032–4039, Apr. 2015.
- [70] F. Zhang and H. Y. Low, “Anisotropic wettability on imprinted hierarchical structures,” *Langmuir*, vol. 23, no. 14, pp. 7793–7798, 2007.
- [71] D. Rhee, W. K. Lee, and T. W. Odom, “Crack-Free, Soft Wrinkles Enable Switchable Anisotropic Wetting,” *Angew. Chemie - Int. Ed.*, vol. 56, no. 23, pp. 6523–6527, 2017.
- [72] G. Lin, Q. Zhang, C. Lv, Y. Tang, and J. Yin, “Small degree of anisotropic wetting on self-similar hierarchical wrinkled surfaces,” *Soft Matter*, vol. 14, no. 9, pp. 1517–1529, 2018.
- [73] X. Ding *et al.*, “Fabrication of a micro-size diamond tool using a focused ion beam,” *J. Micromechanics Microengineering*, vol. 18, no. 7, pp 075017 1-10, 2008.
- [74] C. a Volkert, a M. Minor, G. Editors, and B. May, “F ocused Ion Beam Micromachining,” *MRS Bull.*, vol. 32, no. May, pp. 389–399, 2007.

- [75] J. Sun *et al.*, “Fabrication of a side aligned optical fibre interferometer by focused ion beam machining,” *J. Micromechanics Microengineering*, vol. 23, no. 10, pp. 105005 1-9, 2013.
- [76] L. A. Giannuzzi and F. A. Stevie, “A review of focused ion beam milling techniques for TEM specimen preparation 10_1016-S0968-4328(99)00005-0 Micron ScienceDirect_com,” *Micron*, vol. 30, pp. 197–204, 1999.
- [77] Z. Tong *et al.*, “Review on FIB-Induced Damage in Diamond Materials,” *Curr. Nanosci.*, vol. 12, no. 6, pp. 685–695, 2016.
- [78] M. Dufek, “FEI Versa 3D User Operation Manual.” FEI company, p. Edition 7, 2013.
- [79] J. Sun, X. Luo, W. Chang, J. M. Ritchie, J. Chien, and A. Lee, “Fabrication of periodic nanostructures by single-point diamond turning with focused ion beam built tool tips,” *J. Micromechanics Microengineering*, vol. 22, no. 11, 2012.
- [80] Y. Yan, Z. Hu, X. Zhao, T. Sun, S. Dong, and X. Li, “Top-down nanomechanical machining of three-dimensional nanostructures by atomic force microscopy,” *Small*, vol. 6, no. 6, pp. 724–728, 2010.
- [81] Sensofar Company “Simply Powerful.Instruction of Sensofar Metrology,” pp. 40–41.
- [82] M. J. Vasile, C. R. Friedrich, B. Kikkeri, and R. McElhannon, “Micrometer-scale machining: tool fabrication and initial results,” *Precis. Eng.*, vol. 19, no. 2–3, pp. 180–186, 1996.
- [83] R. M. Bradley and J. M. E. Harper, “Theory of ripple topography induced by ion bombardment,” *J. Vac. Sci. Technol. A Vacuum, Surfaces, Film.*, vol. 6, no. 4, pp. 2390–2395, Jul. 1988.
- [84] Z. Tong, X. Luo, J. Sun, Y. Liang, and X. Jiang, “Investigation of a scale-up manufacturing approach for nanostructures by using a nanoscale multi-tip diamond tool,” *Int. J. Adv. Manuf. Technol.*, vol. 80, no. 1–4, pp. 699–710, 2015.
- [85] D. H. Kam, L. Shah, and J. Mazumder, “Femtosecond laser machining of multi-depth microchannel networks onto silicon,” *J. Micromechanics Microengineering*, vol. 21, no. 4, 2011.
- [86] Y. H. Mori, T. G. M. van de Ven, and S. G. Mason, “Resistance to spreading of

liquids by sharp edged microsteps,” *Colloids and Surfaces*, vol. 4, no. 1, pp. 1–15, 1982.

- [87] A. A. Darhuber and S. M. Troian, “Principles of Microfluidic Actuation By Modulation of Surface Stresses,” *Annu. Rev. Fluid Mech.*, vol. 37, no. 1, pp. 425–455, 2005.
- [88] T. Cubaud and M. Fermigier, “Faceted drops on heterogeneous surfaces,” *Europhys. Lett.*, vol. 55, no. 2, pp. 239–245, 2001.
- [89] O. Bliznyuk, V. Veligura, E. S. Kooij, H. J. W. Zandvliet, and B. Poelsema, “Metastable droplets on shallow-grooved hydrophobic surfaces,” *Phys. Rev. E - Stat. Nonlinear, Soft Matter Phys.*, vol. 83, no. 4, pp. 1–9, 2011.